



**Francisco Leite de
Castro**

**ERODIBILITY OF A DIKE IN CASE OF
OVERFLOWING**

**EROSÃO ASSOCIADA AO GALGAMENTO DE UM
DIQUE**



**Francisco Leite de
Castro**

**ERODIBILITY OF A DIKE IN CASE OF
OVERFLOWING**

**EROSÃO ASSOCIADA AO GALGAMENTO DE UM
DIQUE**

Dissertação apresentada à Universidade de Aveiro para cumprimento dos requisitos necessários à obtenção do grau de Mestre em Engenharia Civil, realizada sob a orientação científica da Doutora Inês Osório de Castro Meireles, Professora Auxiliar do Departamento de Engenharia Civil da Universidade de Aveiro e coorientação científica do Doutor Carlos Daniel Borges Coelho, Professor Auxiliar do Departamento de Engenharia Civil da Universidade de Aveiro e do Doutor Goran Gjetvaj, Professor Catedrático do *Water Research Department* da Faculdade de Engenharia Civil da Universidade de Zagreb.

Dedico esta dissertação de mestrado à minha família, namorada e amigos.

o júri

presidente

Prof. Doutor Miguel Nuno Lobato de Sousa Monteiro de Morais
Professor Auxiliar da Universidade de Aveiro

Prof. Doutora Teresa Viseu Sarrico Santos
Investigadora Auxiliar do Laboratório Nacional de Engenharia Civil

Prof. Doutora Inês Osório de Castro Meireles
Professora Auxiliar da Universidade de Aveiro

agradecimentos

Quero agradecer a todos as pessoas que direta ou indiretamente contribuíram para que o desenvolvimento desta dissertação de mestrado fosse possível. Em primeiro lugar quero agradecer à minha orientadora, Inês Meireles, por todo o apoio prestado ao nível da revisão científica desta dissertação, bem como pelos inúmeros conselhos e palavras de incentivo.

Queria agradecer ao meu coorientador, Carlos Coelho, por me ter permitido realizar parte desta dissertação ao abrigo do programa Erasmus e pelas sugestões apresentadas durante o seu desenvolvimento.

Queria deixar também uma palavra de apreço ao meu coorientador Goran Gjetvaj pela sua disponibilidade, ajuda e acompanhamento constante durante o desenvolvimento da parte experimental desta dissertação.

Tenho também que agradecer ao *Water Research Department* da Faculdade de Engenharia Civil da Universidade de Zagreb (Croácia) pelo fornecimento dos materiais testados e pela utilização do seu modelo hidráulico e respetiva instrumentação associada.

Não posso de deixar de mencionar também todos os amigos que me acompanham já há vários anos nesta jornada e todos aqueles com quem fui criando fortes laços de amizade.

Quero também deixar uma palavra de afeto à minha namorada, Carolina Gaspar, pela paciência, carinho e apoio incondicional, e por nunca ter deixado de acreditar em mim mesmo quando eu já começava a duvidar das minhas capacidades.

Por fim quero agradecer à minha família, em especial ao meu irmão, João Castro, à minha mãe, Ana Leite e ao meu Pai, Manuel Castro por todo o carinho dispensado e por toda a confiança que depositaram em mim.

palavras-chave

diques de terra, galgamento, produtos em rolo para controlo de erosão, erosão hídrica superficial, estudo experimental, reforço de camadas de relva.

resumo

Os diques de terra são construídos um pouco por todo o mundo, quer em zonas costeiras (diques costeiros) quer em zonas fluviais (diques fluviais), com o intuito de proteger a população, as infraestruturas e outros recursos de elevados níveis de água provocados por tempestades e cheias sazonais. A grande maioria destes aterros de proteção de cheias não estão preparados para resistir à erosão superficial provocada na sua crista e talude de jusante pelo galgamento da água e respetivo escoamento sobre os mesmos, e como tal, podem estar em risco de rotura. A mitigação dos danos induzidos num dique pelo galgamento pode ser conseguida por via da proteção da camada superficial de solo sobre a crista e talude de jusante. Existe uma enorme variedade de materiais para proteção contra a erosão (enrocamento, betão, geossintéticos, etc.) que podem variar desde soluções mais pesadas e rígidas a soluções mais leves e flexíveis.

A presente dissertação foca-se em sistemas de reforço leves, flexíveis e compostos por redes/tapetes poliméricos tais como as mantas/tapetes de reforço (*Turf Reinforcement Mats*) e geogrelhas (*geogrids*). O objetivo principal da dissertação consistiu em avaliar a aplicabilidade destes materiais como sistemas de controlo de erosão, e obter dados relativos ao seu desempenho perante uma situação de galgamento/escoamento criada num modelo hidráulico à escala real. Os valores do caudal escoado, as alturas de água e velocidades médias do escoamento foram medidos numa determinada secção do canal (com inclinação 1V:4H) do modelo hidráulico (secção próxima da zona de transição entre o canal inclinado e o canal horizontal). Estas medições permitiram estimar gamas de valores da tensão de corte aplicada na superfície do canal e do coeficiente de rugosidade de *Manning*. Algumas equações empíricas (de carácter provisório) foram apresentadas, relacionando a tensão de corte e alturas de água com o caudal escoado. Os resultados obtidos são exclusivamente válidos para o material granular e os produtos em rolo para controlo de erosão (*Rolled Erosion Control Products*) testados, bem como para a gama de parâmetros hidráulicos proporcionados pelo modelo hidráulico. O estudo experimental permitiu obter principalmente conclusões qualitativas, nas quais ficou comprovado que o reforço de uma camada superficial de solo com *Rolled Erosion Control Products* permite resistir a caudais superiores, em comparação com uma camada de solo simples, sem que se verifique transporte pronunciado de partículas de solo.

keywords

earthen dikes, overflowing, rolled erosion control products, surface soil erosion, laboratory study, turf reinforcement.

abstract

Earthen dikes (or earthen levees) are built all over the world, both in coastal (coastal dikes) and inland areas (riverine dikes), to protect population, infrastructures and resources from high water levels due to storm surges and seasonal floods. Most of these flood defence embankments are not prepared to resist to surface soil erosion of its crest and landside slope induced by overflowing events, and hence, maybe at risk of failure. Mitigation of dike damage by overflow may be accomplished by providing erosion protection on the surface of the crest and dike landside slope. Erosion protection can be conferred by a variety of materials (rip-rap, concrete, geosynthetics, etc.) ranging from hard armouring to light armouring alternatives.

The present dissertation focuses on strengthening systems consisting of lightweight, flexible, synthetic mats such as (high performance) turf reinforcement mats and geogrids. The goal of this dissertation was to assess their effectiveness as a slope erosion protection system and to obtain some performance criteria under overflow conditions created through full-scale laboratory testing on a hydraulic model. Waterflow discharge, flow thickness and mean (horizontal) velocity measurements were acquired at one location on the landside slope channel (1V:4H) (near the downward edge of the slope). These measurements allowed to estimate shear stress ranges at the bed channel and Manning's roughness coefficients. Some tentative empirical equations were presented correlating shear stress and flow thickness estimations with overflowing discharges. The results are strictly limited to the tested coarse-grained soil and rolled erosion control products as well as the range of tested hydraulic parameters possible to be attained on the hydraulic model. The experimental study mainly allowed to obtain some qualitative conclusions, in which it was proven that a reinforced surface soil layer with synthetic mats of a dike slope can withstand higher overflowing discharges than bare soil, without catastrophic sediment motion.

TABLE OF CONTENTS

| | |
|---|-----|
| Table of contents | I |
| List of figures | III |
| List of tables | IX |
| List of variables and symbols | XI |
| Acronyms | XV |
| 1. Introduction | 1 |
| 1.1. General context and motivation..... | 1 |
| 1.2. Objectives | 2 |
| 1.3. Dissertation structure..... | 3 |
| 2. Earthen dikes | 5 |
| 2.1. Factors that affect the erosion process..... | 5 |
| 2.1.1. Types of dikes and constituent material | 5 |
| 2.1.2. Hydraulic loading | 8 |
| 2.2. Earthen dike failure | 9 |
| 2.3. Dike overtopping | 12 |
| 2.3.1. Overtopping types | 12 |
| 2.3.2. Hydraulic processes of surge-only overflow | 15 |
| 2.3.3. Vertical velocity profile..... | 19 |
| 2.3.4. Estimation of the shear stress | 20 |
| 2.3.5. Estimation of manning's n values | 24 |
| 2.4. External erosion..... | 24 |
| 2.4.1. Erodibility of cohesive sediments..... | 28 |
| 2.4.2. Erodibility of non-cohesive sediments | 32 |
| 2.5. Breaching process..... | 32 |
| 2.5.1. Non-cohesive breaching | 34 |
| 2.5.2. Cohesive breaching..... | 35 |
| 2.5.3. Breach overflow in stage I..... | 38 |
| 2.6. Surface protection covers | 41 |
| 2.6.1. Earthen spillways..... | 41 |

| | | |
|----------|---|-----|
| 2.6.2. | Strengthening systems for earthen embankments | 43 |
| 2.6.2.1. | Grass protection cover..... | 44 |
| 2.6.2.2. | Reinforced grass protection cover..... | 45 |
| 2.7. | Performance of surface protection covers under surge-overflow | 49 |
| 2.8. | Full-scale overtopping tests..... | 58 |
| 2.8.1. | Nelsen (2005) laboratory experiments | 59 |
| 2.8.2. | Haselsteineir <i>et al.</i> (2008) laboratory experiments | 63 |
| 2.8.3. | Amini and Li (2012) laboratory experiments..... | 66 |
| 3. | Experimental study..... | 74 |
| 3.1. | Physical model | 74 |
| 3.1.1. | Hydraulic model..... | 74 |
| 3.1.2. | Reinforced granular revetment..... | 78 |
| 3.1.2.1. | Foundation layer..... | 79 |
| 3.1.2.2. | Gravel layer | 80 |
| 3.1.2.3. | Rolled Erosion Control Products..... | 83 |
| 3.2. | Instrumentation..... | 90 |
| 3.2.1. | Electromagnetic flowmeter | 90 |
| 3.2.2. | Velocimeter | 90 |
| 3.3. | Experimental program..... | 92 |
| 3.3.1. | Preliminary study | 98 |
| 3.3.2. | Test performance and observations..... | 101 |
| 3.3.3. | Data collected and observations..... | 111 |
| 3.4. | Data analysis and results | 118 |
| 4. | Summary and conclusions..... | 126 |
| | References | 130 |

LIST OF FIGURES

| | | |
|------------|--|----|
| Figure 1. | Homogeneous flood defence dike typical of UK (Morris <i>et al.</i> , 2009)..... | 7 |
| Figure 2. | Typical cross-section of a zoned earthen dike containing an impervious core (CIRIA <i>et al.</i> , 2013)..... | 8 |
| Figure 3. | Typical cross-section of a coastal embankment with a surface impervious mask (Morris <i>et al.</i> , 2009)..... | 8 |
| Figure 4. | Failure mechanisms of an earthen embankment (Schmocker, 2011)..... | 10 |
| Figure 5. | Diagram of dike failure mechanisms by overtopping (van Gerven and Akkerman, 2005)..... | 11 |
| Figure 6. | Overtopping types for earthen dikes (Pan <i>et al.</i> , 2012): (a) Surge-only overflow ($R_c < 0$); (b) Wave-only overtopping ($R_c > 0$); (c) Wave-only overtopping ($R_c = 0$); (d) Combined wave and surge overtopping ($R_c < 0$)..... | 13 |
| Figure 7. | Wave-only overtopping event (with major wave activity) and its associated flood hydrograph (Hewlett <i>et al.</i> , 1987 in CIRIA <i>et al.</i> , 2013)..... | 14 |
| Figure 8. | Combined wave overtopping and storm surge overflow (with minor wave activity) event and its associated flood hydrograph (Hewlett <i>et al.</i> , 1987 in CIRIA <i>et al.</i> , 2013)..... | 15 |
| Figure 9. | Characterization of steady overflow (flow regime, speed and water depth) over a spillway or dike (CIRIA <i>et al.</i> , 2013)..... | 16 |
| Figure 10. | Vertical velocity profile (CIRIA <i>et al.</i> , 2013)..... | 20 |
| Figure 11. | Definition of bed shear stress for uniform flow (Schmocker, 2011)..... | 21 |
| Figure 12. | Surge overflow mean shear stress as a function of discharge (prototype scale) (Hughes <i>et al.</i> , 2012)..... | 23 |
| Figure 13. | Scheme of forces acting on a submerged particle of a stream bed channel (CIRIA <i>et al.</i> , 2013)..... | 25 |
| Figure 14. | Relationship between soil erodibility [K_d ($\text{cm}^3/\text{N}\cdot\text{s}$)] and compaction water content [WC (%)] for two soil types (SM or CL) (on the right side); and relationship between soil dry density [ρ_d (g/cm^3)] and compaction water content [WC (%)] for two soil types (SM or CL) (on the left side) (Hanson <i>et al.</i> , 2010)..... | 27 |

Figure 15. Erosion resistance chart in case of dike overtopping (Briaud *et al.*, 2008)..... 28

Figure 16. Relationship between flow velocity and shear stress within the flow depth (Briaud *et al.*, 2008). 29

Figure 17. Soil erodibility according to the values of K_d and τ_c of cohesive streambeds (Hanson and Simon, 2001). 31

Figure 18. Schematic representation of the breach development (in 5 steps) in a sand dike (Visser, 1998). 35

Figure 19. Sketch of the breaching process in phase I (Zhu, 2006). 36

Figure 20. Phases II ($t=t_2$), III ($t=t_3$), IV ($t=t_4$) and V ($t=t_5$) of the breaching process in an embankment with a cohesive soil (Zhu, 2006)..... 37

Figure 21. Waterflow on the initial breach channel created on the dike crest and downstream slope of the dike in stage I (Zhu, 2006). 38

Figure 22. Trapezoidal cross-section of the breach in the dike crest (Zhu, 2006)..... 39

Figure 23. Example of a bypass spillway diverting flood flow towards a flood expansion zone (Degoutte *et al.*, 2012 in CIRIA *et al.*, 2013). 42

Figure 24. Erosion control reinforcement techniques (Miller *et al.*, 2012). 43

Figure 25. Functions of the geosynthetics in earthen embankments (FEMA, 2008). 45

Figure 26. Vegetated high performance TRM system. Soil reinforcement is provided by the interlocking between the roots and mat (Hulitt, 2010). 46

Figure 27. Installation of HPTRMs on a New Orleans dike (Flikweert *et al.*, 2013)..... 49

Figure 28. Limiting velocity versus duration curves created by Hewlett *et al.* (1987), for stability of slope protection surfaces subject to steady overflow (in Landa, 2014). 50

Figure 29. Comparison between Hewlett *et al.* (1987) grass performance curves and the original field test data from Whitehead *et al.* (1976) (in Hughes, 2011). 51

Figure 30. Best fit of equation (40) with Hewlett *et al.* (1987) grass curves made by Dean *et al.* (2010) (in Hughes, 2011). 55

Figure 31. Schematic representation of the cumulative work excess work concept presented by Dean *et al.* (2010) (in Hughes, 2011)..... 55

Figure 32. Best fit of equation (40) with Hewlett *et al.* (1987) performance curves related to open and filled mats (Hughes, 2011). 57

| | |
|---|----|
| Figure 33. Flow velocity measurement (on the left picture) and flow depth measurement (on the right picture) in the testing channel (Nelsen, 2005). | 60 |
| Figure 34. Example of flood hydrograph for a small basin showing Q_{peak} and duration of flow exceeding 90% of Q_{peak} (Miller <i>et al.</i> , 2012). | 63 |
| Figure 35. Overflow protection system using geogrid/nonwoven geotextile (a type of RECP) and ground pins/nails (Haselsteiner <i>et al.</i> , 2008). | 64 |
| Figure 36. Overflowing experiments with a slope protection system with geosynthetics (Combigrid®). On the left: before overflow; on the right: in overflow state with $q_{max}=300$ l/s/m (Haselsteinaer <i>et al.</i> , 2008). | 65 |
| Figure 37. Sketch of the flume where the physical model is installed (top and side view) (Pan <i>et al.</i> , 2012). | 67 |
| Figure 38. Metal tray with vegetated HPTRM system being installed on the dike inside the flume (Amini and Li, 2012). | 67 |
| Figure 39. Location of ADVs and acoustic range finder at the crest and lanside slope of the physical model (Pan <i>et al.</i> , 2012). | 68 |
| Figure 40. Measured flow thickness, measured flow velocity and calculated discharge time series representative of combined surge overflow and wave overtopping at a dike crest location (Hulitt, 2010). | 69 |
| Figure 41. Steady overflow discharge (q_s) versus upstream head (h_l) (or negative freeboard ($-R_c$)) for 3 different strengthening systems (rolled compacted concrete protection system (RCC); articulated concrete block protection system (ACB); and high performance turf reinforcement system (HPTRM) (Amini and Li, 2012). | 70 |
| Figure 42. Steady flow thickness (d_s) on landside slope (represented by a hydraulic parameter) versus specific discharge (q_s) for three different strengthening systems (RCC, ACB and HPTRM) (Amini and Li, 2012). | 71 |
| Figure 43. Surge-only overflow on the landside slope of the physical model with a vegetated HPTRM system installed on it (left side photograph). Reinforced grass system after the surge-only overflow experiment (right side photograph) (Hulitt, 2010). | 72 |
| Figure 44. Soil loss measurements (cm) in the landside slope for a specific discharge $q_s=0.251$ m ³ /s/m and overflow duration of 60 minutes (Hulitt, 2010). | 73 |

Figure 45. Schematic illustration of the overtopping hydraulic model. 74

Figure 46. Dimensions of hydraulic model layout (in mm). 75

Figure 47. Sediment trap (hydraulic model’s horizontal platform) releasing water to the container (on the left picture). Detail of v-notch weir installed in back part of the container (on the right picture). 76

Figure 48. Steady overflow over an earthen embankment (Hughes *et al.*, 2011). 77

Figure 49. Detail of crest of the hydraulic model at the intake section (dimension defined in mm). 78

Figure 50. Auxiliary components of the hydraulic model. 78

Figure 51. Foundation layer lying down at the hydraulic model channel bottom. 79

Figure 52. Coarse-grained soil samples for overtopping tests. 80

Figure 53. Most widely accepted sediment classification systems (Zhu, 2006). 81

Figure 54. Particle size distribution of the gravel material used for hydraulic model’s bottom and top layer. 82

Figure 55. Detail of RECPs (M₁, M₂, M₃, M₄, M₅ and M₆) used in the experiments. 84

Figure 56. Installation of RECP (M₁) over the gravel layer of the hydraulic model slope (on the left picture). Detail of the system used to function as anchors: nails with a plastic head (on the right picture). 84

Figure 57. RECP M₅ (Vmax C350[®]) (on the left picture) and RECP M₆ (Vmax C350[®]) (on right the picture) with anchorage density of 8.2 anchors/m² over the channel slope. 85

Figure 58. Recommended anchorage pattern for RECPs M₄ and M₅ by the manufacturer, consisting of anchor density of 4.5 anchors/m² (Tensar[®], 2010). 86

Figure 59. Application of a composite product of a geogrid and geotextile (Combigrid[®]) for soil reinforcement (on the left picture) and application of a geogrid layer only with U-shaped fasteners over a steep slope (on the right picture) (figure extracted from www.naue.com, 2013). 89

Figure 60. Electromagnetic flowmeter utilized to measure the flow discharge. 90

Figure 61. Velocimeter used for a rough estimation of flow velocities in the vicinity of slope’s toe of the hydraulic model. 91

Figure 62. CSLI (beneath the mat) versus shear stress on RECP (Sprague, 2011). 95

Figure 63. Shields diagram: estimation of shields parameter Ψ_{cr} for each gravel bed according to D^* (Quintela, 1981). 100

Figure 64. Formation of breach channel through the slope's granular revetment. 102

Figure 65. Breach formation process with RECP M₁ embedded in granular s.A. 103

Figure 66. Reinforced gravel layer being submitted to a Q_{max} (on the left picture). RECP M₁ profile exhibiting a wavy shape after the passage of a 25.0 l/s flow discharge over it (on the right picture). 104

Figure 67. Development of a breach channel above the RECP M₂. 105

Figure 68. Erosion of top granular gravel layer s.C. 105

Figure 69. Gravel bed s.C being lift by underlying currents. 106

Figure 70. Development of a breach channel above the RECP M₃. 107

Figure 71. Removal of the sediments above the RECP M₃ by waterflow (on the left picture). Channel lining after the passage of Q_{max} (on the right picture). 107

Figure 72. Development of a breach channel above the RECP M₄. 108

Figure 73. Bed channel being submitted to Q_{max} (on the left picture). Bed channel configuration after overtopping event has been ended (on the right picture). 108

Figure 74. Initiation of the erosion process at the gravel top layer (beneath the TRM M₅) (on the left picture). Bed channel configuration after the overtopping event has ended, *i.e.*, after Q_{max} (on the right picture). 109

Figure 75. Initiation of the erosion process at the gravel top layer (beneath the TRM M₆) (on the left picture). Bed channel configuration after the overtopping event has ended, *i.e.*, after Q_{max} (on the right picture). 110

Figure 76. Measurement of velocity with an unsubmerged velocimeter. 115

Figure 77. Flowing water exhibiting turbulence ($Q_{max}=29.6$ l/s). 116

Figure 78. Waterflow depth profile (on the left picture) and water jet created due to irregularity of the surface granular layer (on the right picture). 117

Figure 79. Estimated values of Manning's n at cross-section A. 120

Figure 80. Manning's n versus flow thickness (Hughes *et al.*, 2011). 120

Figure 81. Unit discharge parameter versus shear stress on the lining (s.A+M₁). 121

Figure 82. Overflow parameter that includes measured average flow thickness versus unit discharge (calculated through the measured velocity and flow thickness). 123

LIST OF TABLES

| | | |
|-----------|--|----|
| Table 1. | Functions of dike components (CIRIA <i>et al.</i> , 2013). | 6 |
| Table 2. | Types of hydraulic actions and their relevance in several environments (CIRIA <i>et al.</i> , 2013)..... | 9 |
| Table 3. | Classification of clay in terms of erosion resistance (TAW, 2006 in Oumeraci <i>et al.</i> , 2005). | 28 |
| Table 4. | Approximate values of K_d determined by compaction and percentage of clay (adapted from CIRIA <i>et al.</i> , 2013)..... | 30 |
| Table 5. | Approximate values of τ_c (Pa) depending upon compaction and percentage of clay (adapted from CIRIA <i>et al.</i> , 2013)..... | 31 |
| Table 6. | Ranges of hydraulic parameters typically attained during full-scale experiments (Thornton and Beasley, 2013). | 47 |
| Table 7. | Hewlett <i>et al.</i> experimental values: combination of velocity and overflow duration for three qualities of grass cover (Dean <i>et al.</i> , 2010). | 52 |
| Table 8. | Threshold velocities, erosion limits, and velocity errors related to excess work index for the three grass qualities (adapted from Dean <i>et al.</i> , 2010)..... | 54 |
| Table 9. | Threshold velocities, erosion limits, and velocity errors related to excess work index for the Hewlett <i>et al.</i> (1987) mat curves (adapted from Hughes, 2011). .. | 57 |
| Table 10. | Specific discharge, flow thickness, velocity and maximum permissible shear stress estimates for partially vegetated conditions..... | 61 |
| Table 11. | Maximum flume capabilities in terms of: discharge, flow thickness, velocity and shear stress values related to a reinforced fully vegetated lining..... | 62 |
| Table 12. | Characteristics of the sediments used in the experiments. | 80 |
| Table 13. | Product details of RECPs used for laboratory experiments. | 83 |
| Table 14. | Mechanical properties of the RECPs used in the overtopping tests. | 87 |
| Table 15. | Maximum design permissible shear stress and maximum design permissible velocity values of TRMs M ₅ and M ₆ | 88 |
| Table 16. | Measured discharge values and the various overflow durations for phase I. ... | 96 |
| Table 17. | Measured discharge values and the various overflow durations for phase II. ... | 97 |

| | | |
|-----------|--|-----|
| Table 18. | Measured discharge values and the various overflow durations for phase III. | 98 |
| Table 19. | Estimation of critical shear stress according to equation (50)..... | 99 |
| Table 20. | Estimation of critical shear stress of gravel beds according to Shields..... | 99 |
| Table 21. | Evaluation of sediment motion for gravel bed s.A for each discharge. | 100 |
| Table 22. | Evaluation of sediment motion for gravel bed s.B for each discharge..... | 101 |
| Table 23. | Evaluation of sediment motion for gravel bed s.C for each discharge..... | 101 |
| Table 24. | Values of the discharge measured when sediment motion begins to occur, associated with the granular top layer over the RECP. Part one of the experiments. | 112 |
| Table 25. | Values of the discharge measured when sediment motion occurs beneath the mats. Part two of the experiments. | 113 |
| Table 26. | Values of the discharge measured when sediment motion occurs during part three of the experiment and comparison with thresholds values of part two. | 114 |
| Table 27. | Data collection: discharge values set in flowmeter; data log collected with the velocimeter; and order of magnitude of flow thickness. | 118 |
| Table 28. | Testing results calculated from de data collected from the experiments. | 119 |
| Table 29. | Comparison between the measured mean flow velocity and mean velocity according equation (10)..... | 124 |

LIST OF VARIABLES AND SYMBOLS

| Symbol | Description | [Unit] |
|---------------|--|--------------------------|
| A | Cross-sectional breach flow area | [m ²] |
| b | Bottom breach width | [m] |
| B | Depth-averaged channel/breach width | [m] |
| B_w | Breach width at water surface | [m] |
| c | Celerity propagation of waves | [m/s] |
| C | Chézy coefficient | [m ^(1/2) /s] |
| $C\%$ | Percentage of clay in soil | [%] |
| C_f | Empirical coefficient | [-] |
| d | Water depth at the breach | [m] |
| D^* | Non-dimensional grain size | [-] |
| D_{50} | Median particle diameter, grain size not exceeded by 50% of the mass of the bed sediment | [m] |
| D_{75} | Grain size at which 75% of the grains are smaller | [m] |
| d_c | Critical water depth at the breach channel | [m] |
| D_{max} | Maximum grain size of a granular sample | [mm] |
| D_{min} | Minimum grain size of a granular sample | [mm] |
| d_n | Normal water depth at the breach | [m] |
| d_s | Average flow thickness on landside slope | [m] |
| D_{total} | Duration of the overflow test | [hr:min] |
| E | Erosion rate of soil | [m/s]/[mm/hr] |
| E_g | Pick-up rate of granular soil particles | [kg/s·m ²] |
| E_u | Erosion rate proportional to excess velocity | [m ³ /s/m] |
| E_w | Erosion rate proportional to excess work | [m ³ /s/m] |
| E_τ | Erosion rate proportional to excess shear stress | [m ³ /s/m] |
| f_D | Weisbach-Darcy Friction Factor | [-] |
| Fr | Froude number | [-] |
| Fr_n | Froude number at the breach channel (at $x=l_n$) | [-] |
| g | Acceleration of gravity | [m ² /s] |
| G | Gravity force | [N·(m/kg) ²] |
| γ_w | Specific weight of water | [N/m ³] |
| H | Upstream head | [m] |
| h, h_w | Waterflow thickness | [m] |
| h_0 | Uniform (or normal) waterflow thickness | [m] |
| h_1 | Instantaneous flow thickness at upstream location | [m] |

| | | |
|---------------------|---|------------------------|
| h_2 | Instantaneous flow thickness at downstream location | [m] |
| h_c | Critical waterflow thickness | [m] |
| H_w, SWL, SSE | Outside water level, still water level (upstream side) or storm surge elevation | [m] |
| $h_{w,max}$ | Upper limit of the range of values of measured flow thickness | [m] |
| $h_{w,min}$ | Lower limit of the range of values of measured flow thickness | [m] |
| $h_{w,p}$ | Predicted uniform flow thickness | [m] |
| k | von Karman's constant | [-] |
| K | Strickler's coefficient | [m ^{1/3} /s] |
| k_d | Empirical coefficient | [-] |
| K_d | Soil erodibility coefficient | [cm ³ /N·s] |
| K_u | Proportionality coefficient for excess velocity | [m/s] |
| k_v | Empirical coefficient | [-] |
| K_W | Proportionality coefficient for excess work | [m ³ /kg] |
| K_τ | Proportionality coefficient for excess shear stress | [m ² ·s/kg] |
| L | Length of landside slope | [m] |
| l_n | Adaptation length of the waterflow | [m] |
| m | Discharge coefficient | [-] |
| n | Manning's roughness coefficient | [s/m ^{1/3}] |
| N | Propeller revolutions per second | [Rev/s] |
| n_{max} | Upper limit of the range of values of Manning's n | [s/m ^{1/3}] |
| n_{min} | Lower limit of the range of values of Manning's n | [s/m ^{1/3}] |
| $Opt\ WC$ | Optimum water content | [%] |
| q, q_s | Steady overflow discharge per unit length | [m ³ /s/m] |
| q_1 | Unit threshold discharge for incipient motion of granular top layer | [l/s/m] |
| Q_1 | Threshold discharge for incipient motion of granular top layer | [l/s] |
| q_2 | Unit threshold discharge for incipient motion of granular bottom layer | [l/s/m] |
| Q_2 | Threshold discharge for incipient motion of granular bottom layer | [l/s] |
| q_3 | Unit threshold discharge for incipient motion of granular layer | [l/s/m] |
| Q_3 | Threshold discharge for incipient motion of bare granular layer | [l/s] |
| Q_{br} | Breach flow discharge at dike crest | [m ³ /s] |
| q_c | Steady flow critical discharge per unit length | [m ³ /s/m] |
| $q_{flowmeter}, q$ | Unit discharge measured by the flowmeter | [l/s/m] |
| $Q_{flowmeters}, Q$ | Water discharge measured by the flowmeter | [l/s] |

| | | |
|-----------------------|--|-----------------------|
| q_{max} | Upper limit of the range of values of unit discharge, $q_{max}=h_{w,max} \cdot U_{velocimeter}$ | [m ³ /s/m] |
| Q_{max} | Maximum discharge provided by the pump | [l/s] |
| q_{min} | Lower limit of the range of values of unit discharge, $q_{min}=h_{w,min} \cdot U_{velocimeter}$ | [m ³ /s/m] |
| R | Hydraulic radius | [m] |
| $ -R_c $ | Crest freeboard | [m] |
| R_i | Propeller revolutions | [Rev] |
| R_n | Hydraulic radius at the breach channel | [m] |
| s | Landside slope-parallel coordinate | [m] |
| S | Energy slope | [m/m] |
| $s_{2,1}$ | Distance along slope between upstream and downstream location | [m] |
| t | Time or overflow duration | [s] |
| u | Instantaneous slope-parallel flow velocity | [m/s] |
| U | Depth-averaged horizontal flow velocity | [m/s] |
| $u(z)$ | Logarithmic vertical velocity profile | [m/s] |
| $u_{(z=0.37h)}^{max}$ | Upper limit of the range of values of average velocity | [m/s] |
| $u_{(z=0.37h)}^{min}$ | Lower limit of the range of values of average velocity | [m/s] |
| $u_{(z=h)}^{max}$ | Upper limit of the range of values of velocity at the surface of water column | [m/s] |
| $u_{(z=h)}^{min}$ | Lower limit of the range of values of velocity at the surface of water column | [m/s] |
| u^* | Shear velocity | [m/s] |
| u^*_{max} | Upper limit of the range of values of shear velocity | [m/s] |
| u^*_{min} | Lower limit of the range of values of shear velocity | [m/s] |
| U_0 | Depth-averaged horizontal terminal flow velocity | [m/s] |
| u_1 | Instantaneous slope-parallel flow velocity at upstream location | [m/s] |
| u_2 | Instantaneous slope-parallel flow velocity at downstream location | [m/s] |
| U_c | Depth-averaged horizontal critical flow velocity | [m/s] |
| $u_{c,u}$ | Critical threshold velocity for excess velocity assumption | [m/s] |
| $u_{c,W}$ | Critical threshold velocity for excess work assumption | [m/s] |
| $u_{c,\tau}$ | Critical threshold velocity for excess shear stress assumption | [m/s] |
| u_{max} | Maximum velocity at the surface of the vertical velocity profile | [m/s] |
| U_n | Terminal mean flow velocity at the breach channel | [m/s] |
| $U_{velocimeter}$ | Measured velocity by the velocimeter | [m/s] |
| v_s | Steady velocity on landside slope with vegetated HPTRM | [m/s] |

| | | |
|-------------------------|--|---|
| w | Dike crest width | [m] |
| W | Steady overflow stream power unit area | [N·m/s/m ²] |
| WA_{24} | Water absorption of the soil particles in 24 hr | [%] |
| W_c | Critical threshold overflow stream power unit area | [N·m/s/m ²] |
| WC | Water content (or moisture content) | [%] |
| W_L | Liquid limit | [%] |
| z | Normal distance above the channel bed for vertical flow distribution within flow depth | [m] |
| z_0 | Reference level near the channel bed of vertical velocity profile | [m/s] |
| Z_{br} | Elevation of breach bottom at the dike crest | [m] |
| α_τ | Shear stress proportionality coefficient | [kg/m ³] |
| β_0 | Inclination angle of dike/hydraulic model landside slope | [rad]/[°] |
| β_W | Work proportionality coefficient | [kg/m ³] |
| γ | Inclination angle of breach side-slopes | [°] |
| γ_w | Specific weight of water | [N/m ³] |
| Δx | Slope element of length | [m] |
| ρ_d | Dry density of soil particles | [Mg/m ³]/[kg/m ³] |
| ρ_s | Density of soil particles | [kg/m ³] |
| ρ_{sat} | Saturated density of soil particles | [kg/m ³] |
| ρ_w | Density of water | [Mg/m ³]/[kg/m ³] |
| τ_0, τ_b | Shear stress at the bed channel | [N/m ²] |
| $\tau_{0,mean}$ | Mean shear stress (over a distance) | [N/m ²] |
| $(\tau_{0,mean})_{max}$ | Maximum mean shear stress at uniform flow | [N/m ²] |
| $\tau_{0,p}$ | Predicted shear stress at the granular bed layer | [N/m ²] |
| $\tau_{b,cr}$ | Critical shear stress of the sediment according to Shields | [N/m ²] |
| $\tau_{b,max}$ | Upper limit of the range of values of bed shear stress (uniform flow conditions) | [N/m ²] |
| $\tau_{b,min}$ | Lower limit of the range of values of bed shear stress (uniform flow conditions) | [N/m ²] |
| τ_c | Critical shear stress of bed channel material | [N/m ²] |
| $\tau_{c,soil}$ | Critical shear stress of the sediment according to equation (10) | [N/m ²] |
| ν | Viscosity kinematic coefficient | [m ² /s] |
| Ψ_{cr} | Shields parameter | [-] |

ACRONYMS

| | |
|---------|--|
| ACB | Articulated Concrete Block |
| ADV | Acoustic Doppler Velocimeter |
| ARVS | Anchored Reinforced Vegetation System |
| ASABE | American Society of Agricultural and Biological Engineers |
| ASCE | American Society for Civil Engineers |
| ASTM | American Society of Civil Engineers |
| CIRIA | Construction Industry Research and Information Association |
| CSLI | Clopper Soil Loss Index |
| ECB | Erosion Control Blanket |
| ECTC | Erosion Control Technology Counsel |
| EFA | Erosion Function Apparatus |
| EurOtop | European Overtopping manual |
| FEMA | Federal Emergency Management Agency |
| FHWA | Federal Highway Administration |
| HPTRM | High Performance Turf Reinforcement Mat |
| JET | Jet Erosion Test |
| LDV | Laser Doppler Velocimeter |
| PMF | Probable Maximum Flood |
| RCC | Rolled Compacted Concrete |
| RECP | Rolled Erosion Control Product |
| SERRI | Southeast Region Research Initiative |
| TAW | Technical Advisory Committee on Flood Defences |
| TRM | Turf Reinforcement Mat |
| USACE | US Army Corps of Engineers |
| USCS | Unified Soil Classification System |
| USDA | US Department of Agriculture |

1. INTRODUCTION

1.1. General context and motivation

Earthen dikes (also called earthen levees or flood defence embankments) are built all over the world, both in coastal (coastal dikes) and inland areas (riverine dikes), to protect population and infrastructures from high water levels due to storm surges and seasonal floods. Despite their apparent simplicity, dikes can be surprisingly complex structures (CIRIA *et al.*, 2013).

In theory, dikes should have crest elevations high enough (ample freeboard) to prevent flood/storm surge overflow and/or wave overtopping for any possible storm scenario, however economic constraints frequently impose more feasible dike designs with lower crest elevations. Therefore, the probability of these flood defence dikes to be overtopped occasionally is higher during extreme events, especially for older dike systems (Hughes *et al.*, 2011). Even earthen dikes that currently have sufficient freeboard may be at risk of being subjected to storm surge overflow and/or wave overtopping in the future if the sea level and the occurrence of extreme floods continue to rise (Hughes and Nadal, 2009). Over the past two decades the occurrence of extreme floods due to heavy rainfall and storms has increased, and these extraordinary events will occur even more often in the future, according to the Fourth Intergovernmental Panel on Climate Change Assessment (IPCC, 2007 *in* Pickert *et al.*, 2011).

Overtopping is the most likely reason for dike failure (Haselsteiner *et al.*, 2008). Overtopping events can cause erosion of the surface soil layer and may ultimately lead to catastrophic dike breaching with massive flooding on the protected area, as observed during Hurricane Katrina in New Orleans (USA) in 2005 (Hughes and Nadal, 2009). A series of ruptures throughout the entire flood defence system caused the flooding of about 80% of the city for weeks, causing numerous human losses (1118 dead and 135 missing) and economical losses of around 10 million dollars. Post-Katrina investigations concluded that most of the damage occurred on the dike crest and landside slope, as a result of either wave overtopping, storm surge overflow, or a combination of both (ASCE Hurricane Katrina External Review Panel, 2007).

At first sight, raising all the dike crest elevations may be considered the logical solution to limit overtopping events. However, the costs and engineering challenges associated with such intervention would be too great to be accomplished. For that reason, earthen dikes will need to have its crest and landside slope protected with a strengthening system able to resist to the hydrodynamic forces and thus, avoid soil erosion and scour (Hughes and Nadal, 2009). Protecting levees from erosion by surge overflow and wave overtopping is absolutely necessary to assure a viable and safe dike system (Sills *et al.*, 2008 in Amini and Li, 2012). Besides providing flood damage protection, strengthening systems allow to retard the flooding of protected area behind the dike what is translated into a gaining of time for evaluating risk and providing emergency response to the population (Haselsteiner *et al.*, 2008).

In order to evaluate the appropriate slope protection measures in terms of performance and design, estimates of hydrodynamic flow parameters (shear stress, flow velocity, etc.) related with storm surge overflow and wave overtopping (for a specified set of storm parameters) are required. Afterwards, these estimates can be compared with available guidance values for tolerable levels of overtopping, to assess if there is risk of dike failure (Hughes and Nadal, 2009). According to Pullen *et al.* (2007) (eurOtop), the allowable mean overtopping discharge ranges (l/s/m) of earthen dikes are: 50-200 for embankments well protected (crest and slope); 1-10 for grass-covered clay embankments (crest and landside slope); 0.1 for non-protected embankment. This kind of information is one of the main features related with dike assessment and performance that environmental organizations, governments and the scientific community need to know in order to develop series of warning systems, contingency plans and maps of areas at risk of flooding (hazard maps) (CIRIA *et al.*, 2013).

1.2.Objectives

The primary objective of this dissertation is to test the effectiveness of slope protection/strengthening systems consisting of rolled erosion control products (RECPs) (*e.g.*, geogrid, geotextile and turf reinforcement mats (TRMs)) under steady overflowing conditions, created at a full-scale hydraulic model. The experimental work carried out at the hydraulic model is expected to provide more insight into the erosion behaviour of a gravel layer reinforced with a RECP (when facing an overtopping discharge), since the

application of these products are expected to increase its stability and hence, avoid erosion. The purpose of this gravel bed is to simulate the slope surface layer of a flood defence earthen dike. The hydraulic model was used to quantify hydraulic flow properties of a steady overflow (discharge, flow thickness and flow velocity) and estimate hydraulic shear stress on the slope surface material and associated Manning's roughness coefficient, in order to test the suitability of use of each RECP.

1.3. Dissertation structure

This dissertation was structured into four main chapters: 1. Introduction; 2. Earthen dikes; 3. Experimental study; and 4. Summary and conclusions.

The first section presents a general introduction of the theme under study, wherein this dissertation is contextualized in order to clarify its relevance to the reader. The general objectives expected to be accomplished throughout the experimental study are also settled in this part.

The second chapter explains the theoretical framework behind the development of this thesis, based on the conducted literature review. This theoretical framework is structured in eight sub-chapters that share one common denominator, which is being related with flood defence earthen dikes. Section 2.1 introduces existing dikes typologies, the soil materials typically associated with each typology and its structural components. It is also briefly referred the hydraulic loading that different environments can provide to the structure. Section 2.2 explains the mechanisms that can lead to dike failure. Section 2.3 presents the types of overtopping loading that can be inflicted to the flood defence embankment by the surrounding environment. It is placed special emphasis on the hydraulic processes associated with surge-only overflow, including a series of constitutive equations that can be used to estimate hydraulic parameters over the crest and landside slope of a dike. Section 2.4 explains the mechanisms associated with external erosion produced by overflowing water over the dike surface soil material. Depending on the nature of the soil different erodibility formulations are presented. Section 2.5 gives a description of the initiation and growth process of a breach over a dike depending on the nature of the soil (cohesive or non-cohesive). Section 2.6 explains possible applications of earthen dikes reinforced with a surface protection cover within a dike system. Various types of surface protection covers are presented also. Section 2.7 presents some guidance about the

performance of surface protection covers and the basis behind its formulation. Section 2.8 discusses three overtopping experiments undertaken at full-scale physical models to test dike surface protection covers performance.

The third chapter is exclusively related to the experimental study carried out on hydraulic model at the Hydraulic Engineering Laboratory of the Faculty of Civil Engineering of Zagreb (Croatia). Description of the hydraulic model, testing procedures, data collected, and comparison with other experimental works addressed to the same subject, analysis and discussion of the testing results are included in this part.

Finally, the fourth chapter summarizes the output obtained from the laboratory study and respective conclusions. Some considerations are made about the theme under study as well.

2. EARTHEN DIKES

2.1. Factors that affect the erosion process

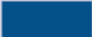


A large number of factors have influence on the process of formation of a breach within the body of an earthfill dike, due to erosion caused by overflowing water. As a matter of fact, it has been observed that in an initial state, the erosion process is triggered by overflowing water at a weak point at the top of the earthfill dike (can occur at other parts of the dike), evolving later to what is herein called a breach (Amini and Li, 2012). The main parameters to be considered are the type of embankment and its constituent material, and the hydraulic loading (Morris *et al.*, 2009). The mentioned parameters are essential to estimate the rate of erosion to which a small initial breach will be exposed during its process of growth in the body of the dike. The present dissertation will be focused on a specific structure type, flood defence structure made of earth.

2.1.1. Types of dikes and constituent material

An earthen dike, as the name says, uses soil as construction material, which will influence its shape and size. The dike body is massive, due to the presence of two slopes, and the crest width is small compared with its height (Figure 1, Figure 2 and Figure 3). The typical cross-section of earthen dikes has not suffered significant changes over the years, displaying: a crest, an earth solid body with an upstream (waterside) and a downstream slope (landside), and a soil foundation on which the structure lays (Schmocker, 2011). Other complementary cross-sectional components include: impermeable core or mask; waterside and landside slope revetments; waterside and landside berms; filter layers; drainage system; relief wells; cut-offs and seepage barriers; and walls. Note that these components are not all necessary in a dike segment to ensure its functionality. The combination of components depends on the hydraulic loading conditions presented. In order to confer dike's functionality, dike components must provide: external protection, stability, impermeability, drainage and filtration (CIRIA *et al.*, 2013). The following table outlines the main functions of the dike components.

Table 1. Functions of dike components (CIRIA *et al.*, 2013).

| Structural components of levees | Existence within levee | Functions of components | | | | |
|---------------------------------|------------------------|-------------------------|-----------|----------------|-----------|------------|
| | | External protection | Stability | Impermeability | Drainage | Filtration |
| Foundation soil | Always present | | Always | | | |
| Earthfill | Always present | | Always | | | |
| Impermeable core | Sometimes present | | | Always | | |
| Impermeable mask | Sometimes present | Sometimes | Sometimes | Always | | Sometimes |
| Crest | Always present | Always | | | Sometimes | |
| Waterside revetment | Sometimes present | Always | Sometimes | Sometimes | | Sometimes |
| Landside revetment | Sometimes present | Always | Sometimes | | Sometimes | |
| Waterside berm | Sometimes present | Always | Always | Sometimes | | Sometimes |
| Landside berm | Sometimes present | | Always | | Sometimes | Sometimes |
| Filter layers | Sometimes present | | | | Sometimes | Always |
| Drainage system | Sometimes present | | | | Always | |
| Relief wells | Sometimes present | | Always | | | |
| Cut-offs and seepage barriers | Sometimes present | | | Always | | |
| Walls | Sometimes present | Sometimes | Sometimes | Sometimes | | Sometimes |

| | | |
|------------|---|--|
| Key |  | Always play a role regarding the function |
| |  | Sometimes play a role regarding the function |
| |  | Not applicable |

This document will give emphasis to the functionality of the external protection component, in particularly the one conferred by the landside revetment and crest.

In most cases, the soil used in the construction of a dike is local, which consequently defines the type of structure to be adopted, so that two categories can be defined (CIRIA *et al.*, 2013): (a) homogeneous earthen dike; (b) zoned earthen dike.

These two typologies of earthen embankments, for flood protection, can vary significantly depending on the country where they are built. For example, a coastal dike built in the United Kingdom, Hungary or France is typically constructed of material excavated on site, presenting cohesive soils composed of materials ranging from clays and silts to sands, and usually has a layer of vegetation (grass cover) to protect the dike surface. On the other hand, countries like Netherlands and Germany have coastal dikes with a traditional configuration containing a core of sand coupled with an outer clay layer (normally with overlying vegetation) that gives impermeability to the embankment (Morris *et al.*, 2009).

Homogeneous earthen dike

A homogeneous dike is considered the simplest one among the wide spectrum of configurations that this kind of structure can assume, since it uses only one type of material that needs to have the ability to form a watertight barrier. However, even this type of earthen dike tends to develop a surface protection layer consisting of vegetation (grass), which will have influence on the breach formation process (Morris *et al.*, 2009). To be able to build a homogeneous embankment, a cohesive and low-permeable material, such as clay or silt, must be used. In areas crossed by rivers or estuaries is common to find this type of structures (CIRIA *et al.*, 2013). Figure 1 presents the main features related to a homogeneous earthen dike cross-section.

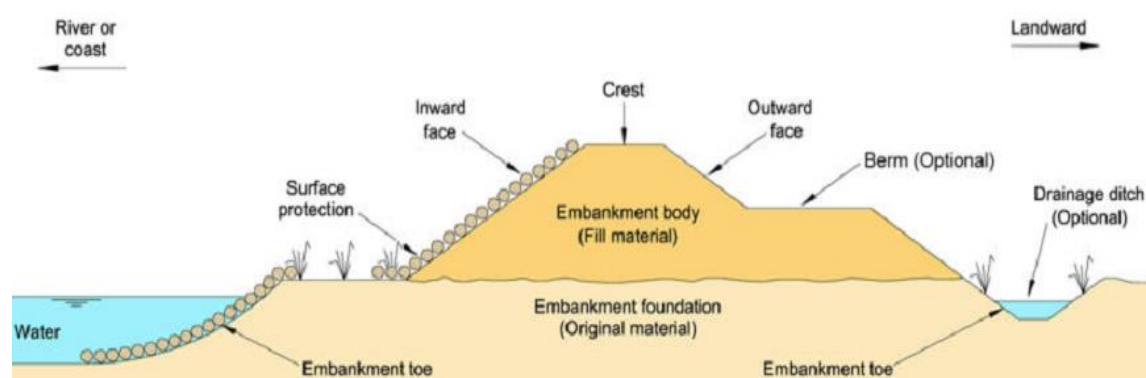


Figure 1. Homogeneous flood defence dike typical of UK (Morris *et al.*, 2009).

Zoned earthen dike

When non-cohesive materials are used in flood defence embankments is necessary to add a waterproof component in order to protect them from the (internal and external) erosion caused by water flow. To achieve this purpose, an impervious core or an impervious mask must be added, so the embankment is no longer considered homogeneous. This kind of structure is commonly called zoned dike which combines permeable material with impermeable material and can display both configurations mentioned above. Dikes with an impervious core (Figure 2) are able to retain water for long periods of time, as dams do (CIRIA *et al.*, 2013).

Geometrically an earthen dike differs from an earth dam in its longitudinal length and cross-section width which are extremely long compared to the crest height (Broere, 1999).

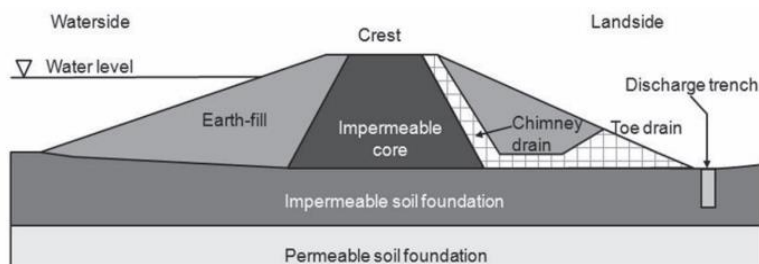


Figure 2. Typical cross-section of a zoned earthen dike containing an impervious core (CIRIA *et al.*, 2013).

The second type of zoned dike is related to the local presence of non-cohesive and permeable material (*e.g.*, sand). Therefore, it is widely used in coastal areas to protect against the inward movement of the sea (CIRIA *et al.*, 2013). In order to provide a certain impermeability and resistance against erosion, a layer of clay is added and positioned at the surface as shown in Figure 3 (Morris *et al.*, 2009).

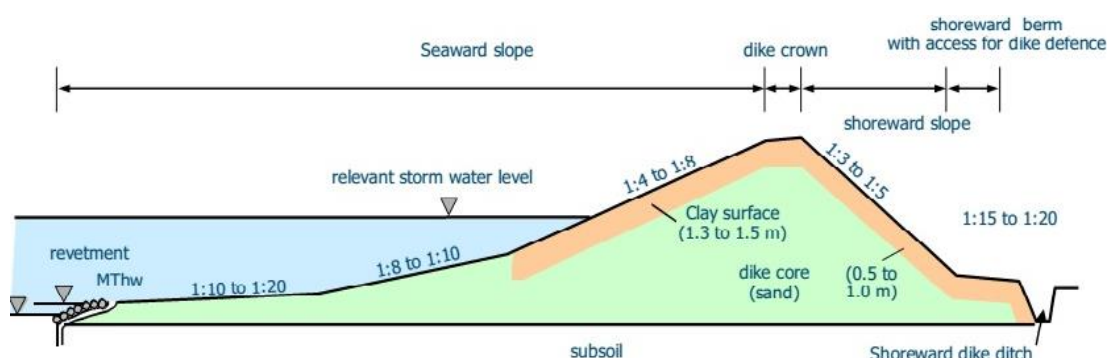


Figure 3. Typical cross-section of a coastal embankment with a surface impervious mask (Morris *et al.*, 2009).

2.1.2. Hydraulic loading

The dikes mentioned above are designed according to certain projected hydraulic loading conditions, imposed by the type of environment (coastal, fluvial or estuary) to fulfil the following basic hydraulic functions: retain water up to a design level; and/or discharge water in a controlled manner; or channelize the flood water to a certain direction (CIRIA *et al.*, 2013). The type of hydraulic load acting on an earthen dike has influence on the failure mechanism by which the structure may collapse and therefore on the breach initiation and growth process. In turn, the type of hydrodynamic loading is dependent on the characteristics of the environment in which the structure is installed which may arise in several ways: water level, local surcharges, waves and currents, as shown in Table 2.

Table 2. Types of hydraulic actions and their relevance in several environments (CIRIA *et al.*, 2013).

| Hydraulic loading characteristic | | Fluvial environment | Coastal environment | Other environments | | | |
|----------------------------------|--------------------------|---------------------|---------------------|--------------------|----------------|--------|----------|
| | | River | (Tidal) sea | Estuary | Lakes | Canals | Torrents |
| Water level ¹⁻⁶ | Flood discharge | ✓ | | | ✓ ³ | ✓ | ✓ |
| | Tide | | ✓ ⁴ | ✓ | | | |
| | Rapid draw-down | ✓ | ✓ | ✓ | ✓ | | ✓ |
| | Storm surge | | ✓ | ✓ | ✓ | | |
| Local surcharges | Wave set-up ⁵ | | ✓ | ✓ | ✓ | | |
| | Seiches | | ✓ | ✓ | ✓ | | |
| Waves ² | | | ✓ | ✓ | ✓ | | |
| Currents | | ✓ | | ✓ | | | ✓ |

Note: Only the main hydraulic load is indicated to each environment.

So, the form of the dike and its components depend on the hydraulic environment where the dike is located and its induced hydrodynamic loadings. For more detailed information see section 2.3.1.

2.2. Earthen dike failure

The understanding of the term ‘failure’ varies from person to person. To a lay person, failure of a flood defence embankment will bring to mind images of large holes with water flowing through it. However, to a flood defence manager, failure may simply mean failure to keep water from reaching the landward side and causing flood damage, rather than catastrophic collapse of the embankment itself (Morris *et al.*, 2009).

Failure mechanisms

An earthen dike failure can be understood as the uncontrolled passage of water flow through the body of the embankment (breaching) or over its crest (decrease of dike crest elevation), due to a loss of significant soil quantities (Morris *et al.*, 2009).

The mechanisms of failure can be divided in two categories; hydraulic rupture and geotechnical rupture (Schmocker, 2011). A failure of hydraulic nature occurs in a situation where water penetrates the polder area (*e.g.*, by seepage, overflow or wave overtopping of the dike) without reaching a critical water level at the upstream side of the dike (planned protection level) and without any element previously damaged (of the dike defence system). A failure with a geotechnical nature consists of creating a breach due to the

geotechnical characteristics of the dike soil material (*e.g.*, slope sliding due to slope macro instability). Figure 4 shows the governing mechanisms of dike failures, of which, the most common causes of failure in earthen dikes are (Singh, 1996 *in* Schmocker, 2011): (1) overflowing/wave overtopping by extreme flood/storm; (2) structural failure due to internal erosion (seepage and piping); (3) structural failure due to slope (macro) instability; (4) structural failure due to problems in the foundation; (5) collapse due to the occurrence of earthquakes; of which points (1) and (2) are the most frequent (Zhu, 2006). However, in most cases the failure occurs as a result of the combination of several causes, which sometimes makes difficult to point out the main cause responsible for the failure of a particular dike (Schmocker, 2011).

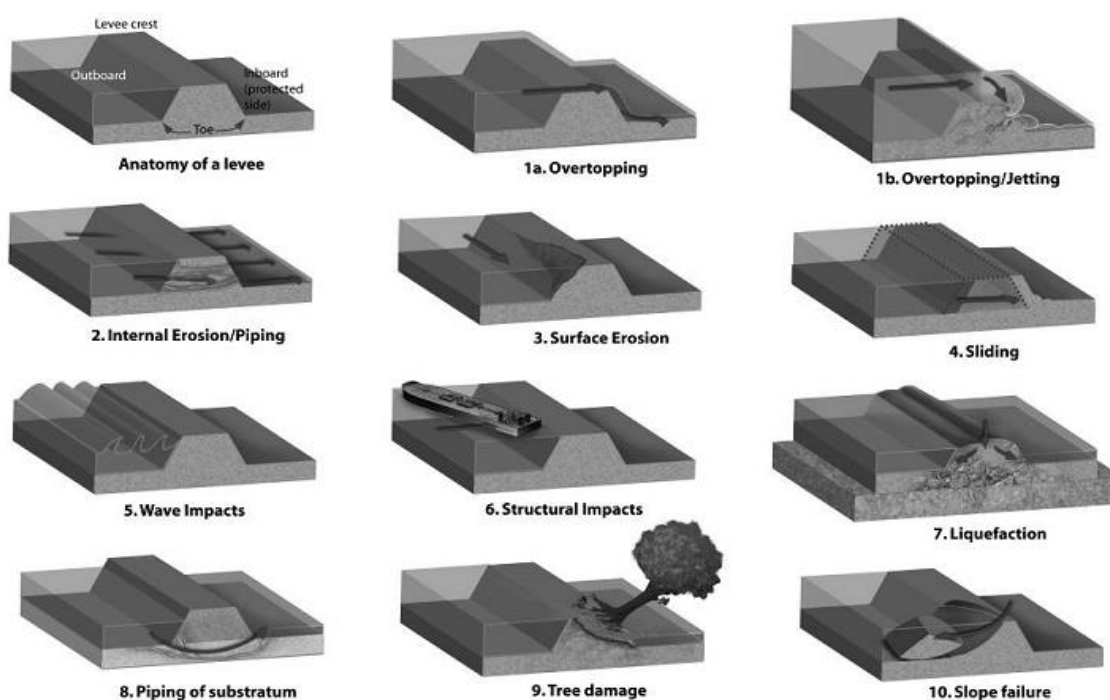


Figure 4. Failure mechanisms of an earthen embankment (Schmocker, 2011).

In the present dissertation attention will be given only to the mechanical surface erosion of the downstream dike slope (and the crest) induced by overtopping. Since the focus is exclusively on overtopping events, the physical mechanisms prior to dike failure are of vital concern, because they induce earthen dike damage.

Earthen dike failure vs earthen dike damage due to overtopping

Overtopping of dikes generates fast-flowing, turbulent water velocities on the landside slope that can damage the protective covering (*e.g.*, grass) and expose the underlying soil

to erosion. If overtopping continues long enough, the erosion may eventually result in loss of dike crest elevation and perhaps breaching of the dike (Hughes and Nadal, 2009), which will conduct to its failure. In other words, damaged dikes can continue to fulfil their designed function of preventing catastrophic flooding. When the damage increases, failure occurs. That is why these two concepts are clearly different and cannot be equated (Hughes, 2011). The fault tree analysis of subsequent damage (that leads to failure) at the landside slope induced by (increased) overtopping is shown in the Figure 5.

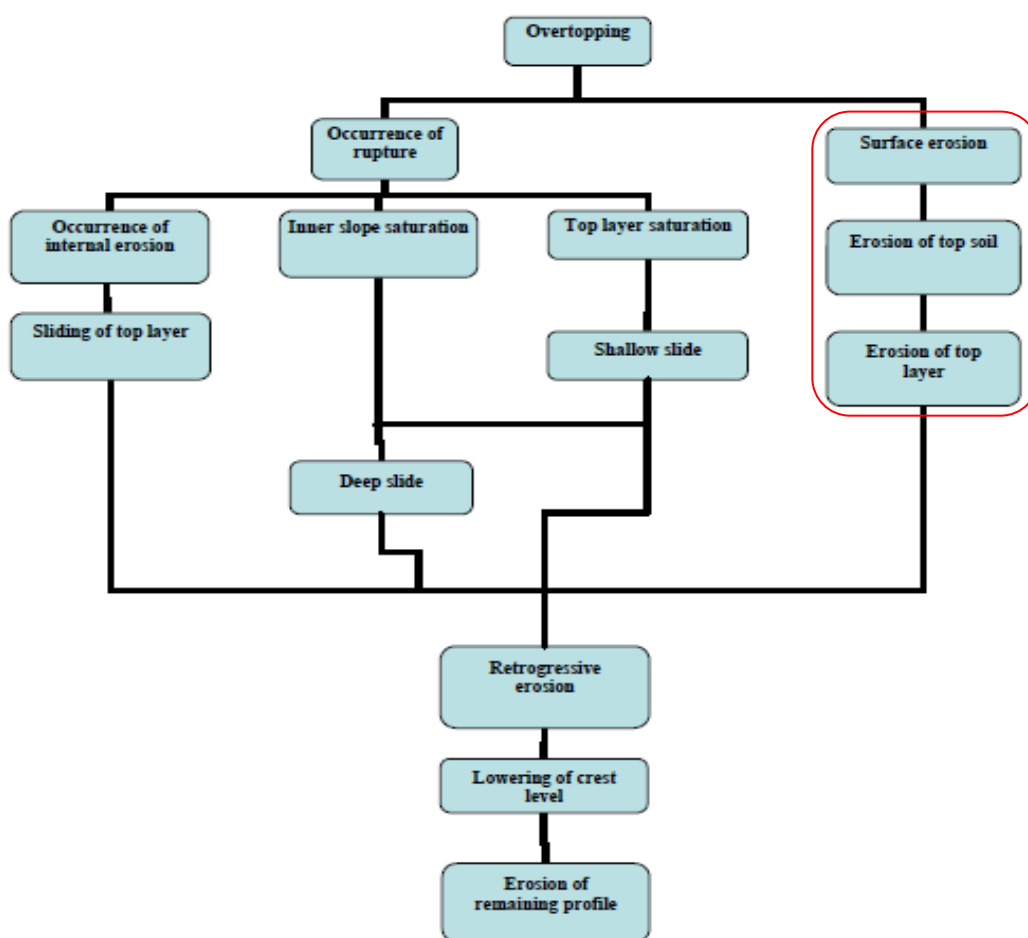


Figure 5. Diagram of dike failure mechanisms by overtopping (van Gerven and Akkerman, 2005).

It can be seen that, apart from ongoing surface erosion, failure can also be deployed by the occurrence of rupture, *i.e.*, (longitudinal) cracks. After a crack, infiltration and consequent saturation of the inner slope will be intensified, after which, part of the slope can slide off (shallow or deep slip). Hence, in case of unprotected slopes initial damage to the surface (erosion or cracks) can cause different subsequent failure mechanisms

(van Gerven and Akkerman, 2005). The only damage mechanism that will be discussed throughout this dissertation is the one represented by the right-most column highlighted with the red rectangular line in Figure 5, related to surface erosion.

2.3. Dike overtopping

With regard to water level, when its elevation is higher than the crest height of the embankment, it is logical that water will flow over the downstream slope. Hence, the downstream slope of the dike acts as a spillway for the overtopping water and damage is caused as a result of water scour (Seed *et al.*, 2006). This phenomenon is called in the scientific literature by overtopping or more specifically overflowing (Visser, 1998). Usually, in the literature the term overtopping may refer actually to wave overtopping and overflowing to steady-state overflow over a dike, and attention should be paid to not misquote these terms. Generally, old dikes were not designed to handle with overtopping water (or to act as spillway). Unless overtopping duration and intensity are limited and the soil material used to build the dike is considerably resistant to erosion or is considered some kind of armouring protection, these flood defence structures can be highly susceptible to catastrophic failure when overtopped (Seed *et al.*, 2006).

According to Broere (1999) the main causes of overtopping can be attributed to the following events: (a) insufficient spillway capacity - a spillway, included in an old dike system, often does not have the ability to discharge safely the waterflow associated to a probable maximum flood (PMF); (b) failure of an upstream dike - for example, if a dike and its reservoir are placed downstream from other dikes, the break of an upstream dike will cause a "domino effect" downstream; (c) landslides - if in the surrounding area a considerable amount of soil or rock slides into the reservoir, a wave of large amplitude can be generated and overtop the dike.

2.3.1. Overtopping types

According to Pullen *et al.* (2007) an overtopping event occurring at a dike can be divided into three types (Figure 6), depending on the elevation and nature of the still water level (SWL) (or storm surge elevation, SSE): (a) surge-only overflow (with negative freeboard); (b) wave-only overtopping (with positive freeboard or zero freeboard); (c) combined wave

overtopping and storm surge overflow (with negative freeboard). Figure 6 compares possible overtopping scenarios for earthen dikes. Note that: Freeboard (R_c) is defined as vertical distance between the sea/river still water level (SWL) and crest elevation; H_s is significant wave height; m is water-side slope; w is width of dike crest.

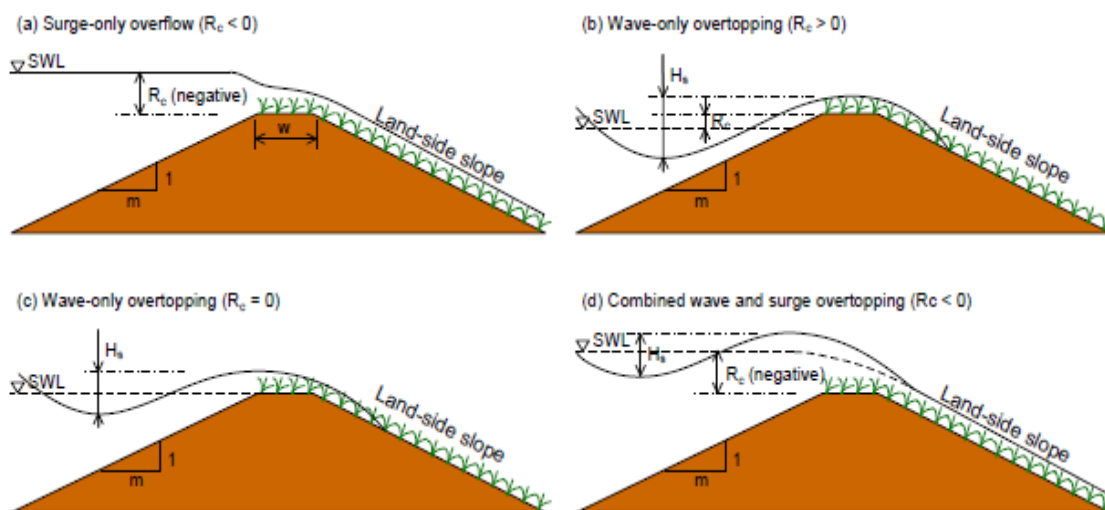


Figure 6. Overtopping types for earthen dikes (Pan *et al.*, 2012): (a) Surge-only overflow ($R_c < 0$); (b) Wave-only overtopping ($R_c > 0$); (c) Wave-only overtopping ($R_c = 0$); (d) Combined wave and surge overtopping ($R_c < 0$).

Surge-only overflow

Surge-only overflow occurs when the still water level exceeds the dike crest elevation and the wave action is inexistent. This event is characterized by a relatively steady flow of water over the dike crest and landside slope and hence the overflow load is relatively constant. The SWL (*i.e.*, average water surface elevation at any instant) may vary slowly in time due to the effect of tide, time-varying surge hydrograph, or long period seiching of a lake or basin. Local variation of water level caused by waves and wave set-up are not taken into account (Hughes *et al.*, 2011). This kind of hydraulic load allows dike's top layer weak parts to settle and consequently, to have its strength increased. Steady state overflow is commonly associated to fluvial/river dikes (Landa, 2014). River flooding may begin with overflow of water into a vulnerable area, following a gradual rise in the water level in the river, caused by high river flow, high sea level and/or high rainfall. This can be predicted with more confidence than coastal flooding (Kortenhaus *et al.*, 2007). An overflow event taking place at earthen dike is similar to overflow of earthen dams and

supercritical flow in channels. Therefore, products developed for these situations have direct applicability to dike surface protection covers. (Hughes, 2008).

Wave-only overtopping

Wave-only overtopping occurs when the surge level is beneath the dike crest elevation or at the same level (zero freeboard). The wave-only overtopping is unsteady in time and spatially non-uniform compared to the surge-only overflow. In other words, wind-generated waves will periodically spill over the crest and hence the crest and landside slope are not constantly under a sheet of water (Hughes *et al.*, 2011). Being subject to a loaded-unloaded cycle causes under and overpressure at the dike surface and does not allow top's layer particles to settle (Landa, 2014). This intermittent/pulsating nature causes a more destructive erosion process on the dike slope surface comparing with the case of a surge-only overflow event, even though these two conditions may have similar average discharge rates (Hughes *et al.*, 2011). According to Hughes and Nadal (2009), when large waves overtop the dike crest they assume a triangular-shaped discharge distribution with a maximum discharge at the leading edge that is several times higher than the time-averaged mean discharge (Figure 7). Nevertheless, wave-only overtopping shares some similar characteristics with surge overflowing such as: the flow velocity increases, until eventually reaches a critical velocity, while flow thickness decreases when the waterflow is moving from an upward position to a downward position along the slope (Hughes *et al.*, 2011).

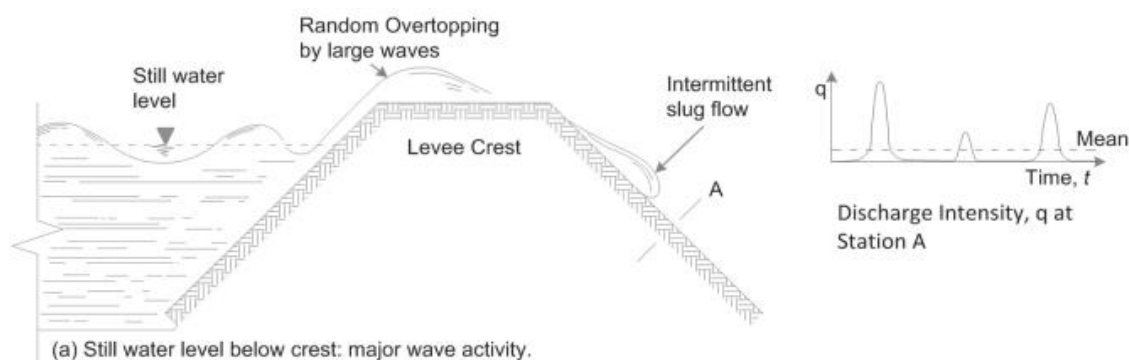


Figure 7. Wave-only overtopping event (with major wave activity) and its associated flood hydrograph (Hewlett *et al.*, 1987 in CIRIA *et al.*, 2013).

Combined wave overtopping and surge overflow

Combined wave overtopping and storm surge overflow occurs when the water level exceeds the dike crest elevation and, at the same time, wind/hurricane-generated waves

provide a pulsing and unsteady component to the waterflow (Figure 8). This overtopping configuration is considered the most destructive, originating an almost continuous unsteady discharge (the peak instantaneous discharge can be several times higher than steady overflow discharge) in which every wave has the possibility to overtop the dike with large peaks in water depth and flow velocity (Hughes *et al.*, 2011).

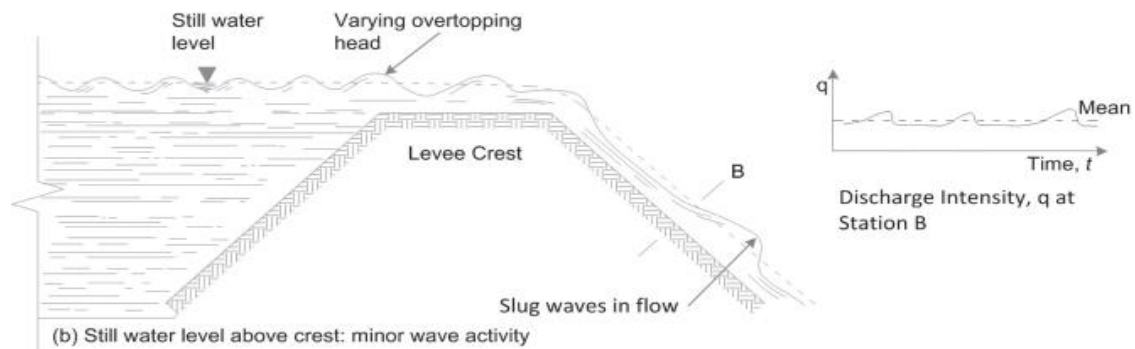


Figure 8. Combined wave overtopping and storm surge overflow (with minor wave activity) event and its associated flood hydrograph (Hewlett *et al.*, 1987 in CIRIA *et al.*, 2013).

2.3.2. Hydraulic processes of surge-only overflow

Surge overflow taking place at a dike can be compared with the two-dimensional steady overflow of a broad-crested weir, considering that the dike crest is at uniform elevation for a substantial distance along the crest and the time variation of the surge elevation is relatively slow compared to wave overtopping (Hughes *et al.*, 2011). Accordingly, the steady overflow discharge per unit of dike crest length can be estimated by the generally accepted equation for flow over a broad-crested weir, provided that frictional energy losses along the crest are minimal (Henderson, 1966 in Hughes *et al.*, 2012):

$$q = \left(\frac{2}{3}\right)^{3/2} \sqrt{g|-R_c^3|} = 0.5443\sqrt{g|-R_c|}^{3/2} \quad (1)$$

where:

q - steady overflow discharge per unit length (at the crest) [$\text{m}^3/\text{s}/\text{m}$],

g - acceleration of gravity [m/s^2],

$|-R_c|$ - crest freeboard (negative) or upstream head H (difference between surge elevation and dike crest elevation) [m].

Froude flow regime classification

According to Powledge *et al.* (1989), during a dike overflow event three distinct flow regimes can be identified (Figure 9): (a) subcritical flow regime - which occurs at high-water side/upstream part of the dike crest and also at the flooded area (landside); (b) critical flow regime - established between the downstream portion of the dike crest and the beginning of the landward slope (near the knick point), if the crest width is sufficiently long to maintain a hydrostatic pressure distribution; (c) supercritical flow regime - which occurs along the downstream slope of the dike, if it is long enough to permit normal (or terminal) flow velocities.

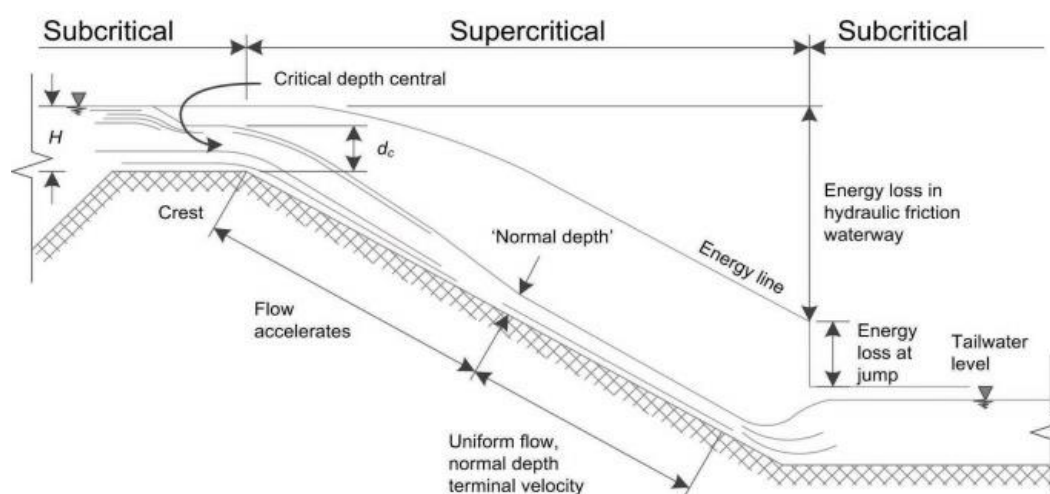


Figure 9. Characterization of steady overflow (flow regime, speed and water depth) over a spillway or dike (CIRIA *et al.*, 2013).

Each flow regime can be represented by its Froude number (Fr):

$$Fr = \frac{U}{gh^{1/2}} \quad (2)$$

where:

U - depth-averaged horizontal flow velocity [m²/s],

h - waterflow thickness [m].

Note that flow thickness in the context of overflow is defined as the thickness of the flowing water perpendicular to dike surface (Hughes *et al.*, 2011).

Fr is defined as the dimensionless ratio between the mean flow velocity (U) and the velocity of wave propagation or celerity [$c=(gh)^{1/2}$]. The celerity is defined as the speed of

a shallow surface wave relative to the speed of the water (CIRIA *et al.*, 2013). Equation (2) can be rewritten as function of unit discharge q :

$$Fr = \frac{q}{(gh^3)^{1/2}} \quad (3)$$

Subcritical regime is a flow condition where Fr is less than unity ($Fr < 1$). This means that water surface flow disturbances can move upstream and hence, the flow is controlled from a downstream point (CIRIA *et al.*, 2013).

When the waterflow is at a critical flow regime (transition between subcritical and supercritical flow) Fr equals to unity ($Fr = 1$) and any disturbance to the surface will be stationary. For this flow condition water depth (h_c), velocity (U_c) and discharge (q_c) are critical and they can be calculated by the following equations:

$$h_c = \frac{2}{3} | -R_c | \quad (4)$$

$$U_c = \sqrt{gh_c} \quad (5)$$

or when equation (5) is substituted for h_c

$$U_c = \sqrt{\frac{2}{3} g | -R_c |} \quad (6)$$

$$q_c = \sqrt{gh_c^3} \quad (7)$$

The supercritical flow regime takes place when Fr is higher than unity ($Fr > 1$) and it is related to a flow condition where downstream flow disturbances do not influence upstream water level (CIRIA *et al.*, 2013). Supercritical flow is attained at the landside slope during the process whereby waterflow accelerates (under the force of gravity) until a normal flow depth is reached at some distance down the slope (considering that the tailwater level on the flooded area is still low and the slope is steep and long enough). Note that when waterflow is accelerating, flow thickness and flow velocity are a function of distance down the landside slope. When uniform flow conditions are reached the flow becomes steady with a normal (or terminal) velocity, as a result of a balance established between the water momentum and the frictional resistance force of the slope surface, at some downstream slope location. The slope-parallel average velocity for fully-developed,

steady uniform flow on the dike landside slope, U_0 , can be calculated using equation (8) (Hughes *et al.*, 2011 and Hughes and Nadal, 2009):

$$U_0 = \left(\frac{\sqrt{\sin \beta_0}}{n} \right)^{3/5} q^{2/5} \quad (8)$$

where:

β_0 - inclination angle of the dike landside slope (Figure 19) [°],

n - Manning's roughness coefficient [$s/m^{1/3}$].

The discharge q (m^2/s) is equal to the steady overflow discharge given by equation (1) because of the mass conservation concept that considers that the discharge is conserved along dike crest and landside slope. The referred hypothesis was proven by Hughes and Shaw (2011) (*in Hughes et al*, 2011). Since the previous equation was derived for mild slopes it may not be strictly valid for steep slopes, where significant air may entrain into the waterflow (Hughes and Nadal, 2009). Typical dike landside slopes are considered steep because $\sin(\beta_0)$ is higher than 0.01 (Henderson, 1966 *in Hughes et al.*, 2011). For comparison purposes, the hydraulic model slope presented in Figure 45 has a value of $\sin(\beta_0)$ equal to 0.243. Equation (8) was derived from the popular flow resistance equation developed by Manning and Strickler:

$$U_0 = \frac{R^{2/3} S^{1/2}}{n} \quad (9)$$

where:

R - hydraulic radius [m],

S - energy slope or slope of the total energy line [m/m].

Equation (8) was derived making three assumptions/considerations: for very wide channels (if $B/h \geq 20$, with B representing the channel's top width) the hydraulic radius, R , can be considered equal to the flowing water thickness h_0 (uniform flow); the slope of the total energy line, S , is the same as the dike slope angle, $S = \tan \beta_0 = \sin \beta_0$; and $h_0 = q/U_0$ (derived from the continuity equation) (Hughes *et al.*, 2011).

Apart from supercritical flow velocity on the landside slope, the hydraulic jump near the toe of downstream slope/transition between the slope and the flooded area is also a concern (the toe/berm of the landside slope is the most common location for the initiation of

erosion). When the tailwater level increases considerably or there is a sudden change in the dike surface inclination (*e.g.*, toe of the dike/flooded area), the water flow suffers a high loss of speed (energy loss) and, subsequently, a hydraulic jump is created (Figure 9). At this location more pronounced erosion will occur due to high velocities and turbulence in the hydraulic jump (CIRIA *et al.*, 2013). The hydraulic jump will move upwards if the tailwater level continues to rise in the flooded or polder area. However, it is not expected a situation where the tailwater level rises until this area is completely inundated (Hughes *et al.*, 2011).

2.3.3. Vertical velocity profile

Flow velocities are not uniformly distributed in a river channel (both transversally and longitudinally) due to the presence of the free surface and friction along the bed and river banks. In fact, the maximum velocity (u_{max}) is approximately 10 to 30 per cent higher than the averaged velocity (U) in the channel cross-section (CIRIA *et al.*, 2013).

The vertical velocity profile for uniform flow conditions can be determined, for a hydraulically rough boundary [$(u^*D)/\nu > 70$ and ν =viscosity kinematic coefficient (m^2/s)], using the following equation (CIRIA *et al.*, 2013):

$$u(z) = \frac{u^*}{k} \ln\left(\frac{z}{z_0}\right) \quad (10)$$

where:

$u(z)$ - (logarithmic) vertical velocity profile [m/s],

u^* - shear velocity, $u^*=(\tau/\rho_w)^{1/2}=(gRS)^{1/2}$ [m/s],

k - von Karman's constant, $k=0.41$,

z - normal distance above the channel bed for vertical flow distribution within flow depth [m],

z_0 - reference level of vertical flow profile ($u(z=z_0)\approx 0$). $z_0=0.033D$ or $z_0=0.033k_s$ [m], where D is the grain diameter of the bed material and k_s is the equivalent grain roughness.

Figure 10 shows the velocity profile in dimensionless logarithmic form.

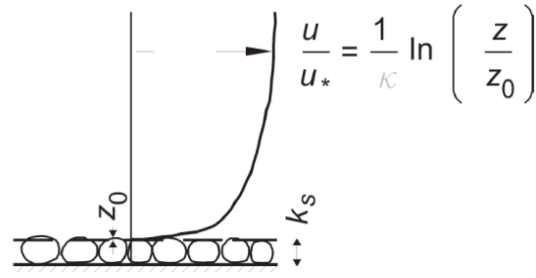


Figure 10. Vertical velocity profile (CIRIA *et al.*, 2013).

According to equation (10) the velocity is very close to its maximum at the water surface boundary, $u_{max} \approx u(z=h)$, and the depth-averaged flow velocity (U) is equal to the velocity $u(z)$ when $z \approx 0.37h$ (CIRIA *et al.*, 2013).

2.3.4. Estimation of the shear stress

The main parameter responsible for sediment transport is the (bed) shear stress. The general expression for the hydrodynamic shear stress (2D) acting on a slope is given by equation (11) (Sturm, 2001 *in* Hughes *et al.*, 2012). This equation is appropriate for unsteady, non-uniform flows on a plane slope that have both convective and temporal accelerations. Therefore it is suitable to estimate instantaneous shear stresses τ_0 (N/m²) provoked by combined wave overtopping and steady overflow (Hughes *et al.*, 2012).

$$\tau_0 = \gamma_w h \left[\sin \beta_0 - \frac{\partial h}{\partial s} \left(\frac{u^2}{2g} \right) - \frac{1}{g} \frac{\partial u}{\partial t} \right] \quad (11)$$

where:

- γ_w - specific weight of water [N/m³],
- s - slope-parallel coordinate [m],
- h - (instantaneous) flow thickness [m],
- u - (instantaneous) slope-parallel velocity [m],
- t - time [s].

In case of steady overflow the temporal acceleration term of equation (11) can be considered null (ignoring turbulent fluctuation), since this loading condition is not time dependent. Accordingly, equation (12) is formed and it is appropriate for steady and non-uniform flows that have into consideration convective accelerations on dike landside slope

(Hughes *et al.*, 2011). As stated before, these flow accelerations take place in a location somewhere between the crest edge and the point where terminal velocity is attained.

$$\tau_0 = \gamma_w h \left[\sin \beta_0 - \frac{\partial h}{\partial s} \left(\frac{u^2}{2g} \right) \right] \quad (12)$$

If the slope is long enough, the terminal velocity is reached and hence there is no more water acceleration. Consequently equation (12) can be simplified to the following equation, appropriate for steady uniform flow conditions and where shear stress is maximum (Hughes *et al.*, 2012):

$$\tau_0 = \gamma_w h \sin \beta_0 \quad (13)$$

This shear stress equation assumes a uniform parallel-stream line flow given by $S = \sin \beta_0$ and $R = h$ ($B/h > 20$). Figure 11 shows a sketch of the hydraulic processes on a bed sloping at a small angle $\alpha = \beta_0$, flow depth h , width B . G is the gravity force and $\tau_b = \tau_0$ is the bed shear stress, both acting on a slope element of length Δx . S_0 denotes the bed slope and $S = S_0$ the energy slope.

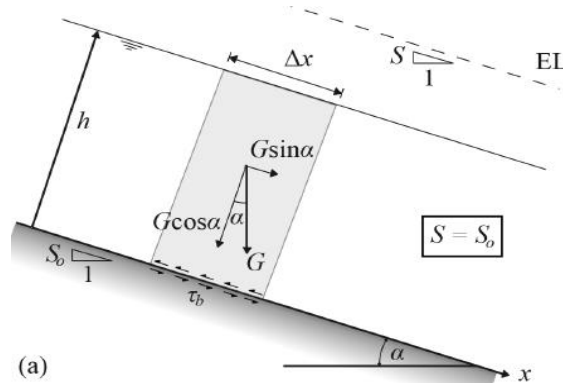


Figure 11. Definition of bed shear stress for uniform flow (Schmocker, 2011).

Note that, if the mean shear stress is calculated according to equation (13), but using values of flow thickness corresponding to a flow acceleration state, the shear stress produced will be conservative, *i.e.*, higher than a situation where terminal velocity is attained. The estimates are conservative because the flow thickness at terminal velocity will be less than the average flow thickness measured when water is still accelerating, for the same discharge value (Hughes *et al.*, 2011).

Estimation of hydrodynamic shear stress over a slope requires synoptic time series measurements of instantaneous flow thickness (perpendicular to dike slope) and flow velocity (parallel to dike slope) at two locations on the landside slope (Hughes *et al.*, 2012). The discrete version of equations (11), (12) and (13) allows to estimate the mean shear stress, occurring between the spatial distance separating the two locations of measurement, for various loading conditions (Hughes *et al.*, 2011). Concerning to the steady overflow (relevant for this dissertation), the discrete version of equation (12) and (13) are, respectively (Hughes *et al.*, 2011):

- shear stress between two locations for non-uniform flow conditions

$$\tau_0 = \gamma_w \left(\frac{h_2 + h_1}{2} \right) \cdot \left[\sin \beta_0 - \frac{h_2 - h_1}{s_{2,1}} \left(\frac{u_2^2 - u_1^2}{2g(s_{2,1})} \right) \right] \quad (14)$$

- shear stress between two locations for uniform flow conditions

$$\tau_0 = \gamma_w \left(\frac{h_2 + h_1}{2} \right) \cdot [\sin \beta_0] \quad (15)$$

where:

- h_1 - (instantaneous) flow thickness at upstream location [m],
- h_2 - (instantaneous) flow thickness at downstream location [m],
- $s_{2,1}$ - distance along slope between two consecutive measurement locations [m],
- u_1 - velocity at upstream location [m/s],
- u_2 - velocity at downstream location [m/s].

A correlation between estimated mean shear stresses ($\tau_{0,mean}$) and average overflow discharges ($q=q_s$) can be established by considering the average discharge as the product of mean flow thickness and mean velocity at each location and assuming that the mean velocity is horizontal and constant over the flow thickness. Hughes *et al.* (2012) find out empirical correlations linking the parameters referred above (measured at two distinct slope locations), as shown by Figure 12. The best-fit equation to the data is represented by the solid line in Figure 12 and is given by equation (16).

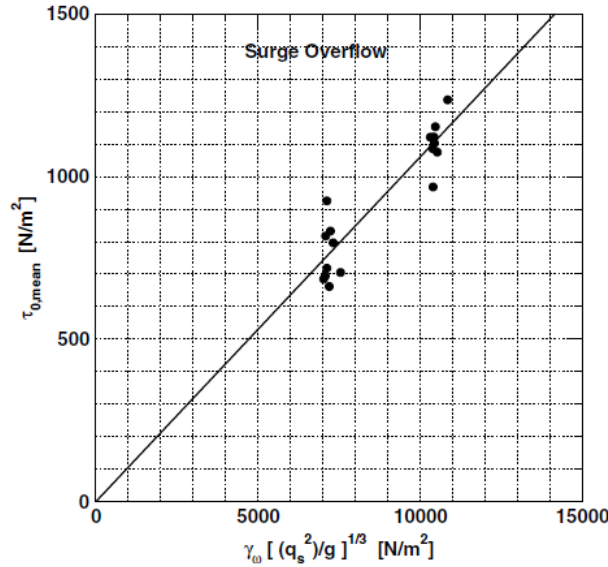


Figure 12. Surge overflow mean shear stress as a function of discharge (prototype scale) (Hughes *et al.*, 2012).

$$\tau_{0,mean} = 0.106 \cdot \gamma_w \left(\frac{q^2}{g} \right)^{1/3} \quad (16)$$

The shear stress time series was calculated according to equation (14) and the average shear stress ($\tau_{0,mean}$) was determined between measurement sections of landside slope where the flow is still accelerating. Thus, $\tau_{0,mean}$ represents the average shear stress over a certain distance at the slope of the hydraulic model. Equation (16) is only valid for landside slopes of 1V:3H having similar roughness as the laboratory model used by Hughes *et al.* (2011). Because the value of q is maintained along the slope for a given condition, the numeric coefficient in equation (16) must be a function of spatial position on the slope (Hughes *et al.*, 2012). It was also calculated the maximum average shear stress $[(\tau_{0,mean})_{max}]$ (that would occur if terminal flow was reached) according to equation (15), but using flow thicknesses associated to water acceleration, to seek correlation with the parameter $\tau_{0,mean}$. The following best-fit equation was found:

$$(\tau_{0,mean})_{max} = 1.41 \cdot \tau_{0,mean} \quad (17)$$

Equation (17) gives a conservative estimate of the maximum shear stress farther down the slope, where terminal velocity is reached (Hughes *et al.*, 2012). It can be noticed that these predictive values are about 40% greater than the estimated mean shear stresses ($\tau_{0,mean}$) of non-uniform flow conditions.

2.3.5. Estimation of manning's n values

Estimates of Manning's n values are given in the literature for different characteristic of channel bottom roughness. It is important to recognize that these estimates assume that waterflow is steady and fully-developed on a constant slope distance (*i.e.*, with terminal velocity) Hughes *et al.* (2011). The following expression is derived from equation (8) and represents Manning's n in terms of steady overflow discharge (q), the mean flow terminal velocity (U_0), and the landside slope angle (β_0):

$$n = \frac{\sqrt{\sin \beta_0}}{U_0^{5/3}} q^{2/3} \quad (18)$$

Manning's n is not constant, it varies with the flow thickness in a proportional relationship. Hughes *et al.* (2011) obtained tested data that confirmed this relationship from small-scale experiments. An increase in velocity up to terminal velocity will result in lower values of Manning's n , for a certain unit discharge q .

Hewlett *et al.* (1987) (*in* Hughes and Nadal, 2009) recommended Manning's roughness coefficient values concerning the steady overflow condition (supercritical regime) for the case of grass-covered slopes. It was recommended $n=0.03$ for slopes of 1:10, decreasing linearly to $n=0.02$ for slopes of 1:3. For landside slopes steeper than 1:3 it was suggested $n=0.02$. This linear relationship can be expressed by equation (19) (Hughes, 2008b):

$$n_{grass} = 0.0343 - 0.043 \tan \beta_o \quad (19)$$

Equation (19) is valid for the range $1/10 < \tan \beta_0 < 1/3$. However, Young and Stone, (1967) (*in* Hughes, 2008b) recommended $n=0.035$ for steep grass slopes.

Manning's n for slope erosion protection systems are determined from measurements in full-scale physical model tests and usually are provided by the manufacturer (Hughes, 2008). Note that Manning's n is always given in IS units [$s/m^{1/3}$].

2.4. External erosion

External (or surface) erosion is the wearing of a surface (bank, streambed, embankment or other surface) by floods, waves, wind or any other natural process (FEMA, 2004).

Incipient motion of sediments – critical shear stress concept

When a flood event happens, hydrodynamic forces, induced by the waterflow, can loosen and remove individual soil particles (or aggregates of particles) at the surface of the dike. These forces cause shear stress at the downstream dike slope (soil boundary), and when its value is higher than the critical shear stress of the dike material (permissible soil shear stress), external erosion is initiated by tearing of surface soil particles (Van Rijn, 1993 *in* CIRIA *et al.*, 2013). The critical bed shear stress for incipient motion is also influenced by other factors, such as particle shape, gradation, bed slope, and the form of the bed (Zhu, 2006). This threshold of erosion is very useful in engineering but it is not obvious that such a clear threshold truly exists physically (Seed *et al.*, 2006).

When the soil surface consists of cohesive materials, cohesive forces (electromagnetic and electrostatic inter-particle forces) between the sediment particles become important. These forces increase the strength of the sediment against flow erosion distinctly. Van Rijn (1993) (*in* Zhu, 2006) pointed out that the type and amount of clay, chemical composition of pore and eroding fluids, presence of organic matter and stress history, etc. are factors that affect critical bed shear stress of cohesive sediments.

Anyway, when the flow velocity is high enough the discharge along the surface imposes dragging on bed slope surface materials (Figure 13) increasing the erosion process.

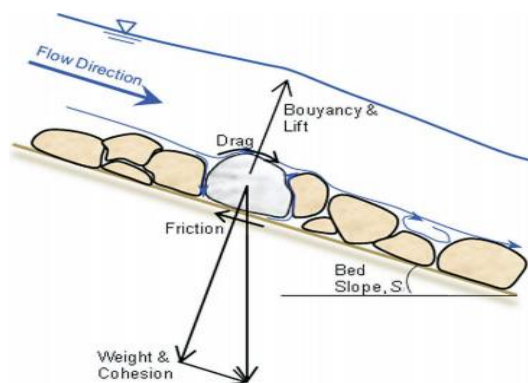


Figure 13. Scheme of forces acting on a submerged particle of a stream bed channel (CIRIA *et al.*, 2013).

Consequently, the thickness and density of the embankment layers will be affected, making the surface less resistant. The process of removal of the layers positioned closer to the surface (with more capability to resist to erosion) implies that less resistant material is exposed, resulting in the acceleration of the entire erosion process (Schmocker, 2011).

It also implies that a percentage of the discharged water will infiltrate, which can cause slope (micro) instability and subsequent sliding, due to saturation and air inclusion. Once these mechanisms of initiation and growth of breaches in the dike body are triggered off, the probability of rupture of the embankment during an extreme event increases significantly (Visser, 1998). The erosion mechanisms are intensified by the removal of sediment from the dike body. Three ways of material removal can be defined (CIRIA *et al.*, 2013): sediment erosion, mass erosion and soil wasting. Sediment erosion occurs when the hydrodynamic forces remove small soil particles from the surface of the embankment being transported in suspension by the waterflow. Mass erosion refers to the removal of small lumps of soil by the action of water flowing in the embankment, especially in points of weakness (*e.g.*, cracked areas). Soil wasting happens when large blocks of material are undercut and slide into the breach waterflow.

The nature of the soil used in the construction of the embankment is another important parameter because it determines the soil susceptibility to erosion. In other words, the soil type defines the rate at which erosion takes place and the type of mechanism associated with breach growth in the body of the earthen embankment (progressive surface erosion or headcut erosion, section 2.5). Therefore, variations in soil type or singularities present in the construction may create points of weakness or higher resistance to the action of erosive agents. Parameters such as the moisture (water) content and soil compaction of the dike constituent material should be considered in (numerical) predictive models of breach formation and growth since they are essential factors to estimate the soil erodibility. The erosion rate on the breach is highly dependent on the soil state in terms of its compaction. A well compacted soil will resist to erosion for a larger period of time than a soil with loose particles (CIRIA *et al.*, 2013). Figure 14 shows how these factors affect the erodibility of the soil (K_d) and it was obtained from an experimental study by Hanson *et al.* (2010). In this study two distinct samples are presented: silty sand (SM) and lean clay (CL). The water content [WC (%)] of the sample for which the soil reaches the highest dry density value (ρ_d), under influence of certain energy of compaction, is defined as the Optimum WC and it can be obtained from the Standard Proctor test (Zhu, 2006). The erodibility parameter K_d ($\text{cm}^3/\text{N}\cdot\text{s}$) reflects the variation in the erosion behaviour of the samples as function of the Optimum WC. According to Hanson *et al.* (2010) (*in* CIRIA *et al.*, 2013) a value of K_d in the range of 100 or superior is typical of an

extremely rapid soil erosion behaviour (silty sand), and a value of K_d ranging from 0.01 to 0.1 is typical of very slow/moderately slow erosion process (lean clay). The other qualitative descriptions given by Hanson *et al.* (2010) included very rapid erosion for $K_d \approx 10$, moderately rapid erosion for $K_d \approx 0.1$ and extremely slow erosion for $K_d \approx 0.001$.

| Embankment Test | Soil Classification ¹ | Sand ¹ > 75 μ m (%) | Fines ¹ > 2 μ m (%) | Fines ¹ < 2 μ m (%) | PI ² |
|-----------------|----------------------------------|--|--|--|-----------------|
| P1 | SM | 64 | 29 | 7 | NP |
| P4 | CL | 25 | 49 | 26 | 17 |

Note: Based on ASTM : ¹D 2487, ²D 4318.

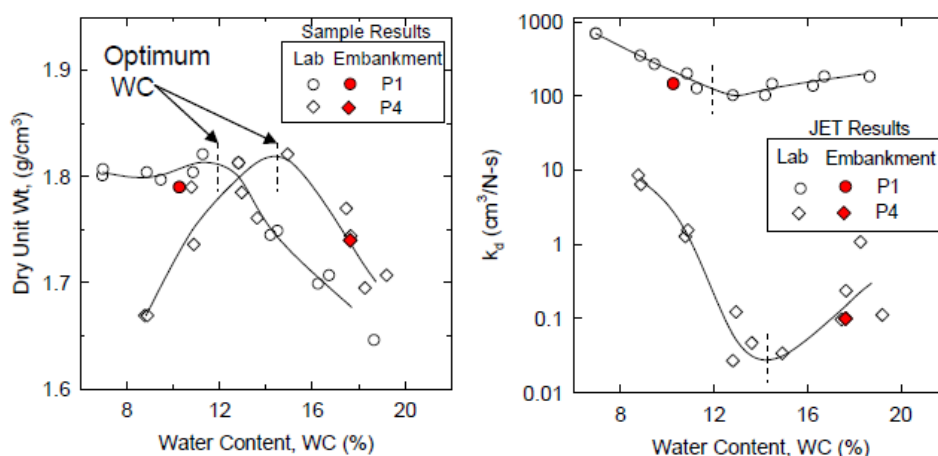


Figure 14. Relationship between soil erodibility [K_d ($\text{cm}^3/\text{N}\cdot\text{s}$)] and compaction water content [WC (%)] for two soil types (SM or CL) (on the right side); and relationship between soil dry density [ρ_d (g/cm^3)] and compaction water content [WC (%)] for two soil types (SM or CL) (on the left side) (Hanson *et al.*, 2010).

A highly erodible soil is, typically, a soil with none or low cohesion and high content of sand ($50 \mu\text{m} < D < 2 \text{ mm}$) and gravel ($D > 2 \text{ mm}$).

A soil that has significant cohesive strength (*i.e.*, large capacity resistance to high shear stresses) and a high percentage of clay particles (especially with high plasticity indexes and low presence of sand, Table 3) can be considered to have good capability to resist external erosion (Morris *et al.*, 2009). Cohesion is only relevant to sediments in the clay ($D < 5 \mu\text{m}$) and silt range ($D < 50 \mu\text{m}$) or fine sand ($D < 250 \mu\text{m}$) with appreciable silt content (CIRIA *et al.*, 2013). Clay can be classified into erosion resistant categories, as shown in Table 3 (Oumeraci *et al.*, 2005).

Table 3. Classification of clay in terms of erosion resistance (TAW, 2006 in Oumeraci *et al.*, 2005).

| CLAY CATEGORY | Water content [%] | Plasticity Index [%] | Sand content [%] |
|------------------------------------|-------------------|-----------------------|------------------|
| 1 – Erosion resistant | > 45 | > 0.73 ($w_L - 20$) | < 40 |
| 2 – Moderately erosion resistant | < 45 | > 18 | < 40 |
| 3 – With little erosion resistance | < 45 | < 18 | > 40 |
| All categories | Organic | Salt | Chalk |
| | < 5% | < 4% | < 25% |

W_L = liquid limit (%); High plasticity index = $W_L \geq 50$ %.

2.4.1. Erodibility of cohesive sediments

Erodibility is a term often used in scour and erosion studies. Briaud *et al.* (2008) defined erodibility of a soil as the relationship between the erosion rate (mm/hr) and the hydraulic shear stress (Pa) and name it erosion function of that soil. This erosion function can be obtained by using a laboratory device called the erosion function apparatus (EFA) (Briaud *et al.*, 2008). The EFA test has been used to test the soil samples (24 samples) collected from the surface of the dikes around New Orleans to provide an erosion chart (Figure 15) for selection of soils with ability to resist to overtopping. In Figure 15 the critical shear stress is defined as the shear stress corresponding to a rate of erosion of 1 mm/hr in the EFA. If the critical shear stress is exceeded, it becomes important to know how fast the soil is eroding at a given velocity (Seed *et al.*, 2006).

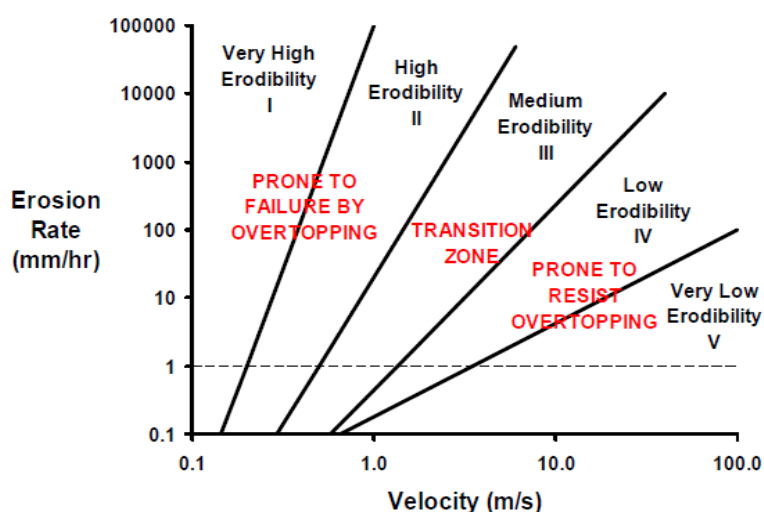


Figure 15. Erosion resistance chart in case of dike overtopping (Briaud *et al.*, 2008).

Note that the erosion chart in Figure 15 relates velocities instead of shear stresses with the soil erosion rate. This is done by Briaud *et al.* (2008) for simplicity's sake in establishing erosion categories. Although erodibility can be represented by the relation between waterflow velocity and corresponding erosion rate, it preferable to quantify the effect of flowing water on soil by using the shear stress applied in soil-water interface, according to Briaud *et al.* (2008). This recommendation lies in the fact that velocity is a vectorial non-unidirectional quantity which is theoretically zero at the soil-water interface, as is explained in Figure 16.

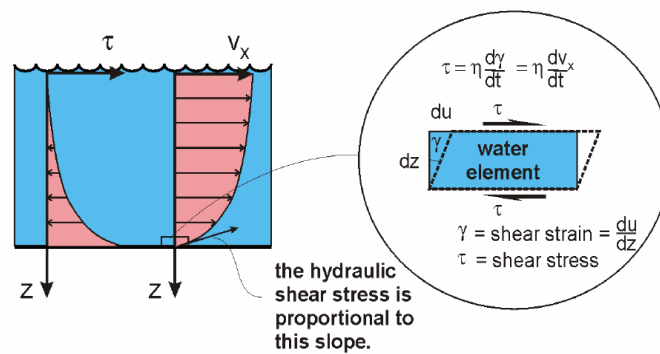


Figure 16. Relationship between flow velocity and shear stress within the flow depth (Briaud *et al.*, 2008).

The following equation was developed by Chen and Anderson (1986) and it is used to estimate the erosion rate during phase I of the breaching erosion process (section 2.5.3). It relates the rate of sediment removal (erosion rate) to shear stress caused by waterflow on the slope's surface. Note that it takes into consideration the soil state (compaction, moisture or water content, etc.) (Hanson and Hunt, 2006).

$$E = K_d (\tau_b - \tau_c) \quad (20)$$

where:

- E - erosion rate (or bulk volume) [$\text{m}^3/\text{m}^2/\text{s}=\text{m/s}$],
- K_d - erodibility coefficient [$\text{cm}^3/\text{N}\cdot\text{s}$],
- τ_b - bed shear stress [$\text{Pa}=\text{N}/\text{m}^2$],
- τ_c - critical shear stress of the bed material [$\text{Pa}=\text{N}/\text{m}^2$].

The effective shear stress at the water-breach soil interface (hydraulic parameter) when the steady overflow reaches the terminal flow velocity (no waterflow acceleration) can be calculated using equation (13) (Zhu, 2006). Note that hydraulic radius is different from

water thickness if the breach channel is “hydraulically narrow” ($B/h < 20$) and therefore equation (13) assumes the following form:

$$\tau_b = (\rho_w g) R \sin \beta_0 \quad (21)$$

where:

ρ_w - water density [kg/m^3].

Note: the specific weight of water is equal to: $\gamma_w = \rho_w g = 9810$ [N/m^3] and $\sin(\beta_0) = S$.

The other variables to be determined are the coefficient of erodibility and the critical shear stress (soil parameters). The coefficient K_d (can be estimated by equation (22) which is based on the soil percentage of clay and on the soil density (Temple and Hanson, 1994).

$$K_d = \frac{10\rho_w}{\rho_d} \exp \left[-0.121(C\%)^{0.406} \left(\frac{\rho_d}{\rho_w} \right)^{3.10} \right] \quad (22)$$

where:

$C\%$ - percentage of clay in the soil (weight %),

ρ_w - water density [Mg/m^3],

ρ_d - dry soil density [Mg/m^3].

Since this equation gives approximate results, the best approach to determine this coefficient is using an experimental test, *e.g.*, the Jet Erosion Test (JET) (Hanson and Hunt, 2006). Alternatively, it is possible to estimate the value of K_d from Table 4 according to the percentage of clay and compaction effort applied to soil sample.

Table 4. Approximate values of K_d determined by compaction and percentage of clay (adapted from CIRIA *et al.*, 2013).

| Clay (%) | Modified compaction (27.5 kg-cm/cm ³) | | Standard compaction (6.0 kg-cm/cm ³) | | Low compaction (kg-cm/cm ³) | |
|----------|--|--------------|---|--------------|--|--------------|
| | ≥ Opt WC (%) | < Opt WC (%) | ≥ Opt WC (%) | < Opt WC (%) | ≥ Opt WC (%) | < Opt WC (%) |
| > 25 | 0.05 | 0.5 | 0.1 | 1 | 0.2 | 2 |
| 14-25 | 0.5 | 5 | 1 | 10 | 2 | 20 |
| 8-13 | 5 | 50 | 10 | 100 | 20 | 200 |
| 0-7 | 50 | 200 | 100 | 400 | 200 | 800 |

Optimum water content=Opt WC (%).

The critical shear stress value can be obtained using equation (23) (or making a rough approximation assuming that $\tau_c=0$ (Hanson and Simon, 2001 and CIRIA *et al.*, 2013).

$$K_d = 0.2\tau_c^{-0.5} \tag{23}$$

Another way to estimate this parameter is using Table 5.

Table 5. Approximate values of τ_c (Pa) depending upon compaction and percentage of clay (adapted from CIRIA *et al.*, 2013).

| Clay (%) | Modified compaction (27.5 kg-cm/cm ³) | | Standard compaction (6.0 kg-cm/cm ³) | | Low compaction (kg-cm/cm ³) | |
|----------|--|--------------|---|--------------|--|--------------|
| | ≥ Opt WC (%) | < Opt WC (%) | ≥ Opt WC (%) | < Opt WC (%) | ≥ Opt WC (%) | < Opt WC (%) |
| > 25 | 16 | 0.16 | 4 | 0.04 | 1 | 0.01 |
| 14-25 | 0.16 | 0.01 | 0.04 | 0 | 0.01 | 0 |
| 8-13 | 0.0 | 0 | 0 | 0 | 0 | 0 |
| 0-7 | 0 | 0 | 0 | 0 | 0 | 0 |

Optimum water content=Opt WC (%).

In some cases it is useful to use a qualitative description of the soil erodibility, since it is a concept difficult to measure and with associated uncertainty (CIRIA *et al.*, 2013). Hanson and Simon (2001) define five levels of soil erodibility based on the coefficient of erodibility (K_d) and critical shear stress (τ_c): highly erodible; erodible; moderately resistant; resistant; extremely resistant (Figure 17). As shown in Figure 17 an inverse relationship has been observed between the critical shear stress and the erodibility coefficient.

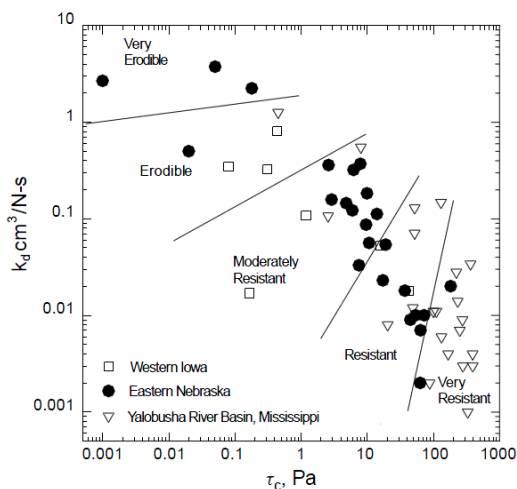


Figure 17. Soil erodibility according to the values of K_d and τ_c of cohesive streambeds (Hanson and Simon, 2001).

2.4.2. Erodibility of non-cohesive sediments

The erodibility of non-cohesive sediment is based on three basic parameters: particle size distribution, density and particle shape. Hence, the submerged weight of the particles (*i.e.*, gravitational forces) confers the main resistance to erosion by waterflow.

An empirical pick-up function has been proposed by Van Rijn (1984) (*in* Zhu, 2006) as a conclusion of the experimental studies carried out in a flume:

$$E_g = 0.00033 \rho_s \left[\left(\frac{\rho_s}{\rho_w} - 1 \right) g D_{50} \right]^{0.5} D_*^{0.3} T_\tau^{1.5} \quad (24)$$

where:

E_g - pick-up rate of granular particles [kg/s·m²],

ρ_s - density of sediment [kg/m³],

D_{50} - median particle diameter (grain size not exceeded by 50% of the mass of the bed sediment) [m].

D_* and T_τ are given by, respectively:

$$D_* = D_{50} \left[\left(\frac{\rho_s}{\rho_w} - 1 \right) / \nu^2 \right]^{1/3} \quad (25)$$

$$T_\tau = (\tau_b - \tau_{b,cr}) / \tau_{b,cr} \quad (26)$$

where:

ν - viscosity kinematic coefficient, $\nu = 1 \times 10^{-6}$ [m²/s].

$\tau_{b,cr}$ - critical shear stress of the sediment according to Shields [N/m²].

Van Rijn (1993) (*in* Zhu, 2006) proposed a method for calculation of suspended load (by rolling, sliding and saltation of particles) and bed load transport where this pick-up rate equation is applied. Nevertheless, here this method will not be discussed specifically.

2.5. Breaching process

Understanding the breach formation process (rate at which a breach forms, volume and rate of release of floodwater, erosion rate, etc.) is essential to obtain a reliable and accurate flood risk assessment with emergency action plans, warning systems and hazard maps. It is

also fundamental to predict the flood hydrograph that develops through the breach (Schmocker, 2011). Depending on the type of soil in which the breach occurs, material with or without cohesiveness, differences can be identified in the physical processes (surface and headcut erosion) induced by the waterflow. A critical point of the breaching process occurs when the dike crest elevation is affected by erosion. The flattening of breach top channel will allow an increased outflow through it and hence, the discharge erosive power will be greater, accelerating the breach growth process (Morris *et al.*, 2009).

Surface erosion

In the presence of a non-cohesive soil, a breach tends to develop by progressive removal of material at the surface in contact with the water. The erosion process will be relatively fast and will affect the landside slope and the crest of the embankment, which will be eroded almost simultaneously. It is expected that rupture occurs more quickly and more catastrophically than in a dike made of cohesive material because the breach crest elevation dramatically lowers and the outflow suddenly increases, given that the soil material is very erodible (Morris *et al.*, 2009).

Headcut erosion

In relation to a cohesive soil, typically, overflowing water will lead to the formation of: various small steps on the slope's surface (small-scale headcuts), in a very early stage of the erosion process (phase I); a single-step/multi-step headcut due to large steepness of the slope, in an advanced stage of the erosion process. This change in slope surface geometry promotes the intensification of turbulence and consequently, intensification of localized erosion spots (local scour) by means of a process called jet impingement, where a water jet coming from the step immediately upstream erodes the head of the downward step (this can happen at a macro and small scale level) (Zhu, 2006).

As mentioned above, the downstream slope becomes progressively steeper, both for materials with or without cohesion. This physical process occurs because the waterflow accelerates along the slope and achieves its largest velocity and hence, its largest erosive power. Typically, the waterflow reaches its highest erosive potential at the toe of the dike or in its vicinity. In addition, also the hydraulic jump contributes to enhance the erosion mechanism, through the turbulence generated in its formation. Therefore, it can be concluded that, in early stage of the erosion process, the maximum rate of erosion is

attained in toe of the dike or nearby and it is probably initiated from there spreading to the upper side later. It is very common that the flow velocity is not high enough at the top of the dike breach to cause erosion or being negligible compared to the one that occurred at the toe of the downstream slope (Zhu, 2006). In the following subchapters will be explained the various stages of the breach growth process in an earthen dike.

2.5.1. Non-cohesive breaching

This chapter will present a more detailed description of the breaching process that develops in a soil without cohesion or with very little cohesion (for instance sand) and that ultimately leads to the collapse of the flood defence structure. The description will be based on the five stages described by Visser (1998) for the breach formation in a sand dike by erosion processes induced by waterflow, used to develop the numerical model BRES. Visser (1998) assumed in his model that, beforehand, there is a small initial breach extending from the crest to the downstream slope of the dike, responsible for releasing the waterflow to the landside area. Visser (1998) also assumed that the initial breach has a trapezoidal cross-section (Figure 22), for simplicity of calculations in the numerical model. In fact, the initial breach, resulting from a given mechanism or a combination of several mechanisms of collapse (overflowing, wave overtopping, seepage, etc.), has an irregular shape and can have a variable size.

The five key stages of the breaching erosion process are (Figure 18):

Phase I – $t_0 \leq t < t_1$: The erosion process starts at $t=t_0$ when the flow drains through the initial breach. Then it is observed the gradual steepening of the channel bottom installed on the downstream slope from the angle β_0 up to the critical angle β_1 , which is approximately equal to the internal friction angle (φ) of the dike constituent material.

Phase II – $t_1 \leq t < t_2$: Under constant angle β_1 at $t=t_1$, the downstream face of the dike starts moving towards the waterside face of the dike - retrograde erosion. This phase ends when the horizontal platform of the crest is completely removed by the waterflow ($t=t_2$). The waterflow being released through the breach starts to increase after the removal of the crest surface.

Phase III – $t_2 \leq t < t_3$: The dike crest decreases in height and subsequently there is an enlargement of the breach. The side slope angle (γ) of the breach channel remains constant

during this process. In $t=t_3$ the breach bottom channel is completely eroded down to the base of the embankment.

Phase IV – $t_3 \leq t < t_4$: Erosion on the dike at this stage is essentially on the breach side slope, as such, the section of the breach expands transversely under a constant angle. The vertical erosion is dependent on the characteristics of erodibility of the dike base. The flow regime at this point is critical.

Phase V – $t_4 \leq t < t_5$: The inlet section of the dike continues to grow laterally, this time, due to the subcritical flow passage. In $t=t_5$ the flow velocity is reduced to levels that do not cause erosion on the soil surface. The flow stops when the water level upstream of the dike has equalled the water level of landside that was originally saved from the flood.

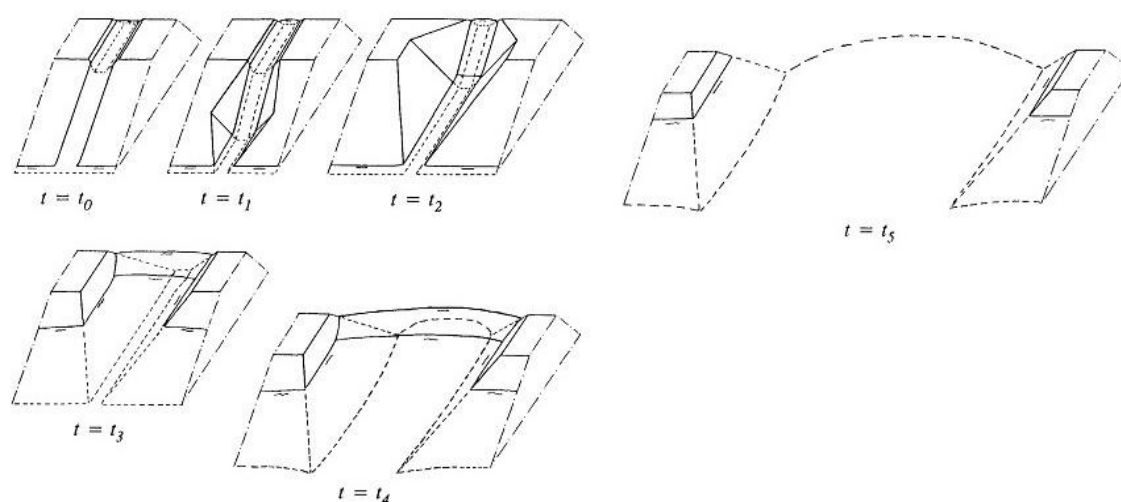


Figure 18. Schematic representation of the breach development (in 5 steps) in a sand dike (Visser, 1998).

2.5.2. Cohesive breaching

It will be outlined in this section a qualitative description of the erosion process in dikes made of cohesive soils, such as dikes mainly made up of clay material. The growth process of a breach is equally divided in five stages, like the division proposed by Visser (1998), and they are included in a new version of the BRES numerical model developed by Zhu (2006), especially for cohesive soils. This five-stage process is divided in (Figure 19 and Figure 20) (Zhu, 2006):

Phase I - $t_0 \leq t < t_1$: In $t=t_0$ starts the breach growth process due to the flow passage through the initial breach. Depending on the flow speed, it can be assumed that either the

top of the dike (much less pronounced) and the downstream slope suffer two types of erosion: the first one related to flow shear forces caused by water discharge (flow shear erosion) and the second one associated to the formation of small steps on the slope surface (small-scale headcut erosion). In $t=t_1$ the angle of inclination is increased from β_0 to a critical value of β_1 (friction angle). Figure 19 shows a schematic representation of Phase I.

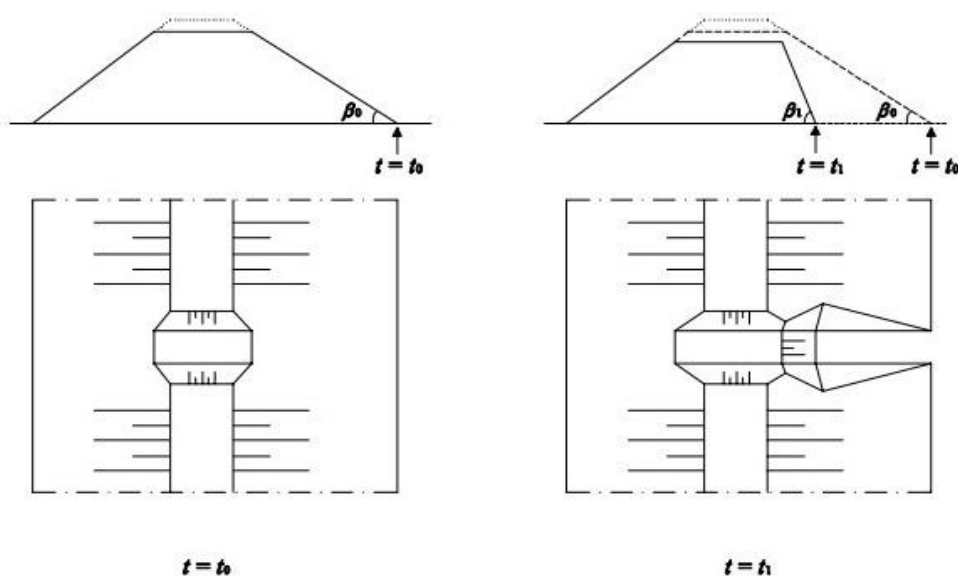


Figure 19. Sketch of the breaching process in phase I (Zhu, 2006).

Phase II - $t_1 \leq t < t_2$: During this phase the slope maintains the inclination angle β_1 which is so high (large steepness) that the earthen dike acts as if it was a big step (headcut) discharging a water jet. This headcut moves towards the upstream face cutting through the downstream face of the dike body and into its crest. The crest elevation starts to lower due to erosion at $t=t_2$ and therefore, in reverse way, the outflow through the breach increases gradually. The erosion of soil material in the breach is related to: the shear stress created by the waterflow; fluidization of the slope surface; discrete headcut slope mass failure; and headcut undermining in the slope disposed under a critical angle.

Phase III - $t_2 \leq t < t_3$: At this point the slope still maintains its steepness and the erosive mechanisms are the same of phase II, but now with greater erosive capacity (*i.e.*, the erosion rate in this phase is higher). This happens due to the fact that the remaining material of the dike body is thinner and more fragile. The breach cross-section also continues to widen, as such the discharge over the embankment increases, which in turn accelerates the entire erosion process. In $t=t_3$ the breach reaches the foundation, being completely transversal to the entire dike body width.

Phase IV - $t_3 \leq t < t_4$: The headcut has cut through the crest and upstream face into the reservoir completely and the erosion becomes, essentially, laterally due to shear stress forces on the sides-slope of the trapezoidal cross-section. The breach enlargement takes place through side-slope instability and subsequent drop of soil masses. Accordingly, the width of the breach continues to grow as a result of a higher discharge.

Phase V - $t_4 \leq t < t_5$: Erosion continues to be mainly laterally, but the erosion rate decreases because the downstream water level rises and suppresses the inflow gradually, reducing its speed. In $t = t_5$ is expected that the flow velocity has no longer the ability to continue the erosion process.

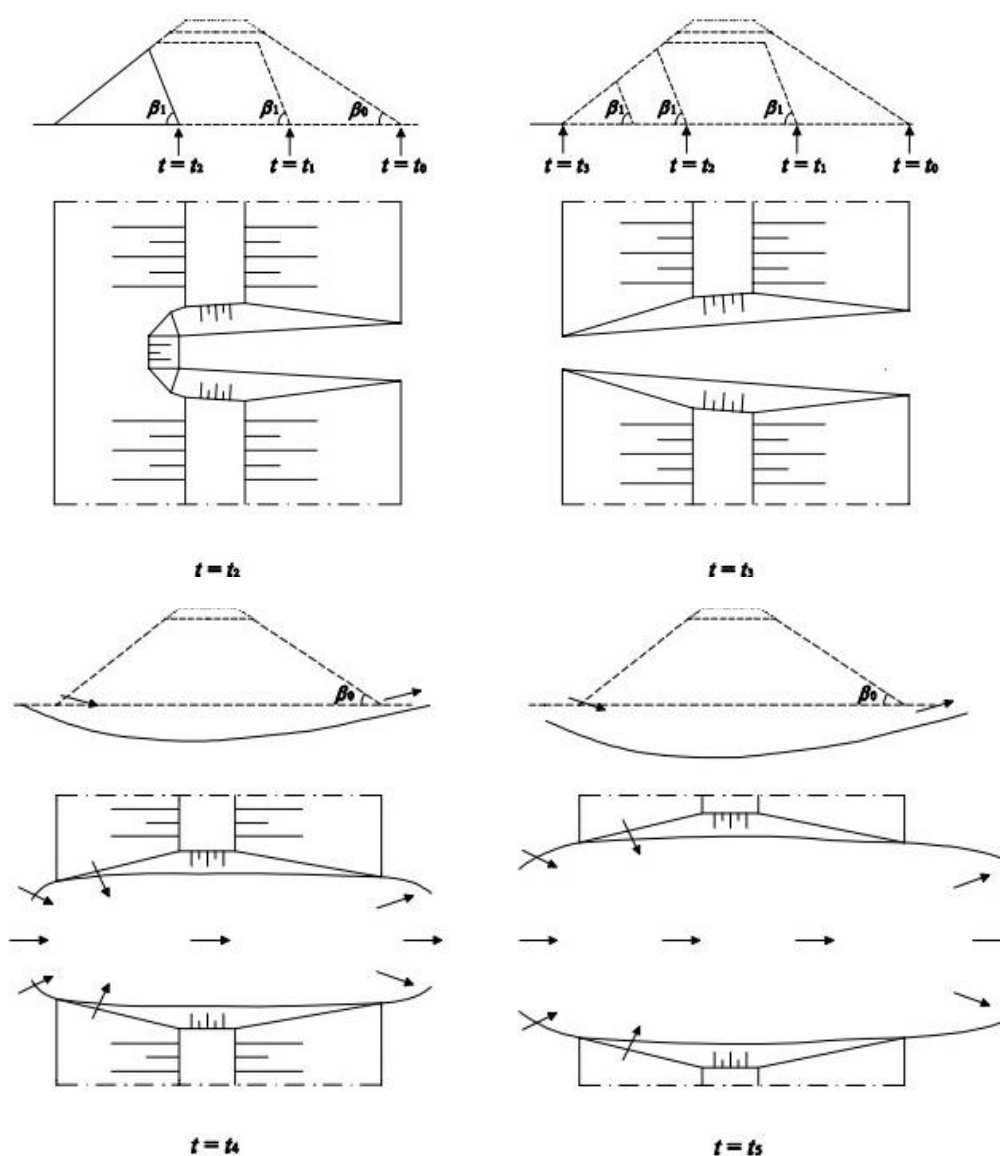


Figure 20. Phases II ($t=t_2$), III ($t=t_3$), IV ($t=t_4$) and V ($t=t_5$) of the breaching process in an embankment with a cohesive soil (Zhu, 2006).

2.5.3. Breach overflow in stage I

This dissertation will focus exclusively on the first stage of the erosion process described by Zhu (2006) (section 2.5.2), inherent to the passage of waterflow through a breach channel formed over the crest and downstream slope of a dike. Therefore, it will be given more emphasis to the mechanisms and physical processes involved in stage I.

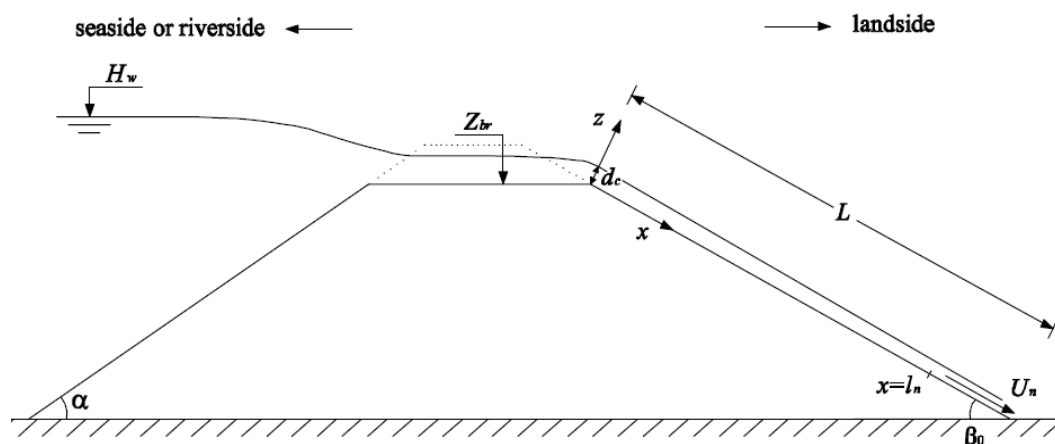


Figure 21. Waterflow on the initial breach channel created on the dike crest and downstream slope of the dike in stage I (Zhu, 2006).

It is relevant to calculate the uniform steady overflow discharge that induces the erosion process at small initial breach over dike crest ($t=t_0$), which can be estimated with a standard broad-crested weir equation used by Visser (1998) and Zhu (2006):

$$Q_{br} = m \left(\frac{2}{3} \right)^{3/2} \sqrt{g} B H^{3/2} \quad (27)$$

where:

Q_{br} - water discharge through the breach at the dike crest [m^3/s],

m - discharge coefficient, $m=1$ (Visser, 1998),

B - depth-averaged breach width (Figure 22) [m],

H - difference between the outside water level (H_w) in the reservoir and the height of the breach bottom (Z_{br}), $H=H_w-Z_{br}$ (Figure 21) [m].

Figure 22 represents the cross-section of the initial breach that the mathematical model BRES (Visser, 1998) assumed that existed on the dike crest, before the breach growth process starts ($t=t_0$). Some geometric breach parameters are also defined.

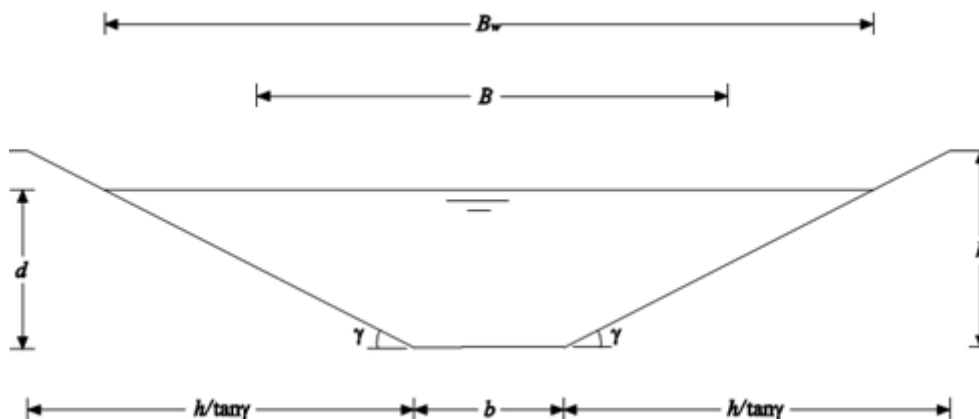


Figure 22. Trapezoidal cross-section of the breach in the dike crest (Zhu, 2006).

The breach width B of a trapezoidal cross-section can be calculated as follows (Figure 22):

$$B = b + \frac{d}{\tan \gamma} \quad (28)$$

where:

- b - width of the breach bottom (smaller base of the trapezoidal section) [m],
- d - flow depth at the breach section at the dike crest and landside slope [m],
- γ - inclination angle of breach side-slopes (Figure 22) [°].

Adaptation length

In phase I water flows through the breach at the landside slope and naturally accelerates until it reaches a normal velocity (U_n). The required distance that the outflow needs to attain the normal velocity is called adaptation length, l_n (Visser, 1998). It is assumed that the length of the landside slope, L (m), is large enough in order to allow the normal (or terminal) velocity to be reached (*i.e.*, $l_n < L$) (Figure 21). The value of l_n can be estimated using equation (29) (Zhu, 2006).

Note that subscript 'n' means that the discharge is done in uniform flow regime conditions.

$$l_n = \frac{2.5(Fr_n^2 - 1)d_n}{\tan \beta_0} \quad (29)$$

where:

- Fr_n - Froude number at $x=l_n$ (Figure 21),
- d_n - normal flow depth at the downstream slope [m].

The Froude number can be calculated by equation (30):

$$Fr_n = \left(\frac{U_n^2 (B_w)_n}{gd_n B_n \cos \beta_0} \right)^{1/2} \quad (30)$$

where:

- U_n - mean flow velocity in the breach cross-section at landside slope [m/s],
 $(B_w)_n$ - breach width at water surface [m].

The value of U_n can be calculated by the following formula, when $x \geq l_n$:

$$U_n = C \sqrt{R_n \sin \beta_0} \quad (31)$$

where:

- C - Chézy coefficient [$m^{(1/2)}/s$],
 R_n - breach hydraulic radius [m].

The value of C can be calculated by Manning's formula (32):

$$C = \frac{1}{n} R_n^{1/6} \quad (32)$$

The parameter R_n for a trapezoidal cross-section is given by the equation (33):

$$R_n = \frac{A}{b + \frac{2d_n}{\sin \gamma}} \quad (33)$$

where:

- A - cross-sectional flow area at the breach [m^2].

The cross-sectional area of the breach is calculated by the expression (34):

$$A = B d_n \quad (34)$$

The water height d_n is calculated by the formula (35) when $x \geq l_n$:

$$d_n = \frac{Q_{br}}{U_n B_n} \quad (35)$$

The breach width at the water surface, B_w , of a trapezoidal cross-section can be calculated as follows (Figure 22):

$$B_w = b + \frac{2d}{\tan \gamma} \quad (36)$$

The critical flow depth, d_c , at the knick point ($x=0$) (Figure 21) is given by the expression (37). Note that the subscript 'c' refers to the critical flow regime.

$$d_c^3 = \frac{Q_{br}^2 (B_w)_c}{g B_c^3 \cos \beta_0} \quad (37)$$

2.6. Surface protection covers

2.6.1. Earthen spillways

Ordinary flood defence embankments along rivers are not usually designed for handling with overflow loads with large durations, except if special designed overflow sections are presented within the dike system (Haselsteiner *et al.*, 2008). When a particular section of a dike is been subjected to an overtopping event it can be considered that the landside slope is acting as a spillway. Therefore, the design of the landside revetment/surface cover (interface between external environment and the dike) needs to have special consideration in order to resist external erosion, infiltration and sliding. The landside toe has also to be designed according to the existence or not of a hydraulic jump (Seed *et al.*, 2006).

Definition

An earthen spillway is a flood defence structure designed to provide a controlled release of water from one area (reservoir) to another over or through it. If the rate of flowing water is controlled by mechanical means, such as gates, it is considered a controlled spillway. If the geometry of the spillway is the only control, it is considered an uncontrolled spillway (FEMA, 2004). An earthen spillway fits into the category of an uncontrolled spillway and it is object of study of the present dissertation. According to Degoutte *et al.* (2012) (*in* CIRIA *et al.*, 2013) two main types of spillways on riverine dikes can be defined: security (or safety) spillways and bypass (or diversion) spillways.

Security spillway

Security spillways allow controlled discharge of water from a reservoir into areas of relatively low risk in order to protect the dike system or dams from failure under overflow

due to excessive water levels, ensuring that the water overtops in the least vulnerable area (*i.e.*, the section designed to resist to overflow erosion). Security spillways are expected to function in rarely occasions where the return period water level for which the neighbouring dikes have been designed is exceeded (CIRIA *et al.*, 2013).

Bypass spillway

Bypass spillways are designed to discharge excessive flood water of main river channel into a particular area: flood detention area (or flood expansion zone, Figure 23) typically surrounded by natural high ground; a secondary river; or a designated floodway. This way part of the river flow is redirect to a safe area for temporary storage and the water levels downstream of the river are reduced. Thereby bypass spillways are normally designed as part of a flood control system that control water levels within a river system, operating more frequently than security spillways (CIRIA *et al.*, 2013).

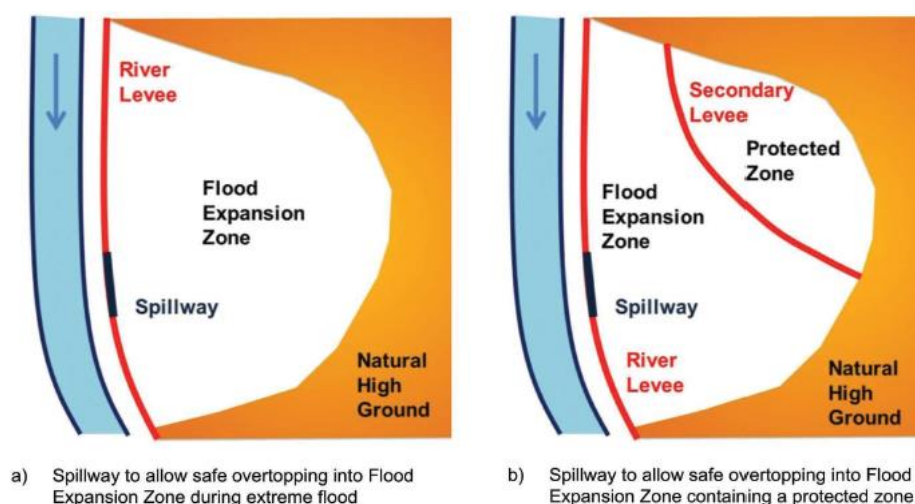


Figure 23. Example of a bypass spillway diverting flood flow towards a flood expansion zone (Degoutte *et al.*, 2012 in CIRIA *et al.*, 2013).

A simple way to create a spillway segment is to adapt a part of an earthen dike (or embankment dam) in order to be able to withstand large amounts of overtopping water. Therefore, the crest and landward slope (and eventually the landward toe) of dike have to be reinforced in order to increase its erosion resistance against overflow.

2.6.2. Strengthening systems for earthen embankments

There are several methods of refurbishment of an earthen embankment in order to be able to withstand overtopping discharges (Figure 24). These methods can be divided into two categories: soft/light armouring and hard or heavy-duty armouring (Miller *et al.*, 2012). Light armouring encompasses natural vegetation (also contains temporary/degradable rolled erosion control products (RECPs) and permanent reinforced vegetation (includes turf reinforcement mats (TRMs), high performance turf reinforcement mats (HPTRMs) and anchored reinforced vegetation systems (ARVSs)). Hard armouring techniques include reinforced concrete slabs, rockfill concrete, rip-rap, reno mattresses, stepped gabions, pre-cast concrete blocks. Figure 24 divides the methods presented in three general groups (vegetation, reinforced vegetation and hard armour techniques) according to threshold values of permissible shear stress and velocity associated with each protection system.

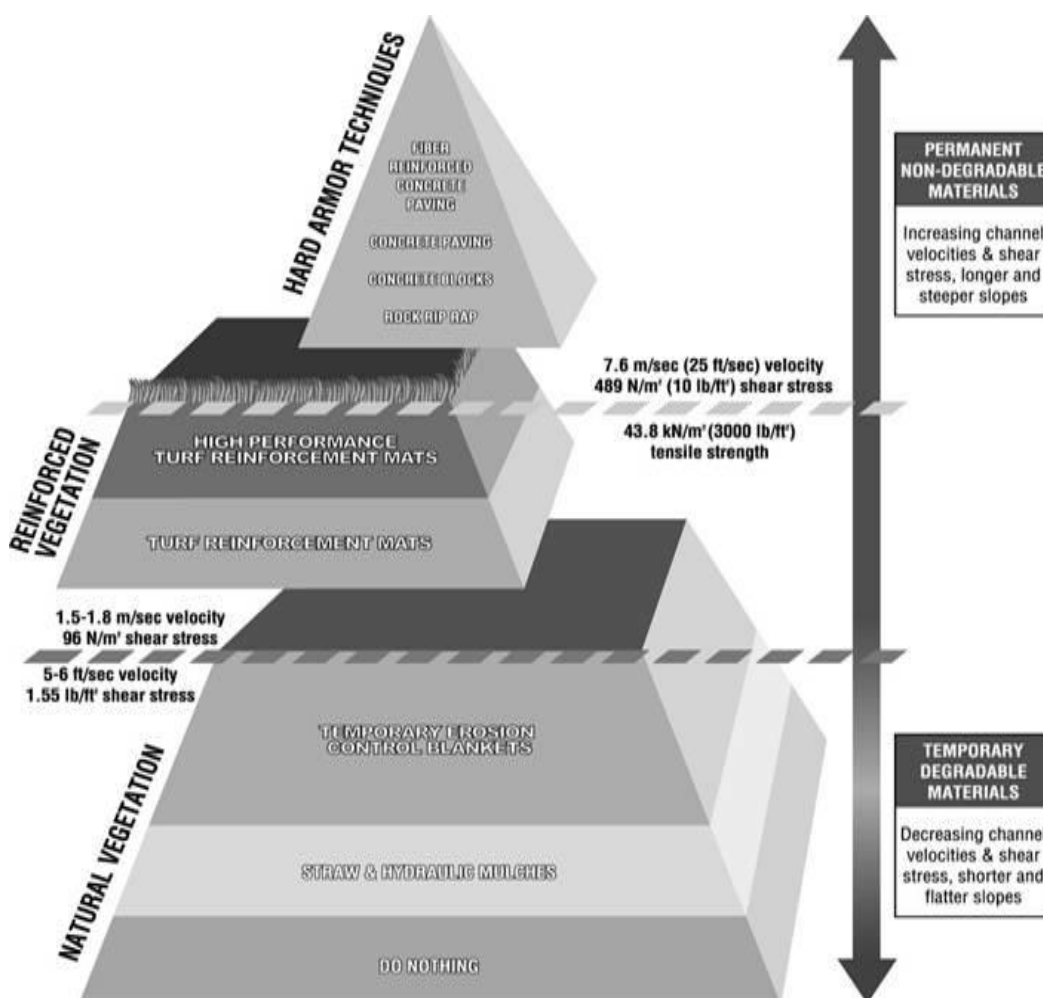


Figure 24. Erosion control reinforcement techniques (Miller *et al.*, 2012).

2.6.2.1. Grass protection cover

Implementation of grass as surface dike cover is the simplest and most common measure used on dikes around the world, particularly for riverine dikes, to protect against erosion. Erosion control is provided in two ways. First and more preponderant, the roots of the grass penetrate the dike surface and create a dense top soil mass of interlocking turf with increased strength and hence, with ability to resist to higher flow velocities than bare soil alone (*i.e.*, surface erosion due to overflowing water) (CIRIA *et al.*, 2013). Second, grass stems helps to dissipate shear force before it reaches the underlying soil surface (Kilgore and Cotton, 2005).

Hanson and Temple (2002) (*in* Amini and Li, 2012b) carry out field tests on steep vegetated and non-vegetated channels subjected to long-duration supercritical flows. Based on their study, the maximum average erosion rate in the unvegetated channel was 25 to 50 times greater than that of the vegetated channel, even though the soil had a measured permissible shear stress of 0.55 N/m^2 .

As long as grass cover is cut relatively regularly and well maintained it may offer an effective and aesthetically form of erosion control to the dike boundaries (within certain threshold conditions where the hydraulic shear stresses do not already exceed stability limits of vegetation) (Figure 29) (CIRIA *et al.*, 2013). Therefore simple grass covered spillways can also be used to convey water into a flood expansion zone during potential flood periods. Its application is best suited to small rivers and rural low-risk environments because grass protection cover work best when conveying water at relatively low velocities and for short durations (Figure 29). In order to make this possible, grass spillways have to be submitted to low overtopping discharges which can be accomplish by providing long lengths to its crest. However it is important to emphasize that long crests are more prone to differential and localized settlement than shorter ones, which can lead to earlier overtopping in these locations rather than others. These lower spots constitute weak points much more vulnerable to preferential erosion due to locally higher velocities. For this reason, grass-covered spillways are best suited as adaptations to existing dikes instead of being used for new dikes. Nevertheless, grass spillways can be considered cost-effective structures due to its simplicity (CIRIA *et al.*, 2013). A common method to allow higher velocities over a grass covered spillway is to reinforce dike grass cover with RECP.

2.6.2.2. Reinforced grass protection cover

This dissertation places emphasis in light armouring protection systems which can provide effective erosion control and reinforcement of the dike surface cover. Typically geosynthetics in form of rolled erosion control products (RECPs) are used to accomplish this function of surface protection. Note that there are other functions associated with geosynthetics (filtration, drainage, separation, etc., Figure 25).

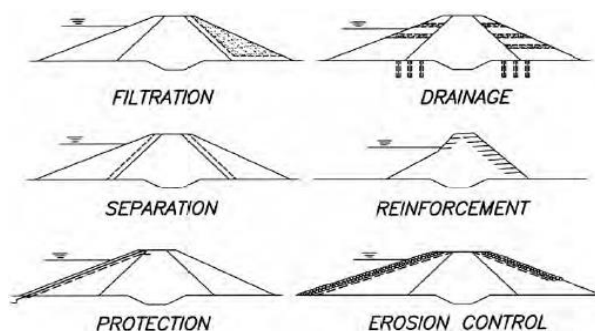


Figure 25. Functions of the geosynthetics in earthen embankments (FEMA, 2008).

Surface protection systems with geosynthetic components are being increasingly used in earthen dams, especially in spillways as a downstream slope protection and in overtopping protection of smaller earthen dikes/embankments (FEMA, 2008). Erosion control is assured by the capability of strengthening systems to provide stabilization of the adjacent surface soil (soil particle migration and mass movement are prevented) by having the shear stress dissipated before it reaches the soil surface (FEMA, 2008). The erosion of the soil surface will be controlled when the shear stress at the soil surface is less than the permissible shear for the soil surface, for a particular overflow duration (Kilgore and Cotton, 2005). Next, two common strengthening system are introduced.

Turf reinforcement mats

When grassed surface covers are not sufficient to resist erosive forces imposed by overflowing water, turf reinforcement should be considered as good solution for improving vegetation's resistance to erosion. Turf reinforcement integrates soil, lining material (TRM) and grass/stem roots within a single matrix (Kilgore and Cotton, 2005). Turf reinforcement mats (TRMs) are a specific type of product of a broader group of products know as rolled erosion control products (RECPs). RECPs are composed of four basic types of products, including mulch-control nets (MCNs), open-weave textiles

(OWTs), erosion-control blankets (ECBs) and turf reinforcement mats (TRMs). MCNs, OWTs and ECBs are temporary degradable RECPs and may be used in applications where natural vegetation alone (grass cover protection) will provide sufficient permanent erosion protection (Lancaster and Theisen, 2003). According to Erosion Control Technology Council, TRMs are described as (Lancaster and Theisen, 2003): “*A rolled erosion control product composed of non-degradable synthetic fibbers, filaments, nets, wire mesh and/or other elements, processed into a permanent, three-dimensional matrix of sufficient thickness. TRMs, which may be supplemented with degradable components, are designed to impart immediate erosion protection, enhance vegetation establishment and provide long-term functionality by permanently reinforcing vegetation during and after maturation*”. Turf reinforcement uses a three dimensional ultraviolet-stabilized mattress to provide additional resistance to soil movement. As vegetation is established, the roots wrap themselves in the synthetic undirected netting and lock themselves into place, thereby reinforcing the vegetative root structure and providing greater stability of surface top soil against erosive forces (Figure 26) (Haselsteiner *et al.*, 2008).



Figure 26. Vegetated high performance TRM system. Soil reinforcement is provided by the interlocking between the roots and mat (Hulitt, 2010).

A reinforced root structure precludes the detachment of the mat from the underlying soil, by decreasing significantly the formation of under currents in soil/mat interface (Kilgore and Cotton, 2005). The establishment of vegetation is also enhanced by ability of the matting’s fibber matrices to increase seed germination and plant growth by retaining moisture and regulating temperature at the soil (Nelsen, 2005).

Prior to the advent of TRMs, vegetative protection covers (or vegetative linings) were simply not considered for certain highly erosive conditions where expected velocities would exceed 2.1 m/s or shear stresses topping 177 Pa (Nelsen, 2005). However, industry has continued to improve research in TRMs and providing even more sophisticated products such as high performance turf reinforcement mattresses (HPTRMs).

High performance turf reinforcement mattresses

High performance turf reinforcement mattresses (HPTRMs) are the most advanced soft armouring protection system available today for severe erosion control challenges. This system has proven the ability to considerably increase the erosion resistance of vegetation, allowing their use in areas under attack of high flow velocities and shear stresses (that exceed a lot the resistance limits of mature natural vegetation alone). At Colorado State University Laboratory intensive research has been carried out over the past 10 years on this matter with enlightening results. HPTRMs working in conjunction with vegetation allowed to increase the instantaneous peak hydraulic resistance threshold of vegetation, in terms of flow velocity, by up to 6.1 m/s, and in terms of shear stress, by up to 670 N/m² (Miller *et al.*, 2012). Typically from full-scale overflowing testing using TRM/HPTRMs a variety of ranges of velocity, shear stress and Manning's roughness coefficient can be recorded, for both vegetated and unvegetated conditions as shown in Table 6.

Table 6. Ranges of hydraulic parameters typically attained during full-scale experiments (Thornton and Beasley, 2013).

| Soil condition | Velocity m/s | | Shear stress Pa | | Manning's <i>n</i> s/m ^{1/3} | |
|----------------|-----------------|-----|--------------------|-------|--|-------|
| | Min | Max | Min | Max | Min | Max |
| Unvegetated | 1,5 | 4,6 | 47,9 | 239,4 | 0,020 | 0,035 |
| Vegetated | 4,6 | 9,1 | 478,9 | 957,6 | 0,022 | 0,045 |

It is important to emphasize that a HPTRM is a TRM which exhibits a significantly greater ultimate tensile strength (in the order of 10 times the traditional TRMs) and higher resistance to ultraviolet light and also provides superior interlock and reinforcement capacity of top soil and root system. HPTRMs are generally thicker and denser than first generation (medium grade TRMs). The density and thickness of HPTRM is such that it

offers the additional protection of a physical barrier between the underlying soil and flowing water leading to increased erosive resistance and longer design life (CIRIA *et al.*, 2013). HPTRMs working in conjunction with specialized tie-down anchors (earth percussion anchors) create a refined protection system for erosion control and slope stabilization, named anchored reinforced vegetation system (ARVS). An ARVS should be considered for long or steep slopes, highly unstable channel and/or canal banks, and any time that greater factors of safety are needed. Geotechnical slope stability analysis must be performed as part of the design process of a solution where an ARVS is considered (Miller *et al.*, 2012). In a variety of applications, reinforced vegetative covers (TRMs and HPTRMs) can present itself as cost-effective and lightweight solutions for slope erosion control by providing immediate erosion protection and bridging the gap between vegetation installation and full establishment. It is also important to point up their applicability for various environment conditions: temperate, semi-arid and arid (Miller *et al.*, 2012). Accordingly, it can be used in lieu of some traditional hard armouring solutions such as rock rip-rap, concrete articulated block or gabions. Note that TRMs and HPTRMs only achieve their peak performance potential in conjunction with well established vegetation (once vegetated, it reduces flow velocities and thereby increases infiltration and reduces discharge) (Nelsen, 2005).

Application of the HPTRMs for design of the New Orleans dikes

After the devastation caused by Hurricane Katrina in 2005, the US Army Corps of Engineers was consulted for improving New Orleans dike system in terms of its resiliency against overtopping. This was accomplished through installation of landside slope armouring protection in locations where standard grass cover would provide insufficient resistance to erosion due wave overtopping and surge overflow. After a study that established a methodology to assess dike armouring necessities, a threshold overtopping rate of 92 l/s/m as defined as the criteria for installing landside slope protection systems (Flikweert *et al.*, 2013). Accordingly, HPTRMs have been applied over significant lengths of the new dikes in the New Orleans area to improve resilience during overtopping events as shown in Figure 27. Note that the established dike design criteria for New Orleans Hurricane Protection System included design shear stresses of 720 Pa and design velocities of 6.0 m/s over a 1V:3H landside slope composed of clay, for a storm duration ranging between 2 and 6 hours (Amini and Li, 2012).



Figure 27. Installation of HPTRMs on a New Orleans dike (Flikweert *et al.*, 2013).

2.7. Performance of surface protection covers under surge-overflow

As stated before, a way to mitigate external erosion is improving the dike crest/slope surface protection layer, which in turn can provide increased resiliency against overtopping. Therefore it becomes pertinent to clarify resiliency in the context of dike performance under hydrodynamic loading.

Earthen dike resiliency

According to Hughes (2011) resiliency is defined as: “*the capability of an earthen dike to continue to fulfil its function when subjected to hydrodynamic loading greater than that of the design level, without failure. It was also noted that dike damage may occur but it should not undermine dike’s functionality and should be repairable*”.

In order to provide appropriate earthen dike resiliency it is necessary to evaluate the capability of the cover layer (typically grass cover) to protect the dike during a wave/surge overtopping event; to determine the location within the dike system where additional protection beyond grass is necessary; and to choose a protective system suitable for the intended dike resiliency. Hughes (2011) presented a methodology for evaluating the strength and resiliency of an earthen dike protection system against wave overtopping induced by severe hurricanes. The methodology is based on the work of Dean *et al.* (2010) that establishes a connection between observed performance of grass-covered slopes during steady overflow and predicted performance during unsteady and intermittent wave overtopping, through the application of the concept of dike erosion equivalence.

Hughes’s methodology is beyond the scope of this dissertation but the hydraulic parameters behind its formulation do not, because they are related to steady overflow conditions. The Dean *et al.* (2010) approach is based on analysis of the Hewlett *et al.* (1987) results for steady flow overtopping and it is described below.

Steady overflow limiting velocity curves of Hewlett et al. (1987)

The main guidance available for performance of grass cover dikes under overflow conditions is a design chart drew by Hewlett *et al.* (1987) (*in* Hughes, 2011) and presented in CIRIA during the 1970/1980s, as shown Figure 28 and Figure 29. This chart used full-scale steady overflow testing data to develop stability curves for various grass qualities and other slope protection materials (TRMs, concrete block systems, etc.). Each design curve defines an acceptable level of erosion for slope protection surfaces (without putting the dike at risk of failure) by correlating limiting steady overflow velocity with overflow duration (Hughes, 2011). Therefore, at some point damage of the cover layer will occur, for example when the grass cover has lost so many grass that bare soil (typically clay) is exposed. Moreover, these stability curves recognized that erosion is time dependent process which means that a dike can withstand various overtopping discharges magnitudes for different durations (Dean *et al.*, 2010).

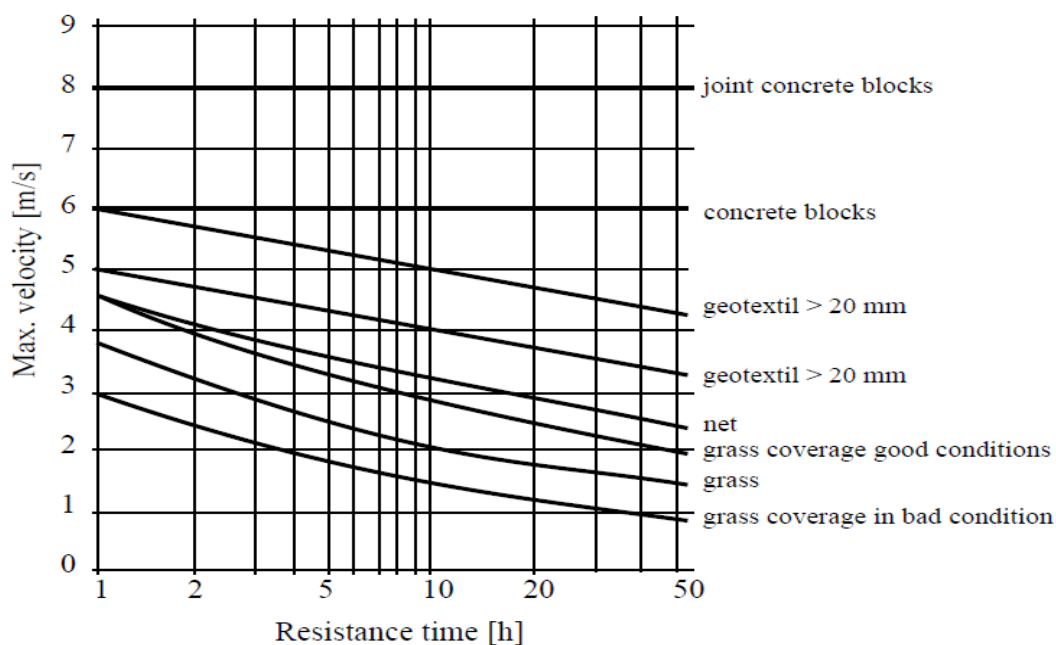


Figure 28. Limiting velocity versus duration curves created by Hewlett *et al.* (1987), for stability of slope protection surfaces subject to steady overflow (*in* Landa, 2014).

Hewlett *et al.* (1987) (*in* Hughes, 2011) drew curves for good-cover plain grass (in Figure 28 shown as grass coverage good conditions), average-cover plain grass (in Figure 28 figure shown as grass) and poor-cover plain grass (in Figure 28 shown as grass coverage in bad condition). The following description related to grass qualities was given: “*good grass cover is assumed to be a dense, tightly-knit turf established for at least two growing seasons; poor grass cover consists of uneven tussocky grass growth with bare ground exposed or a significant proportion of non-grass weed species; newly sown grass is likely to have poor cover for much of the first season*”.

It can be seen in the graphic that grass covers withstand faster (steady) velocities for only short durations, while slower velocities can be tolerated for longer durations. For example, according to Figure 28 grass coverage in bad condition can withstand 3 times the velocity at 1 hour as at 50 hour flow. This is why the duration of a discharge hydrograph, representative of flood event, is important for the stability of the dike cover protection. The Hewlett *et al.* curves derive from earlier work by Whitehead *et al.* (1976). Figure 29 contains the data points on which the Whitehead *et al.* curves are based on and the curves it selves, alongside with the three grass curves presented by Hewlett *et al.* (shown by heavy coloured lines) for comparison purposes.

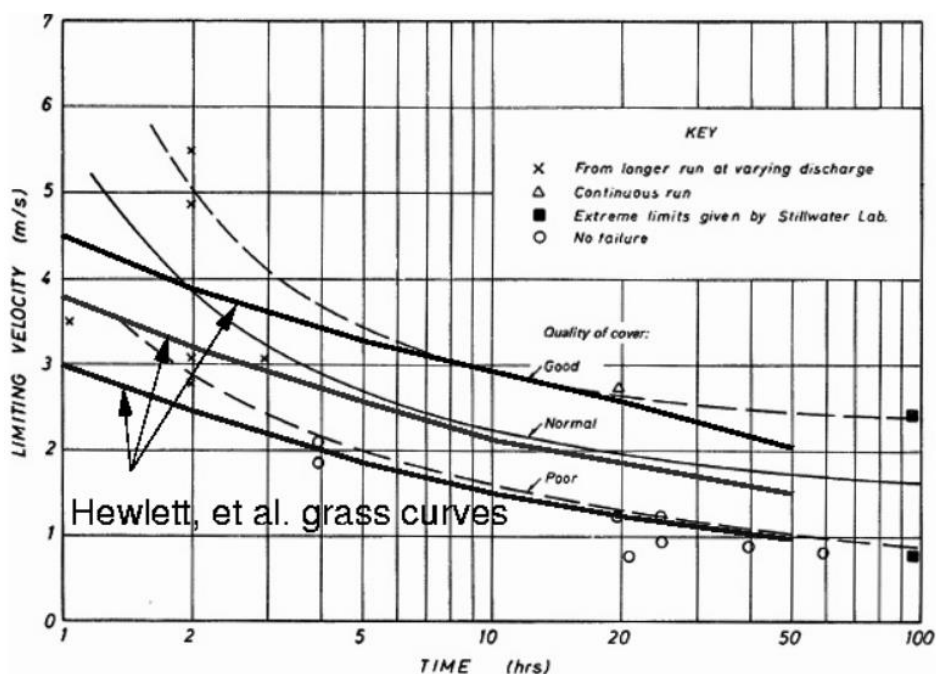


Figure 29. Comparison between Hewlett *et al.* (1987) grass performance curves and the original field test data from Whitehead *et al.* (1976) (*in* Hughes, 2011).

The main difference between the two design curves seems to reside at the threshold velocity values for short durations. The Hewlett *et al.* curves for grass suffered downward adjustments for lower overflow durations (for durations smaller than four hours approximately) in comparison the initial Whitehead *et al.* curves, as consequence of what appears to be an application of a safety factor (CIRIA *et al.*, 2013).

Physical basis for erosion

Dean *et al.* (2010) used experimental data (steady state results, Table 7) extracted from the Hewlett *et al.* grass-cover curves to investigate the physical mechanism responsible for the shape of the performance curves. It was considered three possibilities to explain the shape of the curves: a) velocity u greater than a threshold velocity $u_{c,u}$; b) shear stress τ greater than a threshold shear stress τ_c ; c) flow work W (stream power per unit area) above threshold flow work W_c .

Table 7. Hewlett *et al.* experimental values: combination of velocity and overflow duration for three qualities of grass cover (Dean *et al.*, 2010).

| Velocity (m/s) | Duration (h) | | |
|----------------|------------------------|---------------------------|------------------------|
| | Plain Grass-Good Cover | Plain Grass-Average Cover | Plain Grass-Poor Cover |
| 4.5 | 1 | NA | NA |
| 4.0 | 1.8 | NA | NA |
| 3.5 | 4 | 1.5 | NA |
| 3.0 | 8.5 | 2.5 | 1 |
| 2.5 | 20 | 5 | 1.9 |
| 2.0 | 50 | 14 | 3.8 |
| 1.5 | NA | 50 | 10 |
| 1.0 | NA | NA | 40 |

Each mechanism is characterized by an erosional index: velocity index (a); shear stress index (b); and work index (c). These erosional indices are based on acceptable erosion limits (E_u , E_τ and E_w (unknown coefficients)) above a particular threshold velocity due to an (Hughes, 2011):

- (a) excess of velocity (for $u > u_{c,u}$)

$$E_u = K_u t (u - u_{c,u}) \tag{38}$$

- (b) excess of shear stress (for $u > u_{c,\tau}$)

$$E_{\tau} = K_{\tau} t (\tau - \tau_c) = K_{\tau} \alpha_{\tau} t (u^2 - u_{c,\tau}^2) \quad (39)$$

(c) excess of work (for $u > u_{c,W}$)

$$E_w = K_w t (W - W_c) = K_w \beta_w t (u^3 - u_{c,W}^3) \quad (40)$$

where:

- E_u - erosion rate proportional to excess velocity [$\text{m}^3/\text{s}/\text{m}$],
- E_{τ} - erosion rate proportional to excess shear stress [$\text{m}^3/\text{s}/\text{m}$],
- E_w - erosion rate proportional to excess work [$\text{m}^3/\text{s}/\text{m}$],
- K_u - unknown coefficient proportional to excess velocity [m/s],
- K_{τ} - unknown coefficient proportional to excess shear stress [$\text{m}^2 \cdot \text{s}/\text{kg}$],
- K_w - unknown coefficient proportional to excess work [m^3/kg],
- α_{τ}, β_w - grouping of terms [kg/m^3],
- t - duration of the overtopping event (Table 7) [s],
- u - measured overflowing velocity (Table 7) [m/s],
- $u_{c,u}$ - critical value of velocity below which no erosion occurs [m/s],
- $u_{c,\tau}$ - critical value of velocity associated with shear stress threshold below which no erosion occurs [m/s],
- $u_{c,W}$ - critical value of velocity associated with the flow work threshold below which no erosion occurs [m/s].

Hughes (2011) derived the forms of α_{τ} and β_w and concluded that both equations are equal:

$$\alpha_{\tau} = \beta_w = \frac{1}{8} \rho_w f_D \quad (41)$$

where:

f_D - Weisbach-Darcy friction factor.

Dean's approach consists in a best-fit analysis between Hewlett's curves data and the equations (38), (39) and (40) to search for the best correlation. Accordingly, in order to obtain a minimum error of the curve fit, suitable values for erosional indices [E_u/K_u ; $E_{\tau}/(K_{\tau}\alpha_{\tau})$; $E_w/(K_w\beta_w)$] and threshold velocity values ($u_{c,u}$; $u_{c,\tau}$; $u_{c,W}$) were calculated.

Best-fit analyses - grass cover curves

The study undertaken by Dean *et al.* (2010) has revealed that the excess flow work index (represented by equation (40)) provided a substantially better fit (proven by the smallest standard error in velocities) than the others indices, despite the remaining indices had provided equally good fits. The work index developed by Dean *et al.* (2010) represents the summation of the product of work above the threshold and time. The results obtained for the best-fit of equation (40) to the Hewlett *et al.* grass curves are presented in Table 8.

Table 8. Threshold velocities, erosion limits, and velocity errors related to excess work index for the three grass qualities (adapted from Dean *et al.*, 2010).

| Plain Grass | Threshold velocity ($u_{c,w}$) m/s | Erosion limit ($E_w/K_w\beta_w$) m^3/s^2 | Standard error in velocity m/s |
|---------------|--|--|-----------------------------------|
| Good cover | 1.80 | 0.492×10^6 | 0.38 |
| Average cover | 1.30 | 0.229×10^6 | 0.12 |
| Poor cover | 0.76 | 0.103×10^6 | 0.04 |

In summary, this best-fit analysis of equations (38), (39) and (40) has led Dean *et al.* to conclude that cumulative work done on the landside slope by the flowing water, in excess of some critical value of work ($u > u_{c,w}$), was the physical mechanisms behind the shape exhibited by Hewlett *et al.* curves (limiting velocity versus duration) (Hughes, 2011). Figure 30 shows a comparison between predicted velocity curves of the best-fit associated with the flow work index and Hewlett *et al.* measured velocity curves for the three grass qualities. The heavy solid lines are the Hewlett *et al.* curves, and the symbols connected by lighter dashed lines are the best-fit values.

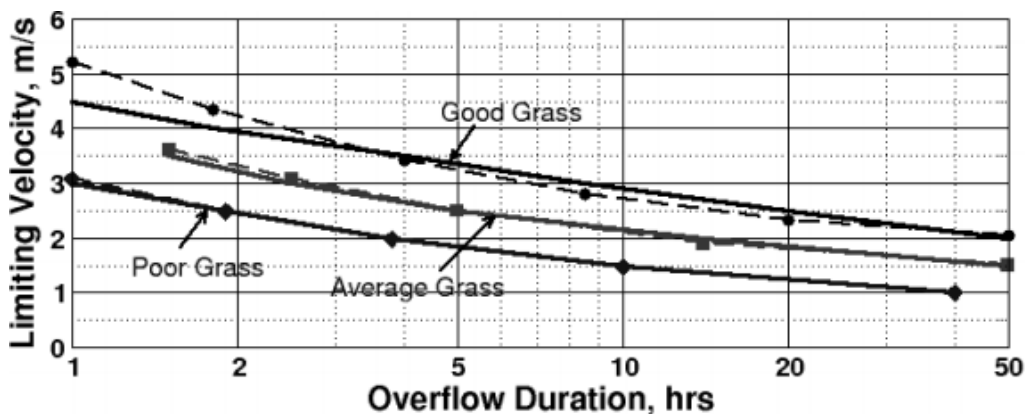


Figure 30. Best fit of equation (40) with Hewlett *et al.* (1987) grass curves made by Dean *et al.* (2010) (in Hughes, 2011).

It can be noted the very good fits obtained for average and poor grass qualities using the flow work index. The graphic shows that the standard deviation between predicted and measured velocities (using the best fit of equation (40)) is bigger at the short overflow durations for good grass. These over-predicted limiting velocities should not compromise the safety of the protective cover because Hewlett *et al.* curves have lower velocities at short-durations when compared to the original performance curves drew by Whitehead. A schematic representation of the Dean *et al.* conclusion is illustrated in Figure 31 for the Hewlett *et al.* curve corresponding to good grass cover condition.

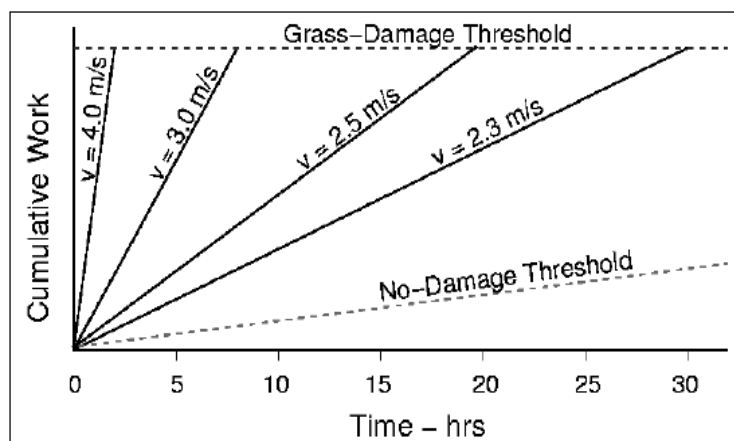


Figure 31. Schematic representation of the cumulative work excess work concept presented by Dean *et al.* (2010) (in Hughes, 2011).

Figure 31 intend to demonstrate that a steady overflow of a given velocity will produce a certain cumulative work over the dike landside slope, without causing severe damage to the grass surface, for a particular duration after the initiation of erosion threshold has been

overcame. This cumulative flow work defines an amount of acceptable slope erosion (function of flow velocity and overflow duration) that occurs between the no-damage threshold and the grass-damage threshold. For example, a grass cover able to withstand a certain level of steady overflow for four hours might suffer damage after an additional period of two hours at the same level of overflowing intensity. Due to the steadiness character of the overflow the velocity lines are linear representing the constant rate of accumulation of flow work over the landside slope. Note that in case of a storm event this simplification cannot be applied because the rate of overtopping varies with surge and storm intensity (Hughes, 2011). According to Hughes (2011), Dean *et al.* excess flow work model gives a warning when isolated grass cover damage starts to become locally problematic.

Best-fit analyses – open and filled mat curves

Hughes (2011) performed an analysis similar to Dean *et al.* (2010) approach for other slope protection surfaces, such as TRMs. Hewlett *et al.* design curves include limiting velocities values for concrete block systems, open mats and filled mats, apart from the various types of grass cover. Open mats were described by Hewlett *et al.* (1987) (*in* Hughes *et al.*, 2011) as synthetic mats which are subsequently filled with top soil and he recommended a nominal minimum mat thickness of 20 mm with the mat installed near the soil surface. Filled mats were defined as synthetic mats filled with bitumen-bound gravel and these mats should be at least 20 mm thick. Fabrics are basically woven geotextiles and they should be installed within 20 mm of the soil surface.

After analysing full-scale tests for a variety of mat products Hewlett *et al.* suggested that the risk of mat uplift may attain critical levels when average flow velocity is greater than about 5 to 6 m/s. So, these values constitute the thresholds velocities beyond which uplift may occur (5 m/s to filled mats and 6 m/s to open mats) and that were used in Hewlett's design curves for geotextiles with a minimum opening size of 0.5 mm (Hughes, 2011).

Hughes best-fit analysis (through a MatLab[®] script) for the open and filled mat curves using excess work index (equation (40)) provided the following erosional indices and thresholds velocities (Table 9).

Table 9. Threshold velocities, erosion limits, and velocity errors related to excess work index for the Hewlett *et al.* (1987) mat curves (adapted from Hughes, 2011).

| Mat type | Threshold velocity ($u_{c,w}$) m/s | Erosion limit ($E_w/K_w\beta_w$) m^3/s^2 | Standard error in velocity m/s |
|------------|---|---|-----------------------------------|
| Open mat | 4.23 | 1.231×10^6 | 0.66 |
| Filled Mat | 3.32 | 0.730×10^6 | 0.53 |

It can be noted that threshold velocities and erosion limits for the two mat types are higher than the values obtained for grass-cover surfaces, as it was expected. These parameters were substituted into equation (40) to estimate velocity as a function of duration for both types of mats. Equation (40) can be rewritten in the following expression:

$$u_{w,p,i} = \left(\frac{E_w}{K_w \beta_w t_i} + u_{c,w}^3 \right)^{1/3} \tag{42}$$

where:

$u_{w,p,i}$ - predicted velocity for each data point [m/s],

$E_w/K_w\beta_w$ - erosional limit: work index [m^3/s^2].

Figure 32 picture compares predicted velocities curves calculated by Hughes (2011) and the ones measured by Hewlett *et al.* (1987). The points connected by dashed lines are predicted limiting velocities and the heavy lines are the original data from Hewlett *et al.*

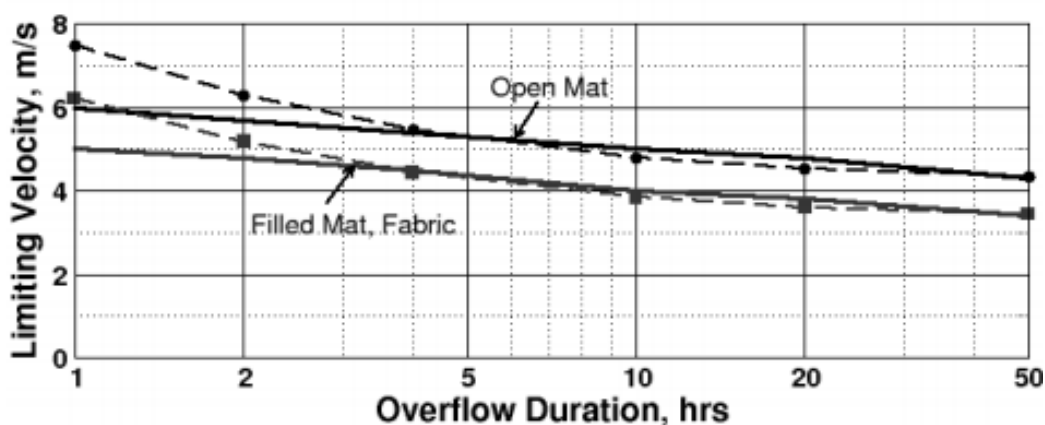


Figure 32. Best fit of equation (40) with Hewlett *et al.* (1987) performance curves related to open and filled mats (Hughes, 2011).

Likewise Dean *et al.* results, where greater deviations between predicted and measured velocities for grass slopes can be noticed at the short-duration side of the graphic, the analysis done by Hughes seems to follow the same trend. In general, the Hughes curves do not overlap so well the original design curves because of their straightness nature that contrasts with the curvature exhibit by limiting grass lines. Hughes (2011) has stated that the thresholds velocities and erosional indices related with the open and filled mats should be considered less reliable than those for grass-covers. This inference is based on amount of available data, which he considers to be scanty, and also in straightness nature of the lines, which he considers to be questionable.

2.8.Full-scale overtopping tests

The erosion process of an earthen dike may be difficult to model numerically or in small-scale physical models, therefore it is advised that the effectiveness of strengthening systems should be determined by full-scale testing in laboratory flumes using defined testing protocols (Hughes, 2008).

Small-scale effects

Small-scale hydrodynamic laboratory experiments raise concerns about scale effects that might have influence on physical model results and lead to inaccurate representation of real-world waterflow and dike soil erosion behaviour (Hughes, 2008).

According to Hughes and Shaw 2011) (*in Hughes et al.*, 2012) potential scale effects may be concerned to: surface friction, air entrainment and erosion behaviour of soil.

It is difficult to scale the surface roughness of dike grass-covered slopes reinforced or not with a strengthening system and consequently the friction forces inherent to passage of flow.

It also difficult to produce and simulate air entrainment during small-scale experiments. At full-scale conditions a high percentage of air entrainment in the flow might cause reduction of maximum flow velocity (by increasing flow thickness) while in small-scale physical models a similar reduction would not happen.

At last, is not possible to model at small-scale the erosion behaviour of a soil under a protection cover, specially vegetated reinforced grass covers.

Accordingly, full-scale testing is ideal for extracting reliable data that can be applied in calibration of predictive numerical models. Consequently, numerical modelling simulations that more accurately reproduce the erosional resistance of dikes and the robustness of the various armouring alternatives, may be provided (Hughes, 2011).

2.8.1. Nelsen (2005) laboratory experiments

Nelsen (2005) conducted large-scale laboratory experiments at Colorado State University (CSU) to assess vegetation reinforcement capability of three turf reinforcement mattresses (SC205[®], C350[®] and P550[®]), when exposed to a surge-only overflow loading, in terms of erosion control performance. Note that up to Nelsen research, turf reinforcing was only considered for situations where the critical shear stresses would not exceed 389 Pascal or even less, based on design values published in Federal Highway Administration (FHWA)'s Hydraulic Engineering circular #15 (2nd edition) (Chen and Cotton, 1988 *in* Nelsen, 2005).

Testing procedure and flume layout

The research procedures were based on American Society for Testing and Material (ASTM) standardized test method D6460, entitled *Standard Test Method for Determination of Erosion Control Blanket (ECB) Performance in Protecting Earthen Channels from Stormwater-Induced Erosion*, and the TRM products were tested for the three life stages of a reinforced vegetated protection system (flexible channel lining): 1) unvegetated; 2) partially vegetated (establishment phase); 3) fully vegetated.

The flume bottom layer was made up of a highly erodible sandy loam soil (USDA classification system) where overlying TRMs were installed. The bottom layer was placed into a 1.2 m wide by 12.2 m long test flume. The reinforced armouring systems were subjected to one-hour (short duration) and ten-hour water discharges (long duration) generating increasing levels of hydraulic shear stress, for a certain channel gradient (that also varied). The main goal was to estimate the magnitude of flow-induced shear stress (which is considered the hydraulic pulling force on the matting and/or soil) at which excessive erosion will occur – permissible/limiting shear stress.

Excessive erosion criteria

Excessive erosion is defined as removal of an average of 12.7 millimetres of soil from beneath the mat and/or through the mat-reinforced vegetation. ASTM D6460 establishes standards and methodology to convert soil loss measurements from beneath the nettings into an average Clopper Soil Loss Index (CSLI).

Immediately prior to testing, the initial soil surface elevation readings were made at numerous pre-determined locations. The channel was then exposed to sequential discharges during where flow thickness and corresponding velocity measurements were taken at the same predetermined cross-section locations (Figure 33). Soil loss measurements were made between overflowing events (typically one-hour flow events), stopping the discharge and recording the soil surface elevation values using a point gauge instrument. As long as soil loss was less than 12.7 mm and the waterflow did not provoke physical damage or excessive fiber loss, the testing program would proceed to the next discharge level. Additionally, stem and leaf density counts were conducted before the waterflow discharge started and after each flow passage, as a means to verify vegetation reinforcement capability.



Figure 33. Flow velocity measurement (on the left picture) and flow depth measurement (on the right picture) in the testing channel (Nelsen, 2005).

Results

Phase 1: In unvegetated testing, the TRMs were exposed to steady overflows that created surface shear stresses ranging from 24 Pa up to 454 Pa. The soil loss for each tested product was less than 12.7mm at the following unvegetated permissible shear stress values: 144 Pa for RECP SC250[®]; 153 Pa for RECP C350[®]; and 191 Pa for RECP P550[®].

Without any surface protection (bare soil) soil loss threshold was reached at a shear stress of only 2.9 Pa. Note that the mats were able to resist to a 454 Pa shear stress maintaining their integrity despite did not complying with the excessive erosion criteria.

Phase 2: In partially vegetated TRM tests, the mats were installed over a highly erodible sandy loam soil seeded with *Kentucky Bluegrass* (retardance class C) (non-organic fibbers were installed to simulate worst case conditions). After one year of grass growing (growing up through 3D matting structure), the testing tray was placed into the flume and tested at a 7% gradient. Table 10 summarizes the main hydraulic parameters recorded during the testing associated with the maximum permissible shear stress attained in the flume for a specific reinforced vegetative lining (Vmax P550[®]).

Table 10. Specific discharge, flow thickness, velocity and maximum permissible shear stress estimates for partially vegetated conditions.

| q l/s/m | h_w m | U m/s | τ_c N/m ² |
|--------------|------------|------------|------------------------------|
| 2833 | 0.46 | 6.1 | 574 |

These parameters refer to RECP Vmax P550[®] (Tensar[®]).

The other permissible shear stress values obtained were 383 Pa for the RECP SC250[®] and 480 Pa for the RECP C350[®]. Note that this permissible shear stress is the shear stress on the mat that results in 12.7 mm of average soil erosion. It is important to emphasize that even when exposed to this extremely erosive flow conditions, the reinforced protection cover experienced no soil loss, no damage to vegetative cover, and no physical damage to the matting itself. Note that FHWA (1988) recommends a maximum permissible shear stress of 48 Pa for a simple grass lining (Retardance Class “C”). This is an illustrative example how TRMs can greatly increase hydraulic resistance limits.

Phase 3: In order to achieve a fully vegetated condition grass cover was allowed to grow another season until the test trays reached a density of approximately 75-90% with a height of 15 cm. Extremely high shear stress flows were attained and maintained for consecutive

one-hour flow events in a 50 % gradient flume to determine the short-duration performance of the reinforced vegetative linings. The maximum induced shear stress reached in the testing flume (the one that maximizes the flume capability) and its associated hydraulic parameters are introduced in Table 11.

Table 11. Maximum flume capabilities in terms of: discharge, flow thickness, velocity and shear stress values related to reinforced fully vegetated lining.

| q l/s/m | h_w m | U m/s | τ_c N/m² |
|--------------------------|----------------------------------|------------------------|--|
| 2333 | 0.30 | 7.6 | 960 |

These parameters refer to RECP Vmax P550® (Tensar®).

This values established new matting performance values, proving the physical durability of the TRM and its ability to resist physical damage at extreme high shear stresses. New grass (fully-vegetated) performance threshold values for short overflow durations (less than two hours peak flow), in terms of shear stress, were discovered: 672 Pa for the RECP P550®; 576 Pa for the RECP C350® and 480 Pa for the RECP SC250®.

Long duration testing (more than two hours peak flow) generated the following permissible shear stress values for a 10 hour overflow event: 576 Pa for the RECP P550®; 480 Pa for the RECP C350® and 383 Pa for the RECP SC250®. Note that shear stress permissible values were diminished after the extension of overflow duration which makes particularly noteworthy the performance of the reinforce grass cover (no soil loss greater than 12.7 mm and no physical damage).

Importance of flow duration

It is important to highlight the negative influence of overflow duration in the performance of the reinforced vegetative covers in terms of erosion control. The continued exposure to high water flows causes soil saturation which may change the erosive properties of soil and respective grass cover, which becomes stressed or damaged (Nelsen, 2005). Therefore using permissible values of shear stress and velocity based on short duration testing may overestimate the field performance of a reinforced vegetated system, since its permissible shear stress is reduced by long-lasting overflows. A long duration flow event more closely represent field conditions and it can be evaluated through the representative flood event hydrograph. In a particular flood hydrograph it is not only instantaneous discharge

(Q_{peak} , Figure 34) that impacts stability of the reinforced protection cover but a flow rate over time. So, a reasonable interval of threshold flow rate over time (Figure 34) must be defined to include several hours or days (Miller *et al.*, 2012).

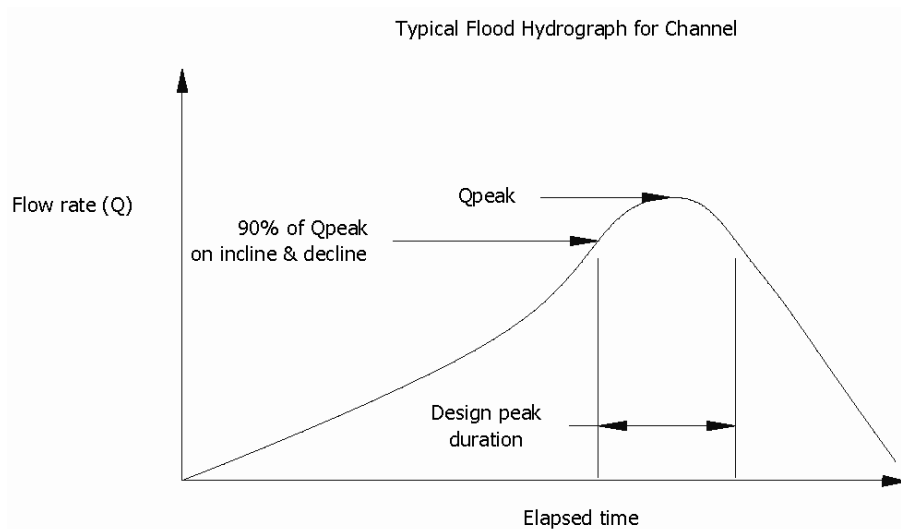


Figure 34. Example of flood hydrograph for a small basin showing Q_{peak} and duration of flow exceeding 90% of Q_{peak} (Miller *et al.*, 2012).

2.8.2. Haselsteineir *et al.* (2008) laboratory experiments

At the laboratory of the Technical University of Munich's Hydraulic Engineering (Germany) and Water Supply Research Institute a series of full-scale model tests were carried out (2006/2007) to evaluate the effectiveness of a surface protection system represented in Figure 35 under overflow conditions, in terms of erosion control performance (Haselsteiner *et al.*, 2008).

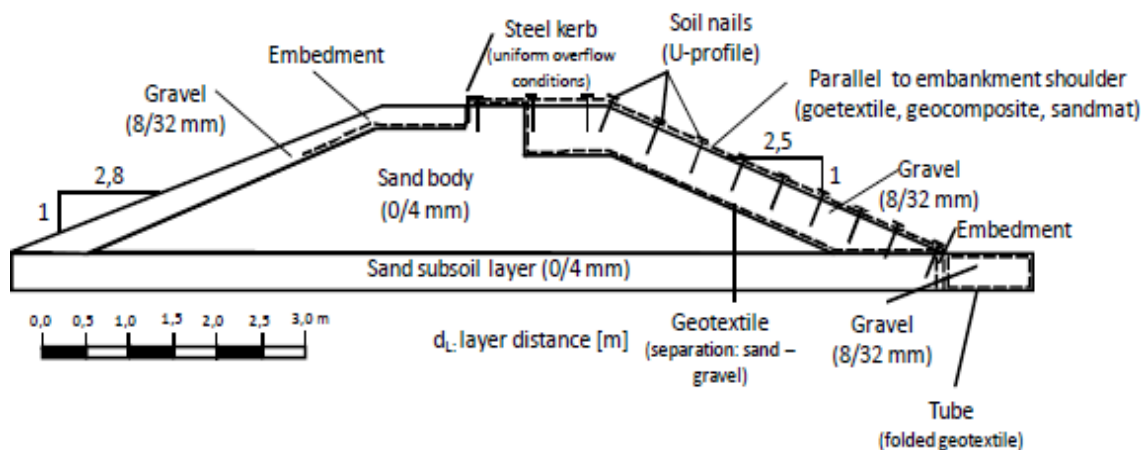


Figure 35. Overflow protection system using geogrid/nonwoven geotextile (a type of RECP) and ground pins/nails (Haselsteiner *et al.*, 2008).

The hydraulic model was located in a concrete channel 20 m long with U-profile discharge section of 2.5 m width and 2.5 m height. The experiments were carried out on downstream slope with an inclination angle varying from V:H=1:1.5 up to 1:2.5.

Figure 36 illustrates a slope-parallel protective system placed 20 cm beneath the topsoil layer of landside slope. Note top soil layer should include grass and may be eroded in case of overflow. The RECP is installed contiguously over the landside slope surface of the hydraulic model sand core and fixed in place with ground pins that function like anchors (Figure 36). It is also anchored at the waterside embankment slope in to be properly fixed. The protection of the slope toe area was guaranteed by the application of a tube at the toe where the geosynthetic is braced. Underneath the surface protection matting gravel was spread and compacted. The transition zone from sand body to coarse gravel layer was filtered by a geotextile filter. The presence of this geotextile and the coarse grained soil material are essential to preclude the harmful migration/transport of the fines. To provide homogeneous overflow conditions a steel kerb was placed on hydraulic model's crest.

The hydraulic model was loaded by specific discharge value (q) ranging from 50 l/s/m up to 300 l/s/m (Figure 36) what provoked overflow heights at the crest model ($/-R_c/$) of 0.10 to 0.35 m, respectively.



Figure 36. Overflowing experiments with a slope protection system with geosynthetics (Combigrid[®]). On the left: before overflow; on the right: in overflow state with $q_{max}=300$ l/s/m (Haselsteinaer *et al.*, 2008).

Testing results

It was observed that applying a composite product made of a geotextile and a geogrid (Combigrid[®]) and soil nails for stabilization, the system shown in the Figure 36 performed well, without remarkable damage or deformation when loaded by a specific discharge of 130 l/s/m. Minor deformation occurred only after the applied soil nails/anchors were subsequently removed. The initial anchor pattern was approximately 2.5 anchors per square meter (25 anchors were used to fix the mat to the model landside slope).

In summary this system can be used to enhance both resistance to external erosion and stability of a dike. Nevertheless, attention should be given to the anchor arrangement over the surface boundary of the slope (*i.e.*, appropriate anchor type, length and spacing) since this is a key aspect for ensuring the stability of surface protection system and erosion of underlying soil material. As the hydraulic forces on the downstream slope increase, the mat is detached from underlying soil, which allows a current to establish between the mat and soil surface. Consequently, turbulent fluctuations within this current eventually erode the soil surface (Kilgore and Cotton, 2005). One advantage of this kind of this system for practical use is the simple way of application. After the refurbishment of dikes, the geosynthetic mat can easily be placed on the finished landside slope. Afterwards the top

soil layer can be placed on the top of it. If the grass cover is lost, a reinforced overflow slope remains. So with only a slightly higher expenditure, a stronger protection system is achieved (Haselsteiner *et al.*, 2008).

2.8.3. Amini and Li (2012) laboratory experiments

A full-scale laboratory test of combined wave and surge overtopping of a trapezoidal dike cross-section was conducted in Large Wave Flume in the O.H. Hinsdale Wave Research Laboratory (HWRL) at Oregon State University (Amini and Li, 2012). The main goal of the experiments was to determine the effectiveness of a dike strengthening system, composed of a vegetated high performance turf reinforcement mat (HPTRM), during extreme overtopping conditions.

Model setup

The flume used for the experiments is 104 m long and it has a rectangular cross-section 3.66 m wide and 4.57 m high. The flume is equipped with a unidirectional piston wave maker and pump system capable to provide a $0.95 \text{ m}^3/\text{s}$ discharge with an upstream head of 0.305 m on the crest of the physical model build inside it (Figure 37). The trapezoidal dike cross-section is 26.14m long x 3.25 m high x 3.66 m wide, with a waterside slope of 1:4.25 (V:H) and a landside slope of 1:3 (V:H), as shown in Figure 37. It is constituted by a sand core covered with concrete cap where a 2.34 m wide metal tray containing the vegetated HPTRM system will be fixed on its landside slope and crest (Figure 38). The metal tray was designed and constructed for installation and growing of HPTRM system, creating a test section 2.57 long on the crest and 9.63 m long on the landside slope (Figure 38). A 5 cm drainage layer of gravel ($D=30 \text{ mm}$) was laid down over the base of the metal tray and 15 cm layer of sandy clay soil was compacted above it. Afterwards the geosynthetics mat was spread across the entire metal tray and anchored to the soil with wire U-shape staples fasteners. At last, seeding was done and for 6 months grass (warm-environment Bermuda grass) was allowed to grow with proper maintenance and a stringent quality control procedure (in order to avoid that grass would become dormant during the growing process, which compromises the root strength to hold the HPTRM).

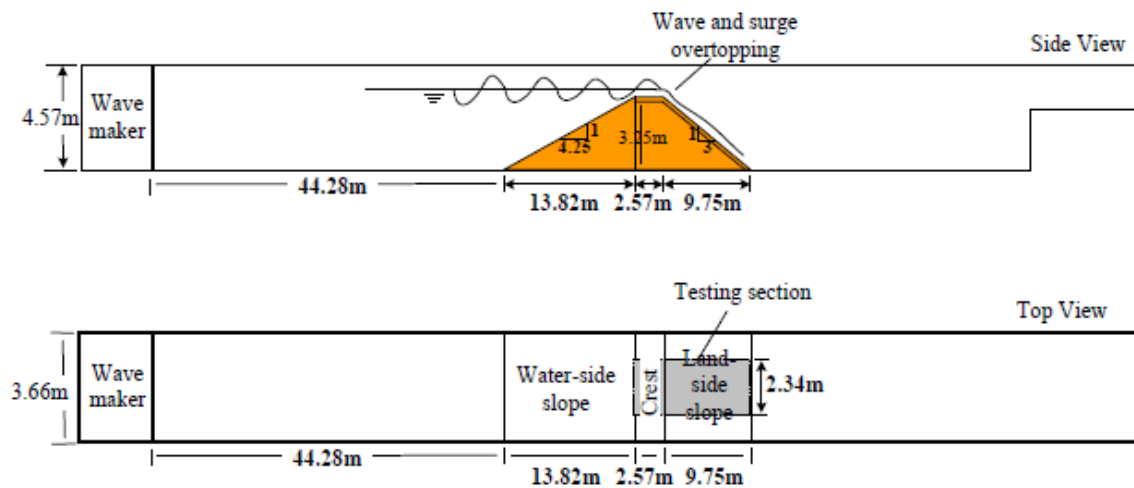


Figure 37. Sketch of the flume where the physical model is installed (top and side view) (Pan *et al.*, 2012).



Figure 38. Metal tray with vegetated HPTRM system being installed on the dike inside the flume (Amini and Li, 2012).

Instrumentation data collection

Instantaneous flow velocity parallel to the crest and landside slope was measured in various locations (4 locations) with two types of Acoustic Doppler velocimeters (ADV), a down-looking ADV and a side-looking ADV (Figure 39). Both ADVs are capable of measuring velocities up to 4 m/s. The down-looking ADV measures the velocity 5 cm

above the lying-down vegetation and side-looking ADV measure the velocity 2 cm it, so that velocities corresponding to small flow thickness can be measured (the probe needs to be submerged to obtain reliable velocity data). Instantaneous flow thickness was measured with acoustic range finders at the same ADVs cross-section locations of ADVs and in another location at the downward side of the slope (Figure 39).

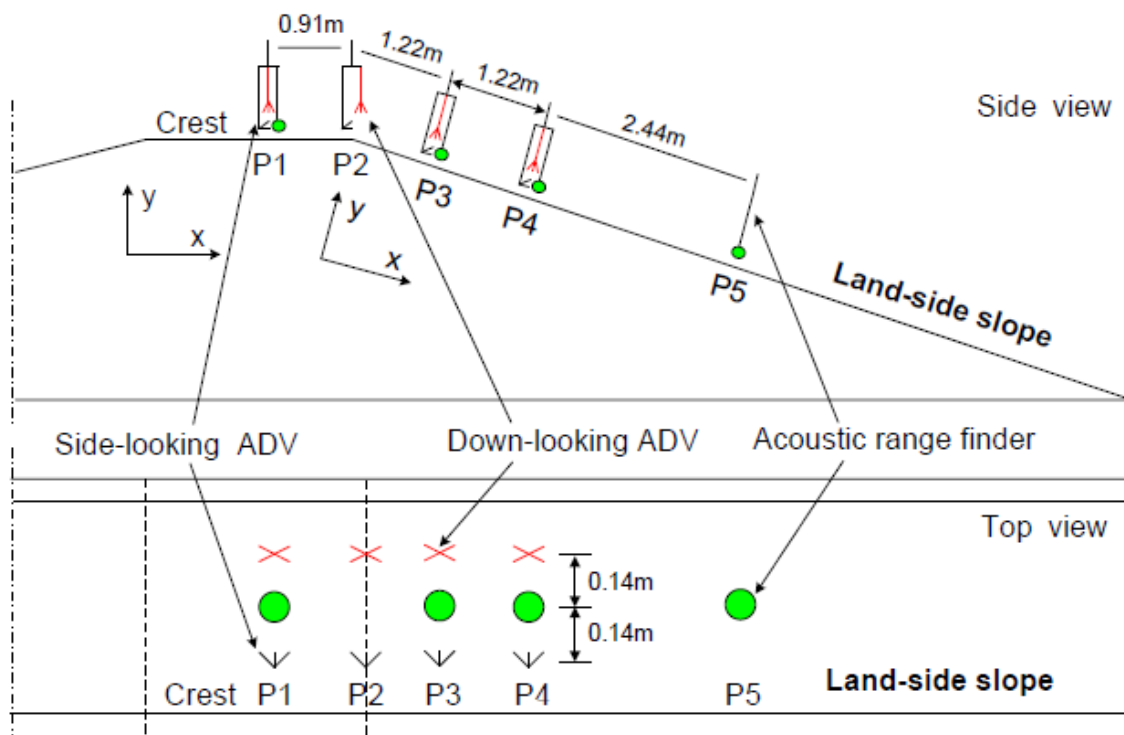


Figure 39. Location of ADVs and acoustic range finder at the crest and landside slope of the physical model (Pan *et al.*, 2012).

Discharge time series was estimated using the flow thickness and velocity values on the crest of the physical model ($q=h.U$). Figure 40 shows an example of the flow thickness, flow velocity, and calculated discharge time series at a dike crest location subjected to combined wave and surge overflow. The measured hydraulic parameters present a large variation comparing to an overflow situation.

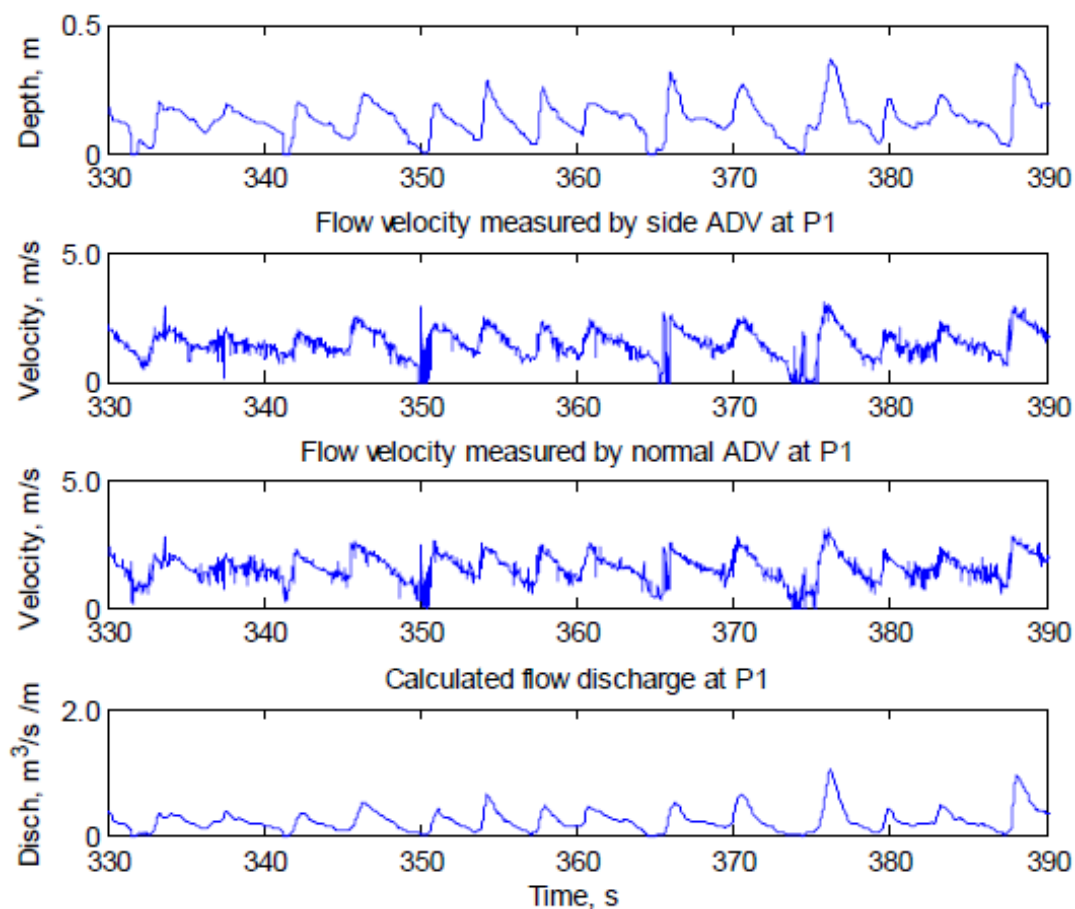


Figure 40. Measured flow thickness, measured flow velocity and calculated discharge time series representative of combined surge overflow and wave overtopping at a dike crest location (Hulitt, 2010).

The experimental study undertaken by Amini and Li (2012) provided some empirical design equations related with a HPTRM strengthening system tested under surge-only overflow conditions (the equation are only applicable to for the similar systems with the same characteristics of tested physical model).

Steady overflow discharge

The only steady overflow test was run for 60 minutes with specific discharge (q_s) of $0.251 \text{ m}^3/\text{s}/\text{m}$ and attaining an upstream head (equal to negative freeboard) of 0.296 m at the crest. The Manning coefficient was estimated to be $n=0.035$. An empirical coefficient, $C_f=0.415$, was also estimated and compared with the one used in Henderson's broad-crested weir discharge formula (1966), related to steady overflow. Accordingly, the following equation was obtained, representing the relationship between the specific discharge (q_s) and the negative freeboard ($-R_c$) (Figure 41).

$$q_s = C_f \sqrt{g} | -R_c |^{3/2} = 0.415 \sqrt{g} | -R_c |^{3/2} \quad (43)$$

However, the calculation of C_f and n might not be precise due to the lack of sufficient data points as show in Figure 41 (Amini and Li, 2012).

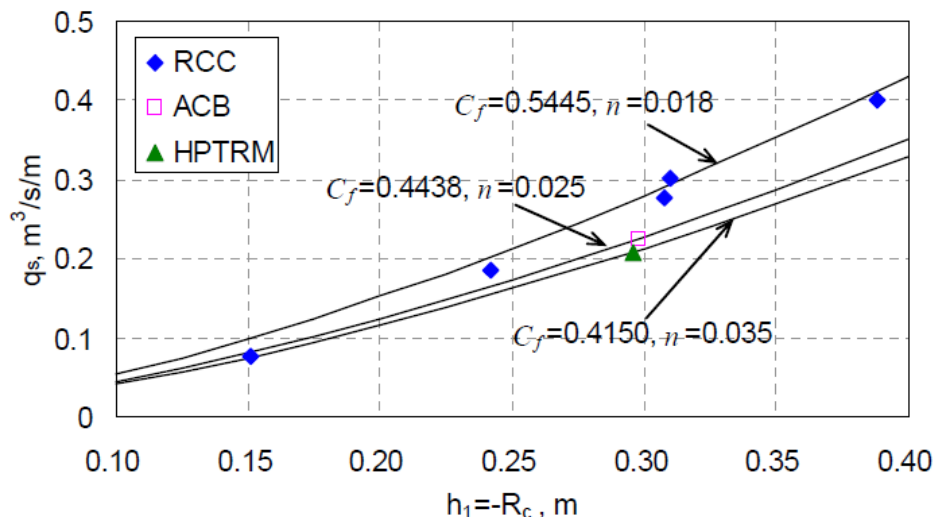


Figure 41. Steady overflow discharge (q_s) versus upstream head (h_1) (or negative freeboard ($-R_c$)) for 3 different strengthening systems (rolled compacted concrete protection system (RCC); articulated concrete block protection system (ACB); and high performance turf reinforcement system (HPTRM) (Amini and Li, 2012).

The empirical coefficient of equation (43), $C_f=0.415$, is smaller than the one calculated by Henderson (1966). An explanation for this discrepancy may be related with the fact that considerable frictional energy losses take place along the crest of a dike reinforced with vegetated HPTRM system. Henderson assumed that energy losses are minimal along the crest which increased the constant C_f (Li *et al.*, 2013).

Average flow thickness on landside slope

It was also establish a linear relationship between the average flow thickness (d_s) on the landside slope, represented by the overflow parameter $(gd_s^3)^{1/2}$, and the specific discharge (q_s). This relationship is represented by equation (44) and the empirical coefficient k_d represents the best-if of equation with the data collected (Figure 42).

$$q_s = \frac{1}{k_d} \sqrt{g} d_s^{3/2} = \frac{1}{0.3076} \sqrt{g} d_s^{3/2} \quad (44)$$

Once more the data collected was scarce to be considered reliable, as shown in Figure 42.

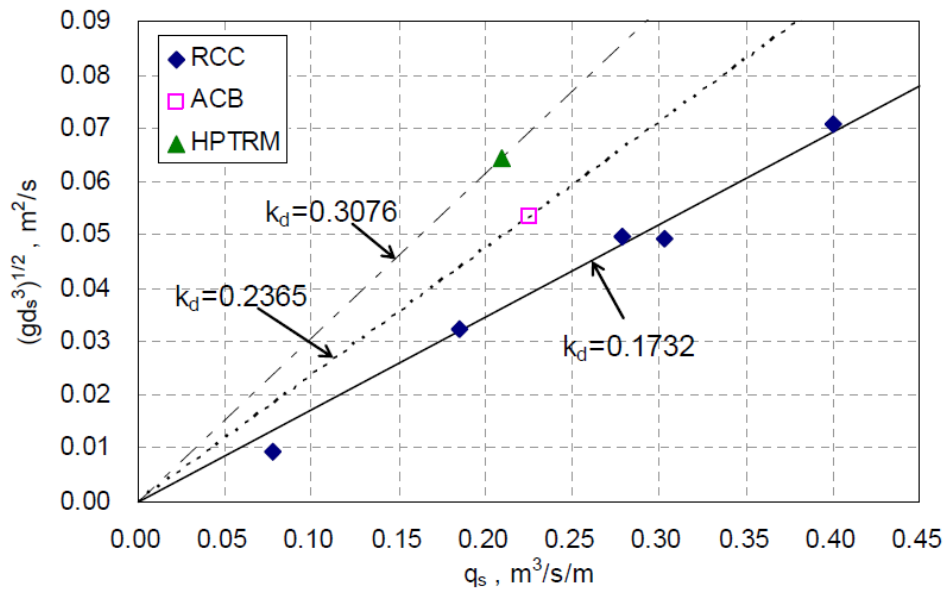


Figure 42. Steady flow thickness (d_s) on landside slope (represented by a hydraulic parameter) versus specific discharge (q_s) for three different strengthening systems (RCC, ACB and HPTRM) (Amini and Li, 2012).

Steady velocity on landside slope

Steady flow velocities (v_s) for surge-only overflow were calculated by dividing average overtopping discharges (q_s) by the measured average flow thicknesses on the most downward measurement location at the landside slope ($v_s = q_s/d_s$).

In order to estimate a flow velocity on landside slope in function of the upstream head (h_1) equation (45) was derived. This equation is based on the equations (43) and (44).

$$v_s = k_v \sqrt{g h_1^{3/2}} = \left(\frac{C_f}{k_d^2} \right)^{1/3} \sqrt{g h_1^{3/2}} = 1.637 \sqrt{g h_1^{3/2}} \quad (45)$$

Testing observations

Prior to wave overtopping tests, a 2 minute overflow test was done to lay-down the stems because the bending of stems increases the flow velocity and discharge and thereby reducing the difference between “apparent” discharge and actual discharge. The amount of water that flows through and filters down the grass could not be estimated in order to find out the actual discharge.

The flow velocity on HPTRM system was slower than the flow velocity on the two wooden board placed alongside the testing tray with less surface roughness which proved that reinforcement system can decrease the flow velocity (Figure 43). On the crest and

upper part of landside slope the flow was laminar and transparent and then started to become aerated and unsteady (1/4 distance of the slope length) (Figure 43). There was no visible grass-swept on the dike, but after each test, the water in the flume became obviously muddy (Amini and Li, 2012).

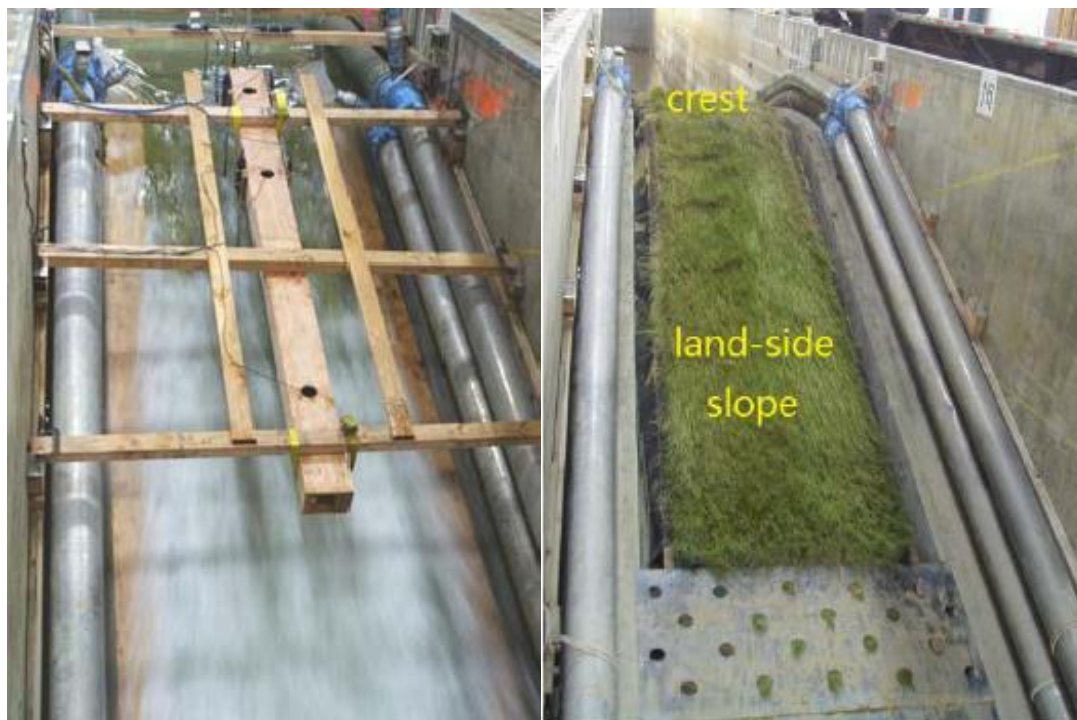


Figure 43. Surge-only overflow on the landside slope of the physical model with a vegetated HPTRM system installed on it (left side photograph). Reinforced grass system after the surge-only overflow experiment (right side photograph) (Hulitt, 2010).

Soil erosion

A variety a pre-defined locations were inspected for soil erosion (the vertical elevation of each location was measured with a long stick before and after each testing). For this experiment it was defined that critical damage is attained when soil and stem loss (>2.5 cm) is such that exposes the grass root system to erosion and hence causing instability of the HPTRM system. The maximum soil loss registered at the dike crest was 0.2 cm and at the landside slope was 0.9 cm, for the surge only overflow test.

As expected the soil loss is higher at landside slope in the most downward location because it is subjected to a supercritical flow velocity and more turbulent conditions (Figure 44). The maximum soil loss comply with excessive erosion criteria (section 2.8.1) and hence the system was considered stable under the testing overflow conditions (Hulitt, 2010).

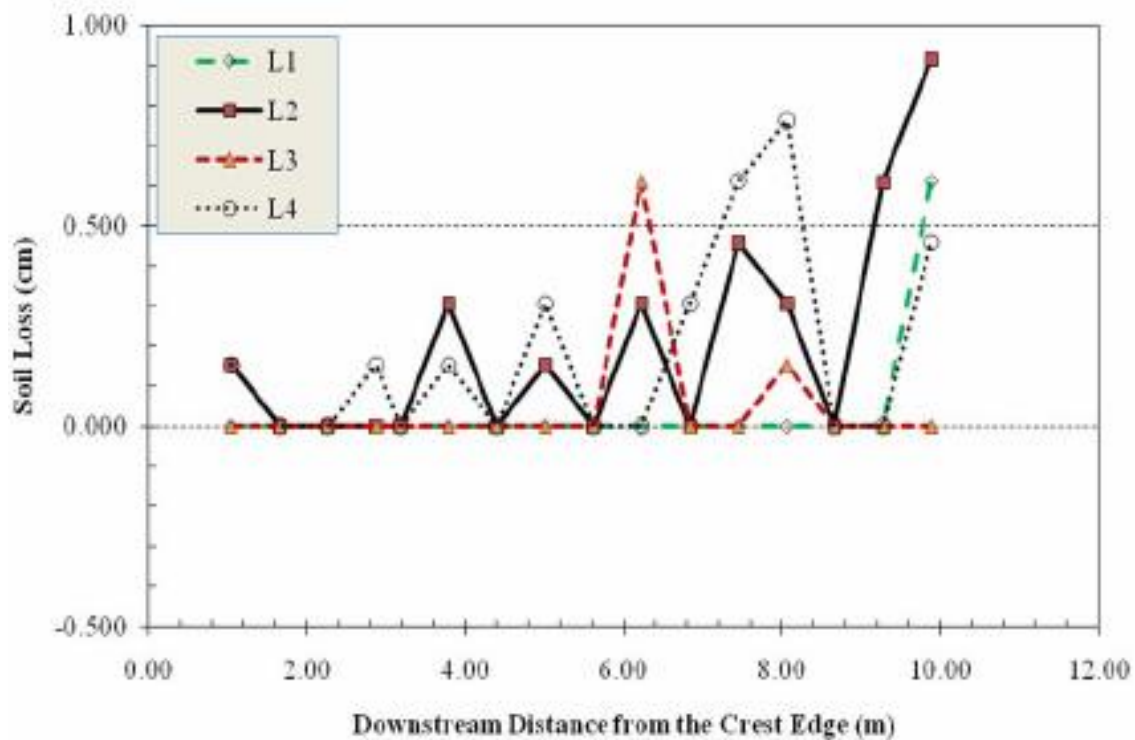


Figure 44. Soil loss measurements (cm) in the landside slope for a specific discharge $q_s=0.251 \text{ m}^3/\text{s}/\text{m}$ and overflow duration of 60 minutes (Hulitt, 2010).

3. EXPERIMENTAL STUDY

3.1. Physical model

The laboratory experiments were carried out on a hydraulic model (full-scale), assembled at the Hydraulic Engineering Laboratory of the Faculty of Civil Engineering of Zagreb (Croatia) consisting of a steepen wooden channel and a recirculation system (Figure 45). The tests were conducted for different surface granular materials and for different types of RECP (6, in total) installed over it. The structure pretended to simulate the surface layer of a dike landside slope which will convey the waterflow from an upstream area (reservoir) to a downstream area (flood expansion zone or polder area), during an overflow event caused by high water levels.

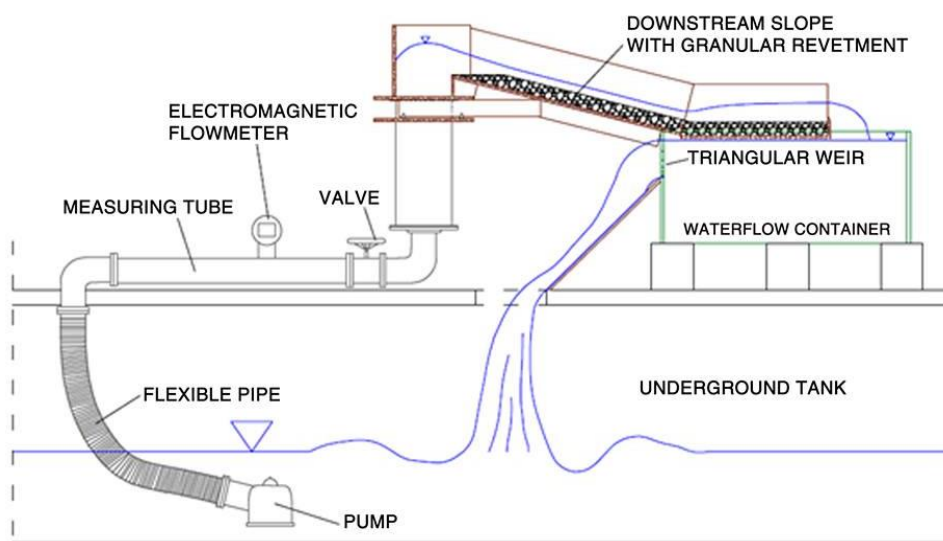


Figure 45. Schematic illustration of the overtopping hydraulic model.

3.1.1. Hydraulic model

In this section hydraulic model layout is introduced and its functionality is explained. Figure 46 shows a sketch of the hydraulic model where its dimensions are defined in millimetres. It is also defined the cross-section (cross-section A) where flow velocity and flow depth measurements were made which is located about 1.10 meters of the hydraulic model's crest edge.

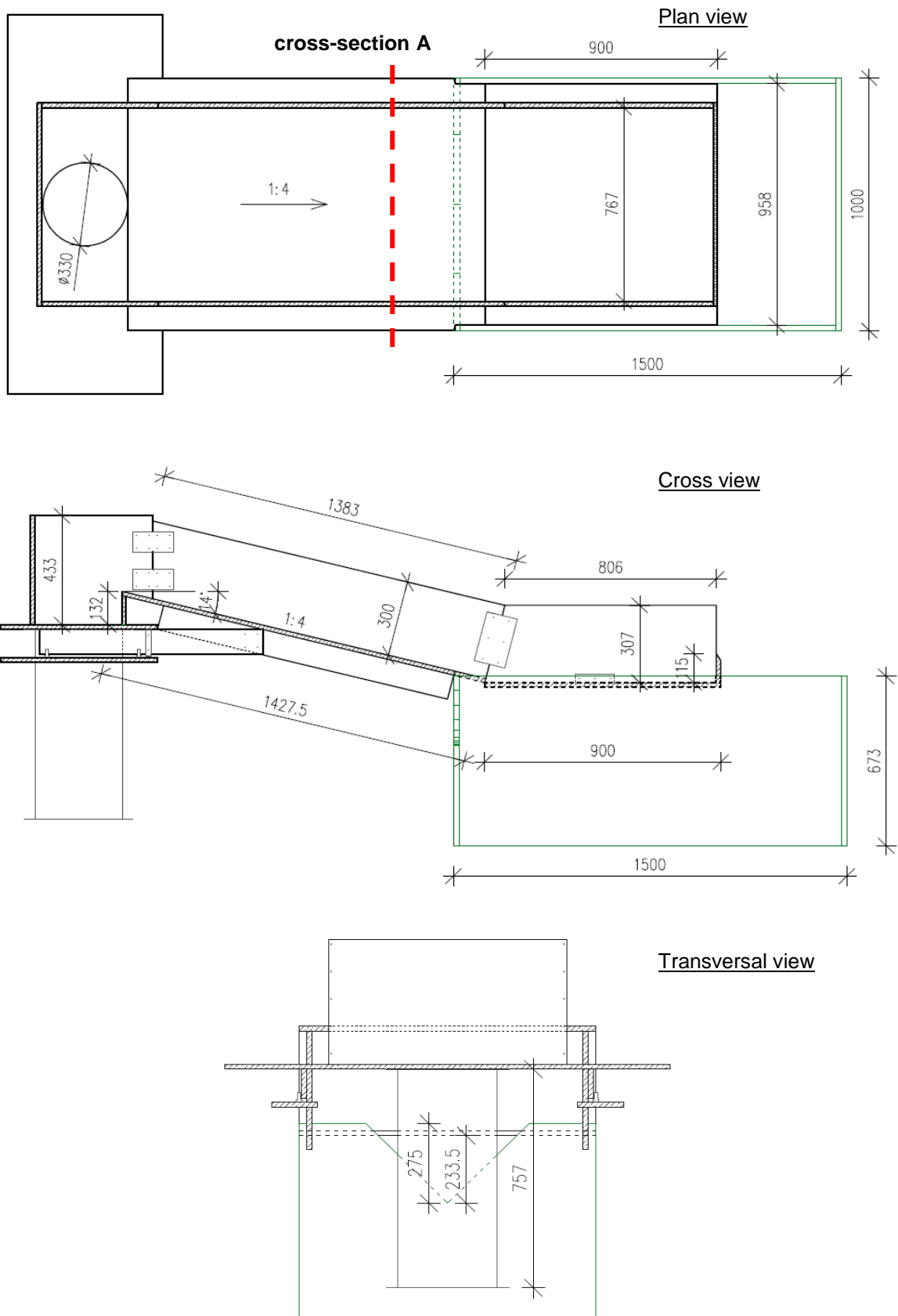


Figure 46. Dimensions of hydraulic model layout (in mm).

The bottom wooden panel had an inclination angle (β_0) of 14.04° , *i.e.*, with a steepness of 1:4 (V:H) and along with two sidewalls (made of wooden also) it formed a channel 1.43 m long, 0.77 m wide and 0.31 m high (Figure 46).

Typically the slope angle of a dike landside slope is 1V:3H ($\beta_0=18.43^\circ$) (Oumeraci *et al.*, 2005) which interfere with the flow velocity and flow thickness along the slope. It is obvious that overtopping flow velocities increase and related flow thicknesses decrease with increasing slope steepness. Accordingly, any conclusions taken from the performed overflow experiments are only applicable for dikes having a landside slope angle of 1V:4H with similar slope roughness as the hydraulic model.

The wooden channel continued downwards with a horizontal platform that simulated an embankment toe/berm and it had a length of 0.90 m, a width of 0.77 m and a depth of 0.31 m (Figure 46). The horizontal channel collected the sediments (sediment trap, Figure 47 on the left picture) that were transported by waterflow along the channel slope, forming a polder that was sealed at the channel edge with a vertical panel 0.11 m high.

As soon as tailwater level would increase beyond the panel elevation, water was released to a container with a length of 1.5 m, a width of 1.0 m and a depth of 0.67 m (external dimensions, Figure 46). This box could store water to a certain level (0.40 m) defined by a triangular weir or v-notch weir installed in its rear (Figure 47 on the right picture).



Figure 47. Sediment trap (hydraulic model's horizontal platform) releasing water to the container (on the left picture). Detail of v-notch weir installed in back part of the container (on the right picture).

After attaining a specific energy head, water was drained to an underground tank, also containing water, where a suspended pump was located (0.10 m above tank bottom). The pump allowed that water was constantly recirculating in the system.

According to the manufacturer specifications the pump had a maximum discharge capacity of 40.0 l/s (at 23.45 meter of water pressure). However, it was impossible to attain a constant value of Q_{max} for every experiment due to operational constraints related to the test facility. Thus the value of Q_{max} ranged from 29 to 36 l/s for the various overflow experiments.

Underground water was pumped through flexible pipe ($\varnothing=110$ mm), also beneath the ground, that led it to the measuring track ($\varnothing=125$ mm). In this segment of the system an electromagnetic flowmeter was installed to measure the discharge waterflow. The amount of water released to the hydraulic model was manually controlled by a valve which was placed immediately beside the electromagnetic flowmeter (downstream side of the device). Thereafter the waterflow was channelled into a vertical steel pipe with an internal diameter of 330 mm and a length of 0.76 m, which supplied the intake section. This section functioned as a reservoir from where the overtopping event would start and also where the hydraulic model's crest was located (Figure 49).

It can be noticed that the present hydraulic model lacks of an "earthen dike" crest sufficient long (distance w) to develop a critical flow regime over it, as shown in Figure 48 .

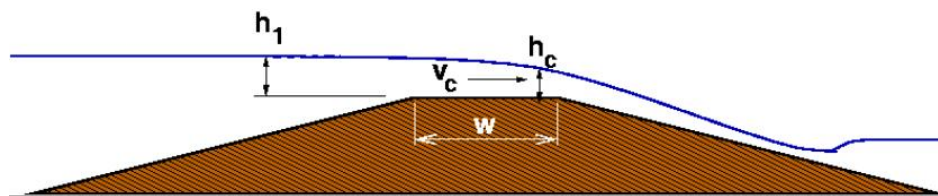


Figure 48. Steady overflow over an earthen embankment (Hughes *et al.*, 2011).

Therefore, the discharge passing over the dike crest cannot be estimated by the upstream head $h_1=H$ applying the broad-crested weir developed by Henderson (1966) (equation (1) in section 2.3.2). Since the dike crest configuration of the hydraulic model is different (Figure 49) than the one depicted by Figure 48, the discharge weir coefficient will be inevitably different than the one used in equation (1) ($C_f=0.5443$).

Due to the characteristics presented by hydraulic model water discharge flowing over the crest and landside slope of the model was assumed to be equal to the one measured by the electromagnetic flow meter (Q_i). Figure 49 gives a detail of hydraulic model's crest.

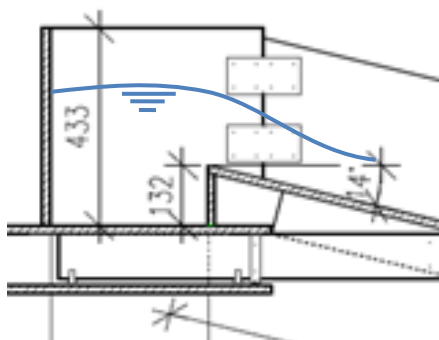


Figure 49. Detail of crest of the hydraulic model at the intake section (dimension defined in mm).

Figure 50 shows some components of hydraulic model described above.

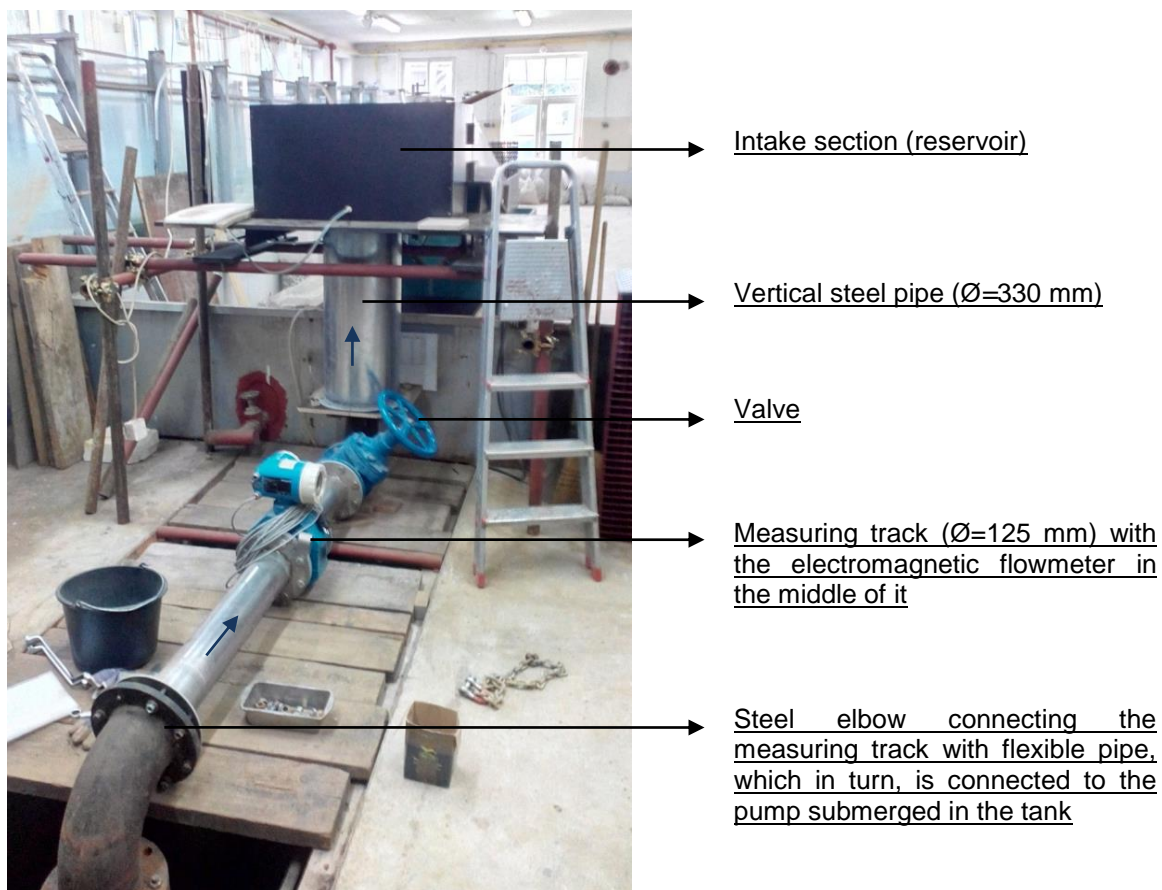


Figure 50. Auxiliary components of the hydraulic model.

3.1.2. Reinforced granular revetment

In this section the features related with preparation of the test channel are explained. The reinforced granular revetment that was installed on the hydraulic model is constituted by:

a) Foundation layer; b) Gravel layers (bottom and top layer); and c) Rolled Erosion Control Products (RECPs).

3.1.2.1. Foundation layer

The foundation layer was made of crushed stone (the same type used in railway lines), coarse gravel, with grain size varying between 32 and 64 millimetres, and a thin layer of sponge. It was decided to put a sponge layer between the bottom of the wooden channel and the rock material in order to provide enough bed roughness, so that the foundation stones and coarse gravel particles could remain stationary on the slope when facing the overflow loading. With the same purpose, it was also decided to install a piece of geosynthetic material in the upward edge of the slope by fixing it with nails to the channel bottom and holding crushed rock in place (Figure 51).



Figure 51. Foundation layer lying down at the hydraulic model channel bottom.

The first row of the channel foundation material (adjacent to the intake section) exhibit bigger frontal area upon which the water acts and hence, are less stable when facing an overtopping discharge. After turning on the pump for the first time during the foundation stability trial, the rock particles immediately moved when passing from a dry state to wet state. After, the installation of a piece of geosynthetic and the thin sponge layer the

foundation layer stood still when facing a 30.0 l/s discharge (which was the maximum discharge capacity of the pump). Afterwards, it was concluded that this first layer of rock material was steady and prepared to bear the granular material (that was intended to be tested) above it. The crushed stones and coarse gravel particles provided a base with large roughness that allowed effective interlocking with overlying granular material.

Moreover, it was also estimated the discharge required to submerge the foundation layer particles which was about 1.0-1.5 l/s. The foundation layer erosion behaviour was not subject of study of the present dissertation.

3.1.2.2. Gravel layer

Uniform sediments of various mean sediment sizes $D_{50}=6.1, 11.9, 23.9$ mm were used for the experimental tests (Table 12) in order to create three different erodible gravel beds (spread over the foundation layer) over which the RECPs were installed. A top granular layer was also placed beneath the RECPs. An ID was assigned to each type of gravel for identification purposes in the rest of this document.

Table 12. Characteristics of the sediments used in the experiments.

| Gravel | D_{min}/D_{max} mm | D_{50}/D_{75} mm | ρ_s kg/m ³ | ρ_d kg/m ³ | ρ_{sat} kg/m ³ | WA_{24} % | Manning's n s/m ^{1/3} |
|--------|-------------------------|-----------------------|-------------------------------|-------------------------------|-----------------------------------|----------------|-------------------------------------|
| s.A | 16/32 | 23,86/29.16 | 2678 | 2609 | 2634 | 1.00 | 0.0258 |
| s.B | 8/16 | 11,87/14.02 | 2654 | 2570 | 2620 | 1.22 | 0.0229 |
| s.C | 4/8 | 6,15/7.23 | 2652 | 2601 | 2620 | 0.73 | 0.0205 |

Note: ρ_{sat} is the saturated density of the sediment and WA_{24} is the sediment water absorption in 24hrs.

Figure 52 shows a detail of each gravel bed.



Figure 52. Coarse-grained soil samples for overtopping tests.

The sediments were homogenous, free of organic matter, and with a smooth and rounded appearance (Figure 52). The gravel layers did not exhibit any cohesion amongst the particles, presenting a lot of empty spaces between the particles where water could filter down.

There is a variety of systems (Figure 53) that establishes a classification criterion based on the size of the sediment particles (Zhu, 2006). According to the Unified Soil Classification System (USCS) the granular material s.A can be classified as coarse gravel ($19.00 < D_{50} < 75.00$) and the other two types, s.B and s.C, as fine gravel ($4.75 < D_{50} < 19.00$).

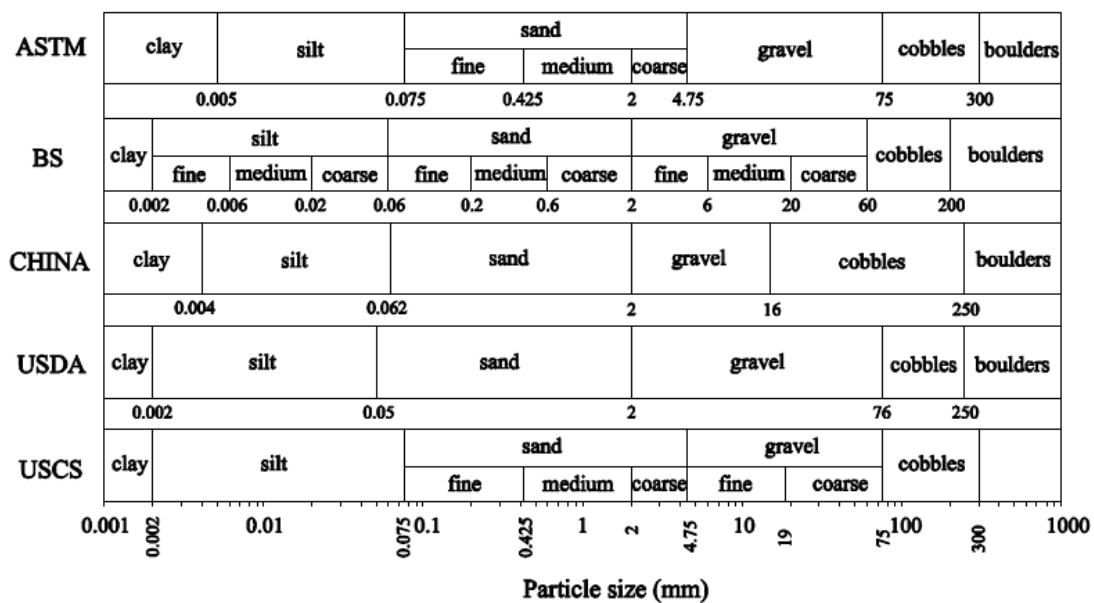


Figure 53. Most widely accepted sediment classification systems (Zhu, 2006).

Manning’s n for granular soils depends on the median grain size D_{50} (m) as shown in equation (46) (Hassanzadeh, 2012):

$$n = 0.048D_{50}^{1/6} \tag{46}$$

Figure 54 shows the particle size distributions of all types of gravel used for overtopping experiments. It can be seen that gravel samples possess a uniform gradation (due to the high steepness of the curves). This data was used to estimate the parameters D_{50} and D_{75} .

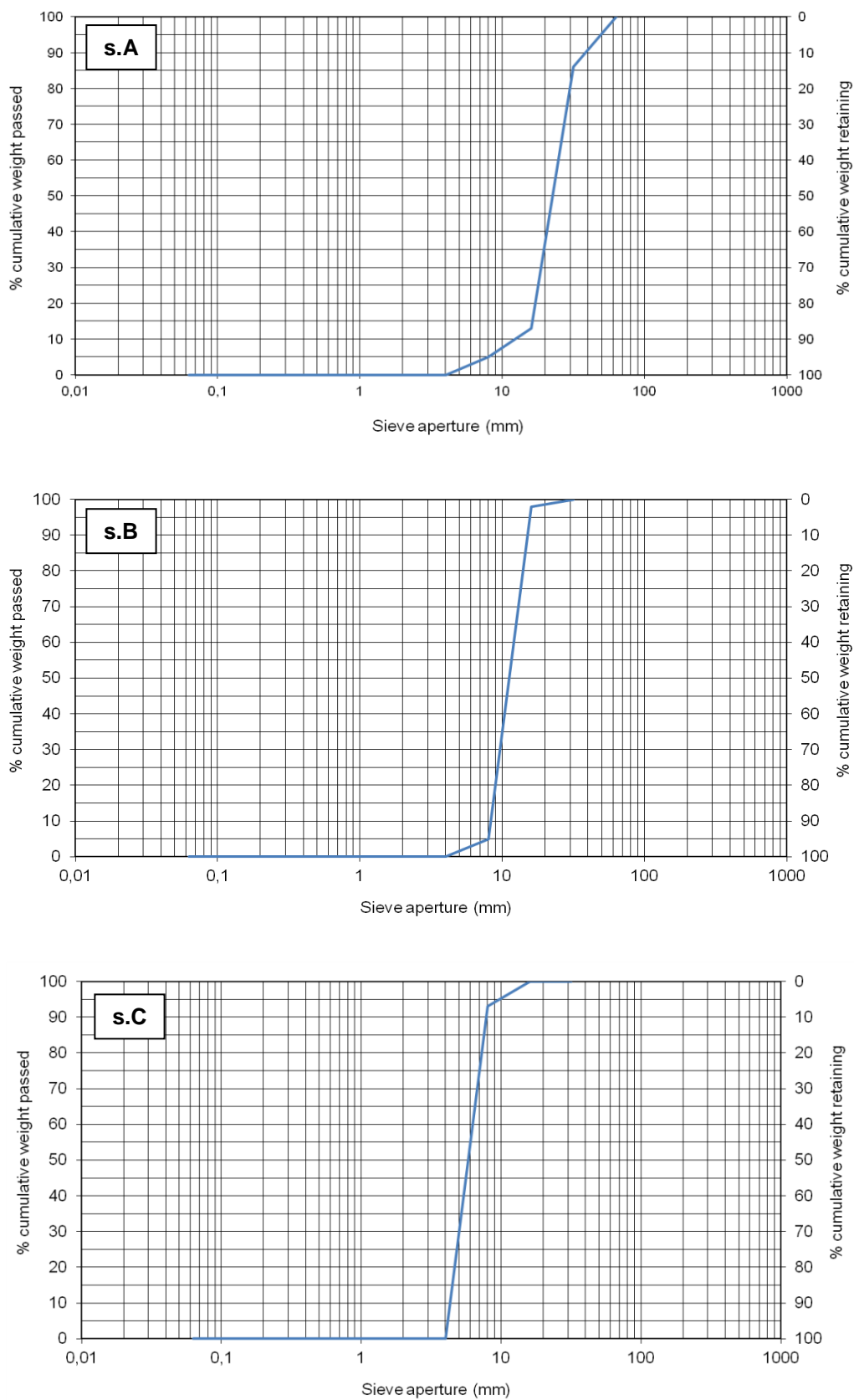


Figure 54. Particle size distribution of the gravel material used for hydraulic model's bottom and top layer.

3.1.2.3. Rolled Erosion Control Products

During the overtopping experiments six types of Rolled Erosion Control Products (RECPs) were tested under overflow conditions. According to the Erosion Control Technology Council (ECTC) a RECP is “a temporary degradable or long-term non degradable material manufactured or fabricated into rolls designed to reduce soil erosion and assist in the growth, establishment and protection of vegetation”. Table 13 and Figure 55 introduce and summarize the several RECPs tested. A product ID was assigned to each RECP for identification purposes in the rest of this document.

Table 13. Product details of RECPs used for laboratory experiments.

| RECPs | Manufacturer | Model | Product type | Raw material |
|-------------------------------|---------------------------------------|--|---|---|
| M ₁ | TENAX® | LBO SAMP 330 | Bi-oriented geogrid | Polypropylene (PP) |
| M ₂ | NAUE® | COMBIGRID® 40/40 Q1 151 GRK 3 | Bi-oriented geogrid with needle-punched nonwoven geotextile | PP (both) |
| M ₃ ⁽¹⁾ | NAUE® | Adapted from COMBIGRID® 40/40 Q1 151 GRK 3 | Bi-oriented geogrid | PP |
| M ₄ ⁽²⁾ | - | unknown product | Bi-oriented geogrid | - |
| M ₅ | Tensar® / North American Green® | V _{MAX} C350 | Permanent 3D turf reinforcement matting | Top and bottom net: PP Centre net: PP corrugated Matrix: Coconut fiber |
| M ₆ | Tensar® / North American Green® | V _{MAX} P550 | Permanent 3D turf reinforcement matting | Top and bottom net: PP Centre net: PP corrugated Matrix: PP fiber |

1: RECP M₃ was adapted from RECP M₂ by removing the nonwoven geotextile from the mat; 2: The manufacturer of product M₄ is unknown.

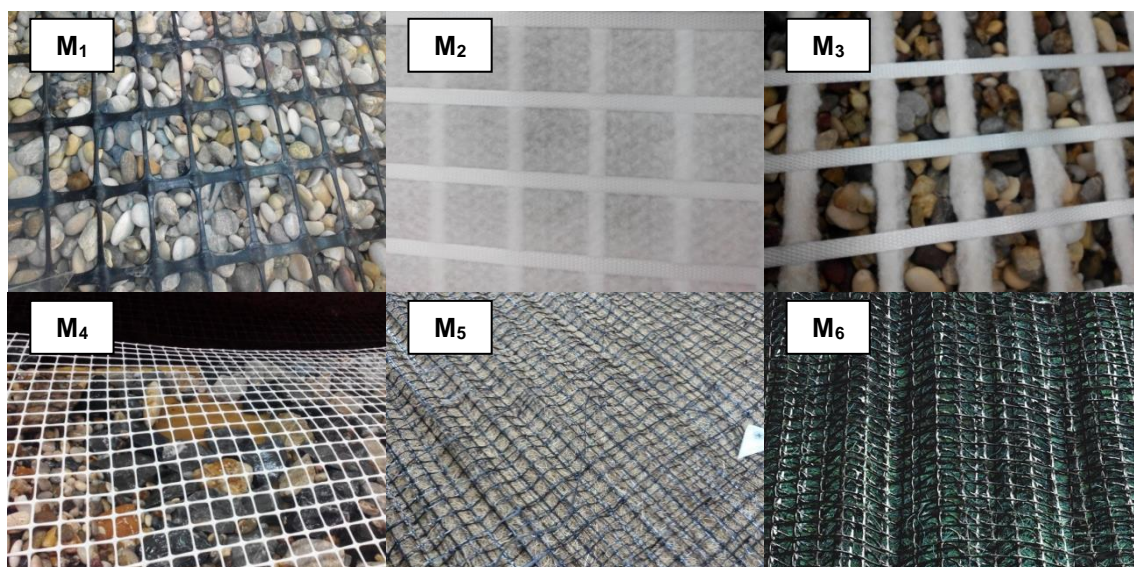


Figure 55. Detail of RECPs (M₁, M₂, M₃, M₄, M₅ and M₆) used in the experiments.

Installation of the RECP in the test channel

The RECP was firmly embedded in the gravel layer diving it in two parts and it was previously trimmed to fit in the channel dimensions. The granular layer underneath it and in contact with the foundation layer (approximately 0.04 m thick) is thicker than the upper layer (approximately 0.02 m thick). The granular layers were spread over the foundation layer and RECP, by placing sediments in loose lift layers, without any mechanical compaction procedure. Note that compaction of the soil generally increases its shear strength, decreases its compressibility, and decreases its permeability (Gresser, 1996).

The RECP was attached to the wooden panel of the model slope with nails (using a drill) that intended to function like anchors (Figure 56).

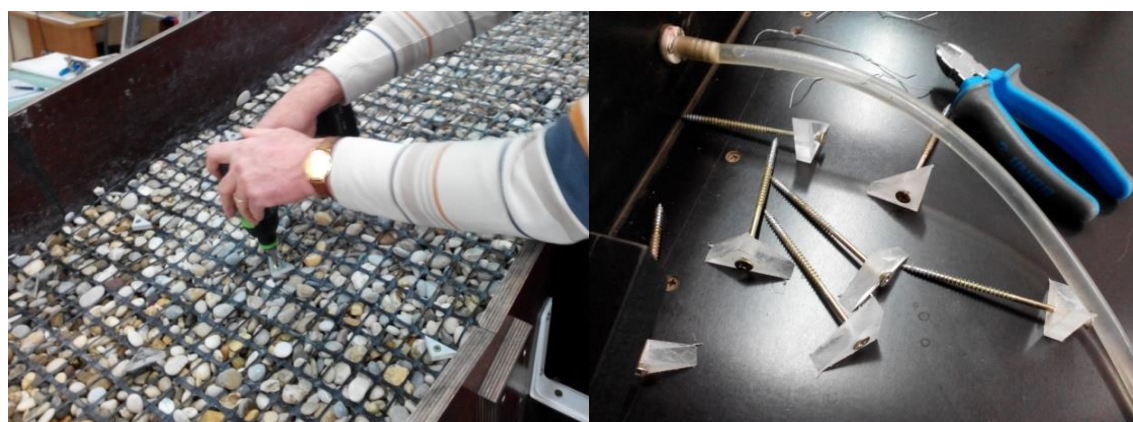


Figure 56. Installation of RECP (M₁) over the gravel layer of the hydraulic model slope (on the left picture). Detail of the system used to function as anchors: nails with a plastic head (on the right picture).

These fixing points do not allow vertical translations of the mat by creating tension on it. This way the mat provides compressive stresses on underlying material keeping it locked in place. All together, these materials referred above, created a composite surface layer approximately 0.10 m thick.

Anchorage pattern adopted for the RECPs

The effectiveness of a protection system depends greatly upon the type and pattern of the anchors (Miller *et al.*, 2012). The various RECPs were anchored to underlying “soil” material on the channel slope using a symmetric anchorage pattern as demonstrated in Figure 57, consisting of an anchorage density of 8.2 anchors (nails) per square meter.



Figure 57. RECP M₅ (Vmax C350[®]) (on the left picture) and RECP M₆ (Vmax C350[®]) (on right the picture) with anchorage density of 8.2 anchors/m² over the channel slope.

Note that these “anchors” do not constitute a certified product available in the market, but an improvised solution (ordinary nail with a plastic head) created to perform the experimental tests. The nail arrangement over the testing channel was not defined according to any protocol and the only concern was to install sufficient nails to ensure that the mat was placed directly in contact with the gravel layer in every locations (Figure 57). It is important to highlight that direct contact between the mat and underlying material is vital for preventing the potential erosion at its interface (Miller *et al.*, 2012).

The anchor type and length and anchorage pattern should have been defined according to the manufacture installation guidelines (if available) in order to obtain the fullest

performance potential in terms of erosion protection of the respective RECP during the overflow experiments (Miller *et al.*, 2012). Accordingly, the installation guidelines for anchoring the TRMs M₄ and M₅ (Figure 57) were consulted in order to get information about the type of anchors available and recommended anchorage patterns. Are recommended three possibilities of anchor types: U-shaped/wire staples, percussion earthen anchors and circle top pins. In case of a downstream slope that will convey considerable amounts of water during seasonal floods (*i.e.*, an earthen spillway) the following anchorage pattern (frequency and spacing) is recommended by the manufacturer installation guide (Tensar[®]), as shown in Figure 58.

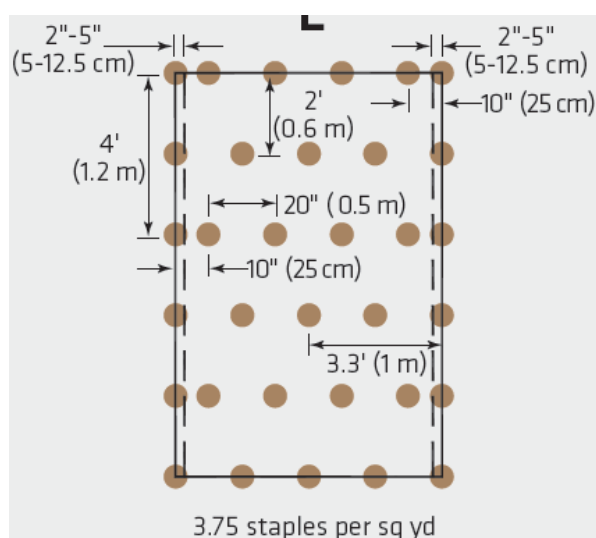


Figure 58. Recommended anchorage pattern for RECPs M₄ and M₅ by the manufacturer, consisting of anchor density of 4.5 anchors/m² (Tensar[®], 2010).

Comparing the “last resort solution” adopted for anchoring the RECPs (nails with a plastic head) with the product installation guidelines, it can be concluded that the experimental anchorage density was appropriate for fixing the mats M₅ and M₆ to the hydraulic model channel bottom. In fact, the adopted anchorage density was almost twice the recommended density by the manufacturer (Figure 58). Even if certified anchors (wire staples for example) had been provided, they would have been useless since the mat underlying material is not a cohesive soil with sufficient depth to ensure adequate pull-out resistance.

Manufacturer technical specifications

Table 14 outlines some RECPs mechanical properties including: aperture size, mass per unit area, mat thickness, ultraviolet stability and tensile strength in the machine direction (M_D) and cross direction (T_D) at various strain (ϵ) levels.

Table 14. Mechanical properties of the RECPs used in the overtopping tests.

| RECPs | Aperture size MD×TD mm×mm | Mass per unit area g/m ² | Thickness mm | UV stability (1000 hr) % | Tensile Strength MD/TD | | |
|-------------------------------|---------------------------------|--|-----------------|--------------------------------|------------------------|------------------|------------------------|
| | | | | | at 2% ϵ | at 5% ϵ | at ultimate ϵ |
| | | | | | kN/m | | |
| M ₁ | 40×27 | - | - | - | 10.5/10.5 | 21.0/21.0 | 30.0/30.0 |
| M ₂ geogrid | 31×31 | 240 | - | - | 16.0/16.0 | 32.0/32.0 | 40.0/40.0 |
| M ₂ geotextile | - | 150 | - | - | - | - | 7.5/11.0 |
| M ₃ | 31×31 | 240 | - | - | 16.0/16.0 | 32.0/32.0 | 40.0/40.0 |
| M ₄ ⁽¹⁾ | 20×20 | - | - | - | - | - | - |
| M ₅ | 13×13 | 624 | 18.54 | 86 | - | - | 8.70/10.20 |
| M ₆ | 13×13 | 723 | 18.29 | 100 | - | - | 21.1/17.7 |

MD=Machine direction (longitudinal to the roll); TD=Transverse direction (across roll width). This technical information is provided by the manufacture data sheets of the various mats. 1: This technical information was not provided

Table 15 presents manufacturer-reported maximum permissible values for shear stress and velocity of TRMs M₅ and M₆ during an overtopping event. It is also given the Manning's n according to flow thickness. These values are based on product performance for three vegetation life stages (unvegetated, partially vegetated and fully vegetated) during recognized testing methods (ASTM or other industry standards), for short (duration is less than two hours) and long testing duration flows.

Table 15. Maximum design permissible shear stress and maximum design permissible velocity values of TRMs M₅ and M₆.

| RECPs | Vegetation condition | Shear stress (Pa) | | Velocity (m/s) short duration | Roughness factor unvegetated | |
|----------------|------------------------------------|-------------------|---------------|----------------------------------|------------------------------------|---------------------|
| | | short duration | long duration | | flow depth (m) | Manning's <i>n</i> |
| M ₅ | unvegetated | 153 | 144 | 3.2 | ≤0.15 | 0.041 |
| | partially vegetated ⁽¹⁾ | 480 | 480 | - | | |
| | fully vegetated ⁽¹⁾ | 576 | 480 | 6.0 | 0.15 < <i>h_w</i> < 0.60 | from 0.040 to 0.013 |
| M ₆ | unvegetated | 191 | 156 | 3.8 | | |
| | partially vegetated ⁽¹⁾ | 576 | 576 | - | | |
| | fully vegetated ⁽¹⁾ | 576 | 576 | 7.6 | | |

1: The performance values are valid for vegetation belonging to retardance class A, B and C. This technical information is provided by the manufacture data sheets of the mats (Tensar®).

In section 2.6.2.2 turf reinforcement mats were well characterized unlike other types of RECPs such as geotextiles and geogrids (M₁ and M₂). TRMs/HPTRMs are specially fabricated to withstand overflowing water volumes and provide erosion control over the boundaries of dike crest and slope and, hence, these products constitute a topic of interest for this dissertation rather than geotextiles and geogrids. However, according to manufacturer data sheets products like geogrids and geotextiles can also be adapted to perform non-structural erosion control functions, despite not reaching similar performance levels such as TRMs. Hewlett *et al.* (1987) (*in* Nelsen, 2005) stated that materials with a two dimension structure do not provide reinforcement but only maintenance of vegetation's natural performance levels (which are lower than performance levels of TRMs protection systems)

Next a brief description about geogrids' typical main functions and applications is provided. According to the manufacture geogrids are designed primarily to provide stabilization, confinement and reinforcement of soil through mechanical interlocking of the aggregate/earth within the mat apertures. Geogrids can also control soil deformation (reducing soil settlement) and distribute the loading over the soil (improving soil bearing capacity). Examples of application are shown in Figure 59.



Figure 59. Application of a composite product of a geogrid and geotextile (Combigrig[®]) for soil reinforcement (on the left picture) and application of a geogrid layer only with U-shaped fasteners over a steep slope (on the right picture) (figure extracted from www.naue.com, 2013).

Their main applications include: sub-soil stabilization underneath roads, railroads and airport runways and base, sub-base and slope reinforcement of embankments and earthen dams (structural reinforcement using soil fasteners). These applications have in common the fact of both having a geogrid installed over a horizontal plane, normal to acting loads, which raises suspicions about its application in steep slopes without a proper anchor arrangement system (parallel to the slope).

Sometimes a geogrid is associated with a geotextile in order to combine reinforcement, filtration (within flood defence embankment) and separation (of adjacent soil types) functionalities in one single product, such as RECP M₂. This mat is a composite product of a geogrid with a needle-punched nonwoven geotextile firmly welded between the reinforcement bars. The needle-punched nonwoven filter geotextile prevent migration of fine particles and thus internal erosion. The manufacture does not make any reference about its applicability in earthen dikes in terms of external erosion control but various references are made about their capability to reinforce soil and provide the stabilization of steep slopes.

Haselsteineir *et al.* (2008) presented an overflow protection system for dike refurbishment where a geosynthetic material similar to RECP M₂ (geogrid+geotextile) was installed to provide soil reinforcement of the dike and thus avoid erosion phenomena (consult section 2.8.2 for more detailed information about Haselsteiner *et al.* experimental study).

3.2. Instrumentation

3.2.1. Electromagnetic flowmeter

The electromagnetic flowmeter (Endress+Hausser®, Propline Promag 53P®) (Figure 60) consists of a transmitter (“Promag 53”) and a sensor (“Promag P”) that has two field coils and two electrodes, both set opposite each other in the measuring tube. The coils generate a constant magnetic field over the entire cross-sectional area of the measuring tube and the electrodes, installed in the wall of the tube at a right angle, pick up and measure the electrical voltage induced by the passage of waterflow through it (Faraday’s law of magnetic induction). This voltage, captured in the electrodes, is directly proportional to the flow velocity in the pipe. Therefore, the discharge through the pipe can be calculated for a particular cross-sectional area and then the data can be directly read from the transmitter (Figure 60, right side).



Figure 60. Electromagnetic flowmeter utilized to measure the flow discharge.

3.2.2. Velocimeter

On the model’s downstream slope a mini current meter (SEBA HYDROMETRIE®) (Figure 61) was used to estimate the velocity of overtopping water. There was only one measurement location, (defined as cross-section A in Figure 46) and it placed in the end of the model’s channel slope, about 1.10 meters of the crest edge. Near this location water flow is expected to reach uniform conditions where the flow thickness is constant and the velocity is highest, if the slope is long enough to allow it. Note that for higher discharges

this assumption may not be valid. This subject will be discussed further below (section 3.3).

The mini propeller used had a measuring range of 0.03 to 2.5 m/s and worked in partnership with a signal counter. This device counted impulses generated by the flow (R_i) in a defined measurement interval. Afterwards, the flow velocity could be estimated according to formula (47) or (48) provided by the flowmeter's manufacturer. These equations are a function of the number of propeller revolutions per second (N), *i.e.*, the ratio between the impulses and the measurement interval. This formula is calibrated to be used for a propeller with a diameter of 30 mm and pitch of 100 mm. It was set a measurement interval of 20 seconds.

if $N < 1.16$:

$$V = 10.57 \cdot N + 1.90 \quad (47)$$

if $N \geq 1.16$:

$$V = 10.26 \cdot N + 2.26 \quad (48)$$

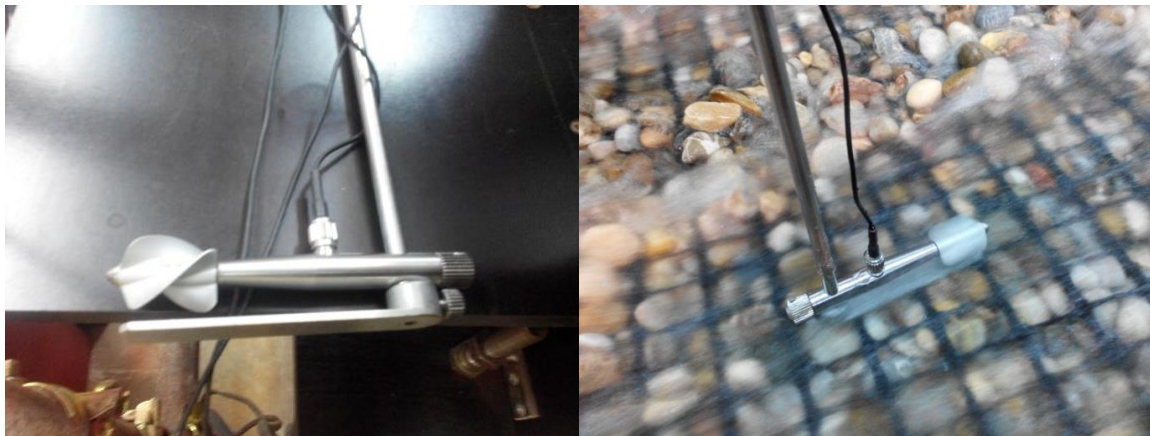


Figure 61. Velocimeter used for a rough estimation of flow velocities in the vicinity of slope's toe of the hydraulic model.

In order to obtain an accurate number of propeller revolutions the tip of velocimeter has to be completely submerged (at least 4/5 cm of flow thickness were required to submerge the device). Unfortunately, waterflow depth on the channel was not high enough to assure it, as shown in Figure 61. This fact has implications on the estimation of the number of propeller revolutions and consequently, in measurement of waterflow average velocity.

It was also impossible to record the flow thickness correspondent to velocity that was being measured. Nevertheless, the experiment was done in order to get more familiar with this common laboratory procedure and to check the range of values of velocity given by the device, even if these values could be considered misleading. Accordingly, the author is aware that this measurement device is not appropriate to extract reliable velocity values under the experimental conditions such as presented herein.

3.3.Experimental program

The complete test program was divided into three phases according to type of sediment (s.A, s.B or s.C) used in the overtopping experiments. So, phase I corresponds to the experiments involving the material s.A, phase II, material s.B and phase III, material s.C.

The hydraulic model contains in all experiments one foundation layer (bottom layer) where the granular material and the respective reinforcement solution, with a RECP, will be placed.

The experimental procedure consists, basically, in releasing a certain amount of water that is progressively increased in time, over a reinforced granular layer and observing the effect that waterflow shear forces exert on its configuration and thus evaluating its stability performance. If the surface layer protection (reinforced or not with a RECP) holds on the flow discharge Q_i for a certain duration (between 5 to 10 minutes) without exceeding a certain defined threshold condition, a larger discharge Q_{i+1} is applied. The process can be repeated until the maximum discharge capacity of the pump (Q_{max}) is reached.

Each phase of the experiment can be divided into three distinct parts or sub-phases:

(1) The main goal of the first part of the experiment is to find out at which discharge the gravel particles above the RECP (gravel top layer) start to be transported by the waterflow (Q_1). Note that a displacement of an individual gravel particle that is transported by the waterflow and finds another equilibrium position over the slope was not considered as the beginning of sediment motion;

(2) In the second part of the experiment, the discharge is progressively risen in order to record the value of water discharge that causes sediment transport of the granular material underneath of the RECP (gravel bottom layer) (Q_2). In some tests this threshold value was not attained because the experiments required a higher Q_{max} .

(3) It was also tested the behaviour of the granular layer without any kind of RECP and noted the discharge value responsible for incipient motion of the gravel particles with loosen arrangement over the channel (Q_3). This task is included in part three of the experiment. The information obtained from these tests provided a basis for assessing the erosion protection afforded by the RECPs.

In order to estimate threshold discharges (Q_1 , Q_2 and Q_3) during the experiments, related to stability performance of reinforced granular layers, certain damage threshold conditions needed to be previously established. Accordingly, excessive erosion criteria associated with threshold discharge Q_1 was defined as removal of granular soil (about 2 cm) above the mat, deep enough to expose the underlying mat to overflow shear stresses; excessive erosion criteria for Q_2 was defined as removal of granular soil (about 4 cm), beneath the mat, deep enough to expose the underlying foundation layer (crushed stone and coarse gravel); and lastly, threshold discharge Q_3 was defined as removal of bare granular soil (about 4 cm) (without the influence of the mat/RECP) deep enough to expose the underlying foundation layer.

According to standard ASTM D6460's specifications (*in* Nelsen, 2005) performance threshold values (permissible shear stress and correspondent permissible flow velocity for a certain discharge Q) should be defined in accordance with an erosion criterion that establishes a maximum average soil loss beneath the RECP of 12.7 mm (over the entire channel bottom). Note that the permissible shear stress characteristic of the RECP is the shear stress necessary to cause an average of 12.7 mm of soil loss over the entire channel bottom. However, during the tests only visual inspection was done to assess the soil loss beneath the mat. The estimation of threshold discharge Q_2 did not have into consideration this specification because it was difficult to control and measure granular soil loss due to characteristics presented by the underlying bed layer. As stated, this layer was relatively thin, constituted only by loosen gravel particles, poorly graded, that have not been well compacted and hence, presented an uneven surface at "closer-look" perspective (scale of an individual gravel particle). As a result, individual gravel particles were unstable even with relatively small overflowing discharges, even though the gravel layer remained stable as a whole. As s.A and s.B material possessed a grain size ($D_{50}=2.4$ cm for s.A and $D_{50}=1.2$ cm for s.B) superior to the maximum soil loss defined by the protocol (ASTM D6460), this criterion was non-inapplicable for this kind of non-cohesive erodible

bed. Note that typically gravel layers have a filtration purpose within the earthen dike structure and thus are more suitable for the use in pervious sections preventing particle soil migration from the previous core (CIRIA *et al.*, 2013). Therefore ASTM D6460 procedure is more suitable for cohesive and pervious soils such as sandy clay (CL) (Amini and Li, 2012) or sandy silty clay (ML-CL) (Nelsen, 2005) (included in the group of fine-grained soil according to USCS classification system), that traditionally can be found on the surface clayey layer of vegetated earthen embankments. Thus, the aspects related to erodibility of an underlying real-world embankment soil were not simulated in these tests.

The soil over which a RECP will be installed (in order to create an unvegetated or vegetated reinforced erodible soil bed) should be well characterized, including the percentage of gravel, sand, silt and clay in its composition, liquid limit and plasticity index, and mechanically compacted before the testing (compaction should be verified to be 90 percent of Proctor Standard density using ASTM D 698, sand cone method) (Sprague, 2011). In the presence of a cohesive soil (with clay or/and silt) previously compacted and levelled side-to-side, bed channel elevations at pre-determined cross-sections along the testing channel should be measured prior and after each flow event (with a constant discharge) to determine the soil loss quantity. Accordingly, flow must be stopped between one-hour long (duration recommended by ASTM D6460) flows events to proceed with the bed elevation readings, using a total station for example. Afterwards this data has to be converted to Cumulative Clopper Soil Loss Index (CSLI) as outlined in ASTM D6460 (*in* Nelsen, 2005). The CSLI assigns a value of zero to any point in the control volume demonstrating a soil gain. The zero value is then averaged in with all other points in the control volume. Afterwards, the values of CSLI shall be plotted against shear stress (averaged over the entire test section) in order to define a permissible (or limiting) shear stress at RECP installed over an erodible soil. Figure 62 shows an example related to the estimation of permissible shear stress of a RECP product according to the established threshold soil loss (0.5 in or 12.7 mm) (Sprague, 2011) The permissible shear stress of a RECP lining is determined both by the underlying soil properties as well as those of the RECP (Kilgore and Cotton, 2005). In section 3.1.2.3 the RECPs used in the overflow experiments were introduced but only permissible shears stresses for mats M₅ and M₆ were provided by the manufacture. If time series of (normal) flow thickness (created by increasing flows applied to the test section for 1 hour each) are measured in testing channel

alongside the correspondent soil loss, permissible shear stresses on the lining can also be provided for M_1 and M_2 , like Nelsen (2005) did in his full-scale overtopping experiments.

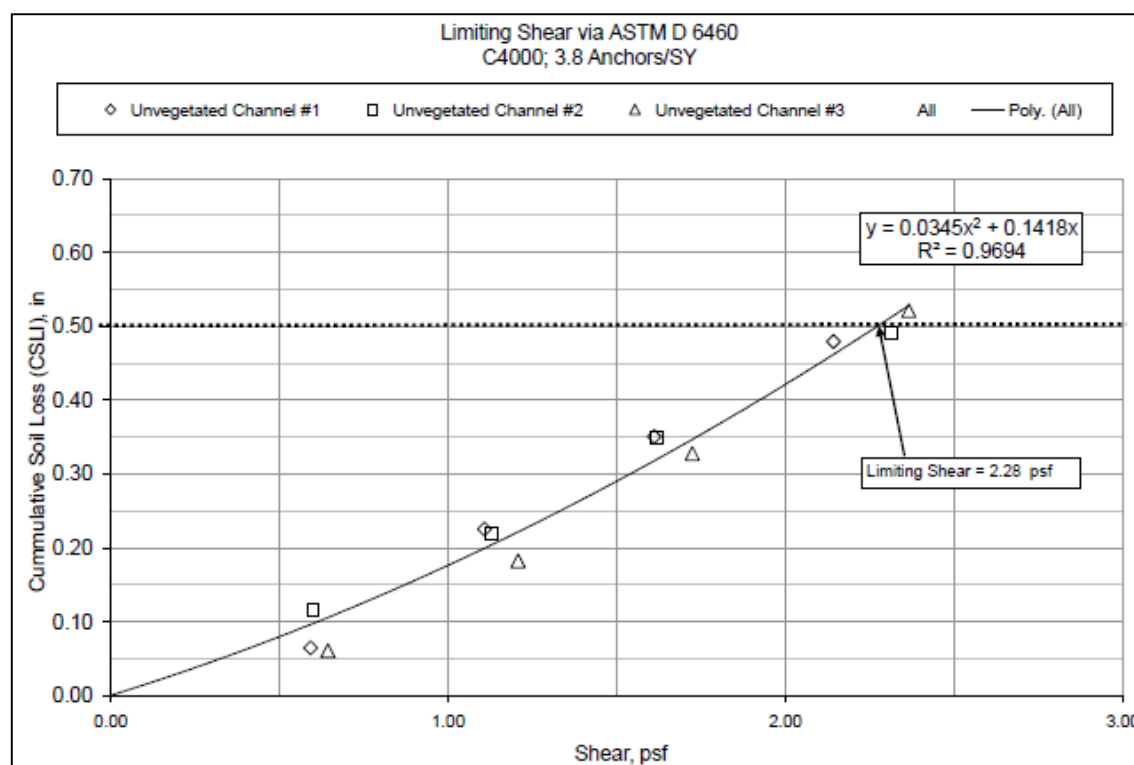


Figure 62. CSLI (beneath the mat) versus shear stress on RECP (Sprague, 2011).

A fourth performance threshold Q_4 (different from “soil” loss measurements) associated with movement of the mat or with its mechanical integrity, could have been defined. However, it was highly unlikely that the mat would have been mechanically compromised by the low discharge flows generated in testing facility. Accordingly, due to the limited conditions available in the facility, establishing this threshold condition would make no sense in this context.

Summary of experimental program

Tables 16 to 18 summarize the experimental program in order to give the reader an organized overview of the laboratory procedure’s sequential steps. The measured discharge values and the various overflow durations for phases I, II and III are presented, respectively, in Table 16, Table 17 and Table 18. Each table corresponds to a different phase of the overflow experiments and presents the discharge values that were set by the electromagnetic flowmeter, alongside with the duration of the overflow event created. It is also possible to perceive the time gap between two consecutive set discharges.

For example, according to Table 16 during overflow experiment “s.A+M₁” 10 sequential, increasing flows were applied to the testing section for 51 minutes (D_{total}).

Typically, a continuous one-hour flow (short duration testing) over the protection system should be guaranteed at each discharge level as good practice experimental procedure (ASTM D6460) (*in* Sprague, 2011), in order to determine hydraulic performance thresholds of RECPs over cohesive soil beds. However, for the present overflow experiments this criterion was not applied. Since the non-cohesive granular material tested possessed a large grain size with absence of fines, the overflow duration is not so relevant to assess sediment motion as for cohesive clayey soils, much more susceptible to fatigue. Accordingly each discharge was run for only a small time period (5-10 minutes).

Table 16. Measured discharge values and the various overflow durations for phase I.

| s.A (only) | | s.A+M ₁ | | s.A+M ₂ | | s.A+M ₃ | | s.A+M ₄ | | s.A+M ₅ /M ₆ | |
|-------------|-------|--------------------|-------|--------------------|-------|--------------------|-------|--------------------|-------|------------------------------------|-----|
| Time | Q | Time | Q | Time | Q | Time | Q | Time | Q | Time | Q |
| h:min | l/s | h:min | l/s | h:min | l/s | h:min | l/s | h:min | l/s | h:min | l/s |
| 10:22 | 4.9 | 13:38 | 5.1 | 14:51 | 2.5 | 14:14 | 5.0 | 14:54 | 5.0 | - | - |
| 10:26 | 7.5 | 13:43 | 7.5 | 14:54 | 5.0 | 14:18 | 7.5 | 14:57 | 7.5 | | |
| 10:32 | 10.0 | 13:48 | 10.1 | 14:59 | 7.5 | 14:23 | 8.5 | 15:05 | 8.5 | | |
| | 0.0 | 13:54 | 12.5 | 15:03 | 10.0 | 14:26 | 9.0 | 15:07 | 9.0 | | |
| D_{total} | 10min | 13:57 | 15.0 | 15:20 | 7.5 | 14:30 | 9.5 | 15:12 | 9.5 | | |
| 15:21 | 5.0 | 14:03 | 17.5 | 15:25 | 8.5 | 14:37 | 10.0 | 15:16 | 10.0 | | |
| 15:25 | 7.5 | 14:09 | 20.0 | 15:28 | 9.0 | 14:42 | 10.5 | 15:20 | 10.5 | | |
| 15:28 | 8.5 | 14:16 | 22.5 | 15:31 | 9.5 | 14:46 | 11.0 | 15:30 | 11.0 | | |
| 15:32 | 9.0 | 14:21 | 25.0 | 15:34 | 10.0 | 14:50 | 11.5 | 15:34 | 11.5 | | |
| 15:34 | 9.5 | 14:29 | 29.6 | | 0.0 | 14:53 | 12.0 | 15:46 | 33.5 | | |
| | 0.0 | | 0.0 | | | 14:58 | 12.5 | | 0.0 | | |
| D_{total} | 13min | | | | | 15:03 | 15.0 | | | | |
| 14:07 | 9.5 | | | | | 15:08 | 20.0 | | | | |
| 14:14 | 10.0 | | | | | 15:13 | 35.6 | | | | |
| 14:17 | 10.5 | | | | | | 0.0 | | | | |
| 14:26 | 11.0 | | | | | | | | | | |
| 14:31 | 11.5 | | | | | | | | | | |
| | 0.0 | | | | | | | | | | |
| D_{total} | 24min | D_{total} | 51min | D_{total} | 43min | D_{total} | 36min | D_{total} | 40min | D_{total} | - |

D=Overflow duration. Symbol “-“ means that the experiment was not performed.

Table 17. Measured discharge values and the various overflow durations for phase II.

| s.B (only) | | s.B+M ₁ | | s.B+M ₂ | | s.B+M ₃ | | s.B+M ₄ | | s.B+M ₅ /M ₆ | |
|--------------------------|-------|--------------------------|-------|--------------------------|-------|--------------------------|-------|--------------------------|-------|------------------------------------|-----|
| Time | Q | Time | Q | Time | Q | Time | Q | Time | Q | Time | Q |
| h:min | l/s | h:min | l/s | h:min | l/s | h:min | l/s | h:min | l/s | h:min | l/s |
| 13:06 | 2.1 | 12:52 | 2.0 | 15:23 | 2.5 | 12:47 | 2.5 | 13:47 | 2.0 | - | - |
| 13:15 | 2.5 | 12:55 | 3.0 | 15:26 | 3.0 | 12:52 | 3.0 | 13:52 | 2.5 | | |
| 13:22 | 3.0 | 12:58 | 3.5 | 15:30 | 4.0 | 12:57 | 3.5 | 13:57 | 3.0 | | |
| 13:26 | 3.5 | 13:05 | 4.0 | 15:37 | 7.5 | 13:01 | 4.0 | 13:59 | 3.5 | | |
| | 0.0 | 13:09 | 5.0 | | 0.0 | 13:05 | 5.0 | 14:13 | 35.7 | | |
| | | 13:11 | 6.0 | | | 13:08 | 6.0 | | 0.0 | | |
| | | 13:15 | 7.0 | | | 13:10 | 7.0 | <i>D_{total}</i> | 26min | | |
| | | 13:18 | 8.0 | | | 13:15 | 7.5 | 14:46 | 10.0 | | |
| | | 13:23 | 9.0 | | | 13:17 | 8.0 | 14:47 | 12.5 | | |
| | | 13:27 | 10.0 | | | 13:20 | 9.0 | 14:51 | 15.0 | | |
| | | 13:29 | 11.0 | | | 13:23 | 10.0 | 14:54 | 17.5 | | |
| | | 13:34 | 12.0 | | | 13:27 | 12.0 | | 0.0 | | |
| | | 13:37 | 13.0 | | | 13:32 | 13.0 | | | | |
| | | 13:39 | 14.0 | | | 13:35 | 14.0 | | | | |
| | | 13:41 | 15.0 | | | 13:37 | 15.0 | | | | |
| | | 13:45 | 16.0 | | | 13:43 | 17.0 | | | | |
| | | 13:46 | 17.0 | | | 13:46 | 18.0 | | | | |
| | | 13:48 | 18.0 | | | 13:49 | 20.0 | | | | |
| | | 13:50 | 19.0 | | | 13:53 | 22.0 | | | | |
| | | 13:53 | 20.0 | | | 13:57 | 25.0 | | | | |
| | | 13:55 | 22.0 | | | 14:02 | 27.0 | | | | |
| | | 13:58 | 24.0 | | | 14:07 | 35.1 | | | | |
| | | 14:01 | 27.0 | | | | 0.0 | | | | |
| | | | 0.0 | | | | | | | | |
| <i>D_{total}</i> | 20min | <i>D_{total}</i> | 49min | <i>D_{total}</i> | 14min | <i>D_{total}</i> | 1h20m | <i>D_{total}</i> | 41min | <i>D_{total}</i> | - |

D=overflow duration. Symbol “-“ means that the experiment was not performed.

Table 18. Measured discharge values and the various overflow durations for phase III.

| s.C (only) | | s.C+M ₁ /M ₃ | | s.C+M ₂ | | s.C+M ₄ | | s.C+M ₅ | | s.C+M ₆ | |
|--------------------------|------|------------------------------------|-----|--------------------------|-------|--------------------------|-------|--------------------------|-------|--------------------------|-------|
| Time | Q | Time | Q | Time | Q | Time | Q | Time | Q | Time | Q |
| h:min | l/s | h:min | l/s | h:min | l/s | h:min | l/s | h:min | l/s | h:min | l/s |
| 15:10 | 1.0 | - | - | 13:25 | 1.0 | 15:28 | 1.0 | 00:00 | 2.0 | 00:00 | 2.1 |
| 15:13 | 1.3 | | | 13:38 | 1.5 | 15:34 | 1.5 | 00:30 | 35.0 | 00:30 | 34.0 |
| | 0.0 | | | 13:45 | 2.5 | 15:38 | 3.0 | | 0.0 | | 0.0 |
| | | | | 13:48 | 3.5 | 15:42 | 4.0 | | | | |
| | | | | | 0.0 | 15:48 | 4.5 | | | | |
| | | | | | | | 0.0 | | | | |
| <i>D_{total}</i> | 3min | <i>D_{total}</i> | - | <i>D_{total}</i> | 23min | <i>D_{total}</i> | 20min | <i>D_{total}</i> | 30min | <i>D_{total}</i> | 30min |

D=overflow duration. Symbol "-" means that the experiment was not performed.

3.3.1. Preliminary study

The following tables (Table 21, Table 22 and Table 23) show predicted hydraulic parameters such as water thickness ($h_{w,p}$) and maximum shear stress ($\tau_{0,p}$) on the channel bottom. The predicted water thickness is estimated as function of the discharge set in flowmeter, rectangular channel width, channel slope gradient and Manning's n , applying the flow resistance equation of Manning and Strickler (through an iterative process) (Quintela, 1981):

$$Q_{flowmeter} = K \cdot (h_{w,p} \cdot B) \cdot \left(\frac{h_{w,p} \cdot B}{2h_{w,p} + B} \right)^{2/3} \cdot (\sin \beta_0)^{1/2} \quad (49)$$

where:

- $Q_{flowmeter}$ - discharge given by the flowmeter [m³/s],
- K - Strickler coefficient, $K=1/n$ [m^{1/3}/s] (Manning's n for the various sediments is shown in Table 12),
- $h_{w,p}$ - predicted waterflow thickness on the slope [m],
- B - channel width of the hydraulic model, $B=0.767$ [m].

Afterwards, the maximum shear stress $\tau_{0,p}$ (uniform flow conditions) is calculated according equation (13), using flow thickness $h_{w,p}$ calculated for each discharge $Q_{flowmeter}$. The goal of this calculation is to predict if sediment transport will happen under influence of different flow discharge values for each sample of granular material, using the critical

shear stress concept that establishes a threshold condition for the incipient motion of granular particles. The critical shear stress (or permissible shear stress) for granular, non-cohesive soil ($1.3 < D_{75} \text{ (mm)} < 50$) was estimated by the equation (50) function of D_{75} (grain size where 75% of the material is finer) (Kilgore and Cotton, 2005):

$$\tau_{c,soil} = 0.75D_{75} \quad (50)$$

This formula was used due to its simplicity and the values obtained are shown in Table 19.

Table 19. Estimation of critical shear stress according to equation (50).

| Gravel | D_{75} mm | $\tau_{c,soil}$ N/m ² |
|--------|----------------|-------------------------------------|
| s.A | 607 | 21.87 |
| s.B | 300 | 10.52 |
| s.C | 156 | 5.42 |

The value of critical shear stress was also calculated using the Shields parameter (Ψ_{cr}) (Table 20).

Table 20. Estimation of critical shear stress of gravel beds according to Shields.

| Gravel | D^* - | Ψ_{cr} - | $\tau_{b,cr}$ N/m ² |
|--------|------------|------------------|-----------------------------------|
| s.A | 607 | 0.06 | 23.56 |
| s.B | 300 | 0.06 | 10.59 |
| s.C | 156 | 0.05 | 4.78 |

Equation (50) was chosen rather than Shields' critical shear stress because it provided slightly lower values. Note that the evaluation of sediment motion was not influenced by critical shear stress calculation method.

The non-dimension grain size D^* was calculated by equation (25) for each gravel bed. Afterwards, the Shields parameter is estimated according to Figure 63 using D^* .

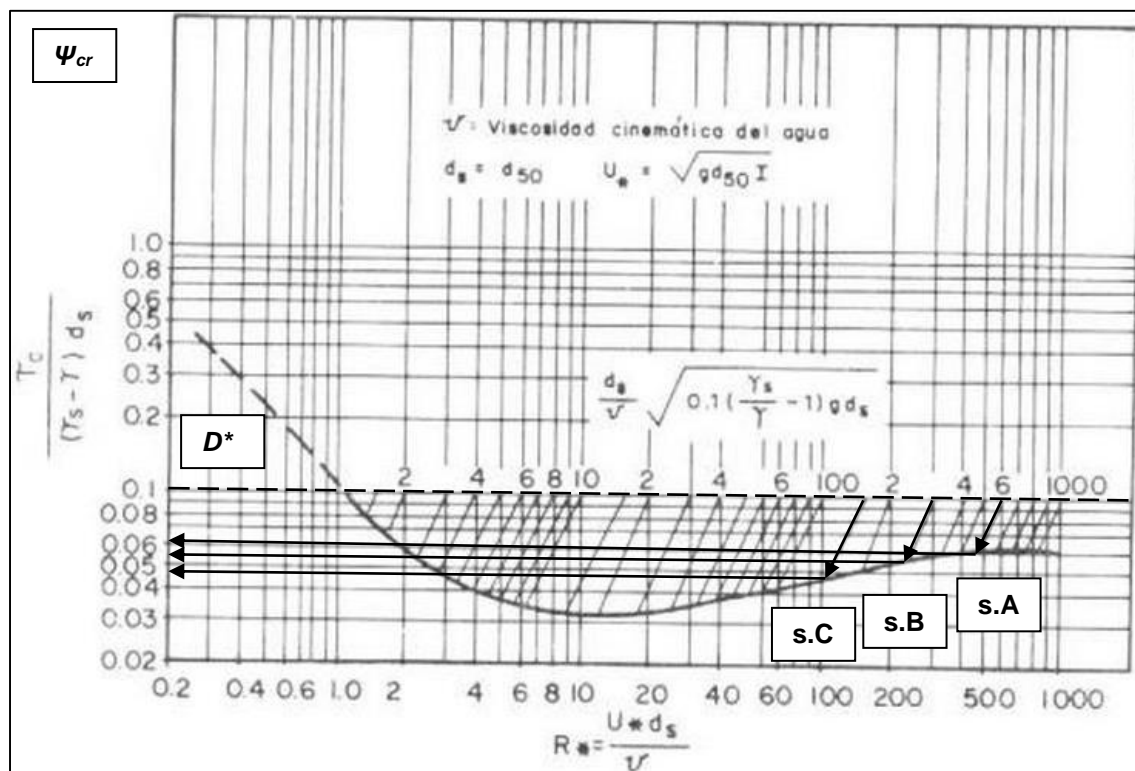


Figure 63. Shields diagram: estimation of shields parameter Ψ_{cr} for each gravel bed according to D^* (Quintela, 1981).

After extracting the Shields parameter from Figure 63 it is possible to calculate the critical shear stress for each type of gravel bed through application of equation (51).

$$\Psi_{cr} = \frac{\tau_{b,cr}}{(\rho_s - \rho_w)gD_{50}} \tag{51}$$

Table 21. Evaluation of sediment motion for gravel bed s.A for each discharge.

| Q l/s | $h_{w,p}$ cm | $\tau_{0,p}$ N/m² | $\tau_{b,cr}$ N/m² | $\tau_{c,soil}$ N/m² | SEDIMENT MOTION |
|------------------------|--|--|---|---|------------------------|
| 5.00 | 0.84 | 19.94 | 23.56 | 21.87 | NO |
| 7.50 | 1.07 | 25.50 | 23.56 | 21.87 | YES |
| 8.50 | 1.16 | 27.51 | 23.56 | 21.87 | YES |
| 9.00 | 1.20 | 28.48 | 23.56 | 21.87 | YES |
| 9.50 | 1.24 | 29.43 | 23.56 | 21.87 | YES |
| 10.00 | 1.28 | 30.36 | 23.56 | 21.87 | YES |
| 10.50 | 1.31 | 31.28 | 23.56 | 21.87 | YES |
| 11.50 | 1.39 | 33.06 | 23.56 | 21.87 | YES |

Table 22. Evaluation of sediment motion for gravel bed s.B for each discharge.

| Q l/s | $h_{w,p}$ cm | $T_{0,p}$ N/m² | $T_{b,cr}$ N/m² | $T_{c,soil}$ N/m² | SEDIMENT MOTION |
|------------------------|--|---|--|--|----------------------------|
| 2.10 | 0.46 | 11.01 | 10.59 | 10.52 | YES |
| 2.50 | 0.51 | 12.23 | 10.59 | 10.52 | YES |
| 3.00 | 0.57 | 13.65 | 10.59 | 10.52 | YES |
| 3.50 | 0.63 | 14.98 | 10.59 | 10.52 | YES |

Table 23. Evaluation of sediment motion for gravel bed s.C for each discharge.

| Q l/s | $h_{w,p}$ cm | $T_{0,p}$ N/m² | $T_{b,cr}$ N/m² | $T_{c,soil}$ N/m² | SEDIMENT MOTION |
|------------------------|--|---|--|--|----------------------------|
| 1.00 | 0.28 | 6.59 | 4.78 | 5.42 | YES |
| 1.30 | 0.32 | 7.72 | 4.78 | 5.42 | YES |

According to this preliminary study the granular bed material (of different grain sizes) will exhibit an unstable behaviour during the passage of overflowing water. Discharges superior to 5.0 l/s are expected to apply shear stresses at the bed layer bigger than the permissible shear stress for the granular surface s.A, thus causing sediment transport. For lower grain sizes (s.B and s.C) every discharge are expected to cause erosion with this channel slope inclination. Lower gravel beds with lower grain sizes are expected to be more susceptible to overflow erosion. Accordingly, a series of RECPs will be installed over the granular layers in order to assess if erosion can be avoided.

3.3.2. Test performance and observations

In this section a brief description of overtopping experiments will be done in order to give the reader a general overview of hydraulic model functionality and limitations, as well as gravel bed behaviour when facing hydraulic loading with and without a RECP by providing testing photographic documentation. Since the way waterflow removes and drags the particles along the downstream slope is very similar between the tests performed it is not pertinent to discuss every experiment realized.

Phase I, s.A (only)

In the beginning of the experiment water discharge, set by the valve and read in the electromagnetic flowmeter, was increased and gradually released over the downstream slope, which gives time to the sediments for moving and finding another equilibrium position along the slope. Every water discharge has to remain constant for a minimum time period of at least one minute, in order to observe particle behaviour carefully. With a starting discharge of 4.9 l/s it was noticed no sediment movement, thus bed layer resisted against dragging forces applied by flowing water. When it was submitted to a 7.5 l/s discharge value, the surface layer was stable during the testing period. It was observed random movement of individual particles which after a while (about 1 minute) were stationary again. These events were localized and did not happen along the entire boundary surface. A 10.0 l/s discharge imposed sediment transport along the slope by rolling and sliding of the granular particles (Figure 64, left side), which resulted in the formation of a breach channel over the granular bottom layer of the hydraulic model (Figure 64, right side). The gravel was gradually washed-out by the waterflow and the foundation layer was exposed and hence, the experiment was stopped (the threshold discharge Q_3 was attained). In another words, the release of water created a gully on the slope's model. Almost the whole amount of outflow was being discharged through this gully with increased flow velocity. If the water discharge was increased beyond 10.0 l/s the breach would widens and the entire model bed layer would have been removed.



Figure 64. Formation of breach channel through the slope's granular revetment.

Phase I, s.A+M₁:

For 5.1, 7.5 and 10.0 l/s discharges the behaviour of the superficial layer above the RECP M₁ (Figure 65) was nearly the same as the previously tested granular layer s.A (without the mat), which suggests that the mat does not have influence in top layer's stability. Accordingly it was also noticed that with a 10.0 l/s discharge (Q₁) the superficial granular material was eroded by the waterflow creating a breach channel and exposing the underlying geogrid M₁. When increasing the discharge to 12.5 l/s another channel along the downstream slope was formed, parallel to the one that had been already created.

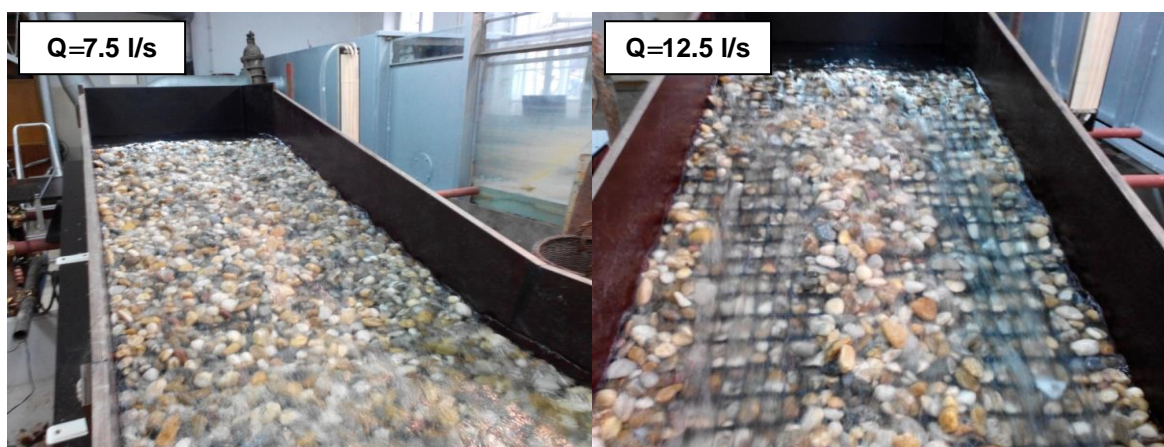


Figure 65. Breach formation process with RECP M₁ embedded in granular s.A.

The two breach channels continued to grow in lateral direction when the discharges were set to 15.0 l/s and 17.5 l/s. The sediments that were still resisting to waterflow shear forces remained next to the side-walls of the channel and in the middle of the bed slope, separating the two breach channels. When increasing the discharge value from 17.5 l/s to 20.0 l/s the remaining surface granular material was washed out, as expected. The sediments underneath the RECP M₁ also started to move a little along the slope but only readjusting their position. After the passage of a 25.0 l/s discharge the pump was stopped to obtain a better visualization of sediment/RECP state and understand their behaviour. It was concluded that some sediment motion occurred, although it was not sufficiently pronounced to provoke instability of the granular layer and consequent exposure of the foundation layer. Little sediment motion was proven by the changing in the mat's surface profile that was no longer completely straight (Figure 66, right-side picture). The mat exhibited a slightly wavy shape influenced by the location of the nails over the channel. This mat fixing points (anchors) did not allow pronounced vertical movement of the mat,

and hence, constituted an obstruction to sediment transport, creating areas with more concentration of material that pushed forward the geogrid. It was also observed that some individual particles moved through the apertures of the geogrid M_1 . After raising the discharge to 29.6 l/s ($Q_{max}=Q_2$) the underlying granular layer was not washed out by the overtopping event and dragged to model's horizontal platform. Despite the fact that some individual particles had been displaced (Figure 66) the mat M_1 proved to be capable of increasing underlying granular material stability by providing effective confinement of the gravel layer under greater overtopping water volumes. The reinforced lining is able to withstand (at least) 3 times more water discharge than granular layer alone.

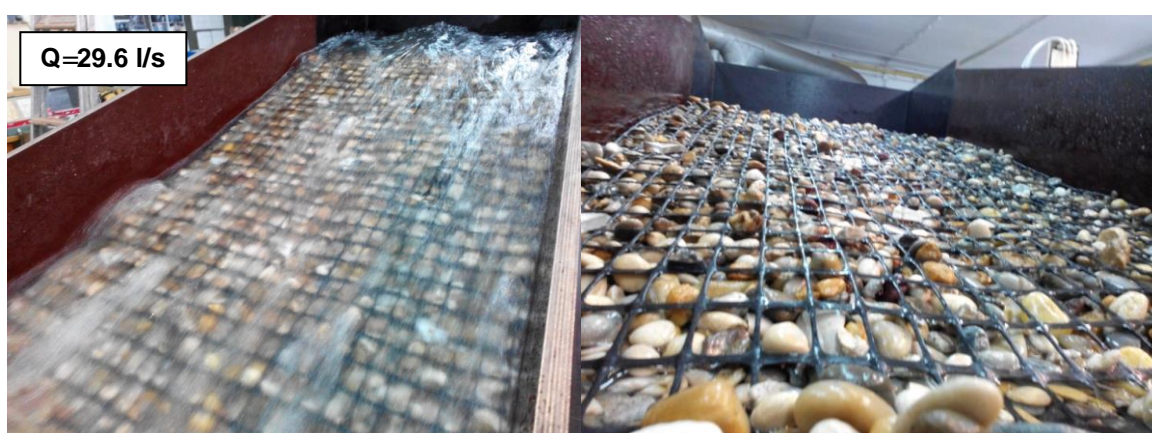


Figure 66. Reinforced gravel layer being submitted to a Q_{max} (on the left picture). RECP M_1 profile exhibiting a wavy shape after the passage of a 25.0 l/s flow discharge over it (on the right picture).

Phase I, s.A+M₂:

The apertures of the RECP M_2 do not allow for particle strike-through from one side to the other because they are sealed with a nonwoven geotextile which is firmly integrated between the geogrid bars. Therefore, the interlocking of the underlying and overlying granular layers within the apertures is expected to be reduced, comparing with RECP M_1 . The erosion flow pattern identified is similar to the one observed during the experiments referred above. The breach channel formation process (top granular layer) took place during the period where the discharge was increased from 9.0 l/s to 10.0 l/s (Figure 67). With 9.0 l/s discharge (Q_1), overlying particles moved downstream and created a localized point of erosion with exposure of the RECP M_2 in the upper part of the slope. After increasing to 9.5 l/s it was observed a small expansion in the lateral direction of the localized point of erosion. This erosion area continued to evolve longitudinally with a

10.0 l/s discharge, resulting into a quick formation of breach channel along the entire model's slope. This erosion pattern might be associated with earlier overtopping in a certain location along the crest width rather than others (hydraulic model crest profile might be uneven along its width), which causes preferential erosion due to locally higher velocities. Afterwards the experiment was stopped and the stability of gravel layer underneath the mat M_2 was not assessed under higher discharges (Q_{max}). The presence of geotextile between the geogrid bars did not benefit the visual inspection of the bottom layer conditions, so the threshold discharge Q_3 was not recorded.



Figure 67. Development of a breach channel above the RECP M_2 .

Phase II, s.B+ M_2

This testing was not successfully performed. The erosion of the top granular bed s.B took place during the period wherein the discharge (threshold discharge Q_1) is increased from 3.5 l/s to 4.0 l/s. A breach erosion channel formed next to model border due to concentrated flow (Figure 68).

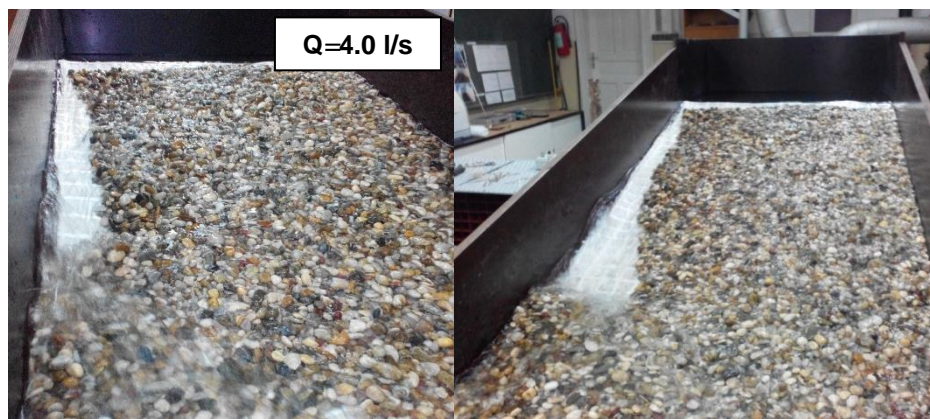


Figure 68. Erosion of top granular gravel layer s.C.

The threshold discharge Q_2 was attained with only 7.5 l/s because the RECP M_2 was detached from the underlying gravel bed in locations that were not anchored. This allowed a current to establish between the RECP and gravel bed s.C which cause direct erosion over the gravel. These currents underneath the mat developed due to the presence of geotextile between the geogrid bars, that created a surface with a certain impermeability, and insufficient anchoring that did not permit direct contact between the mat and gravel in every location (Figure 69).

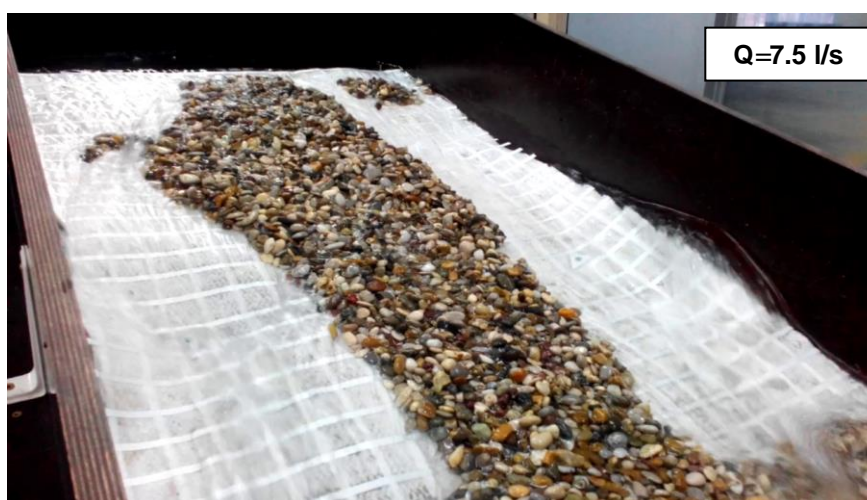


Figure 69. Gravel bed s.C being lift by underlying currents.

Phase I, s.A+M₃:

In order to increase the friction at geogrid-surface material interface and to have a clear view of underlying material behaviour it was decided to extract the nonwoven geotextile that was sealing the openings of the RECP M_2 . The erosion flow pattern observed was also similar to previous ones, with formation and growth of a breach channel over the overlying granular layer. The breach channel formation process took place during the period where the discharge was increased from 9.5 l/s to 11.5 l/s (Figure 70). As discharge value was being raised, granular material was being progressively washed out, until the moment where RECP M_3 was totally exposed by 20.0 l/s overtopping discharge. After being submitted to a maximum pump discharge of 35.6 l/s, the granular layer underneath the geogrid withstood. Therefore it can be concluded that the geogrid is able to provide enough blocking capacity against sediment movement towards sediment trap, for this specific discharge (Figure 71).

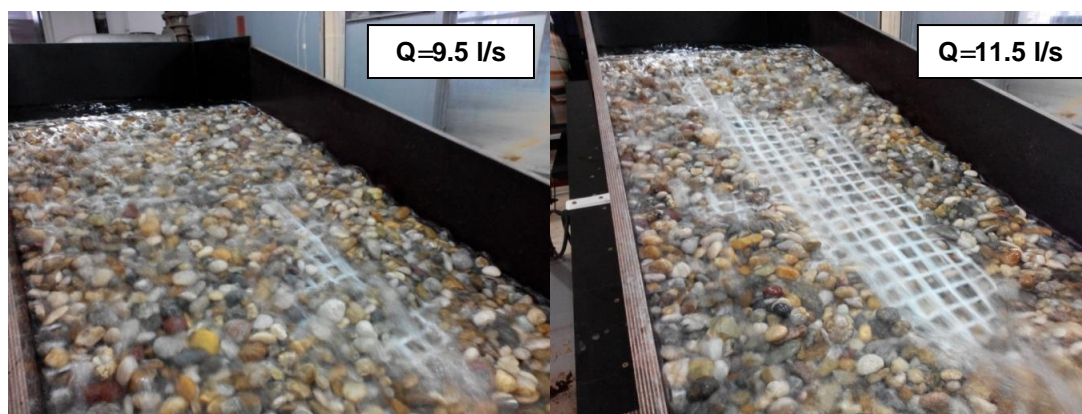


Figure 70. Development of a breach channel above the RECP M_3 .

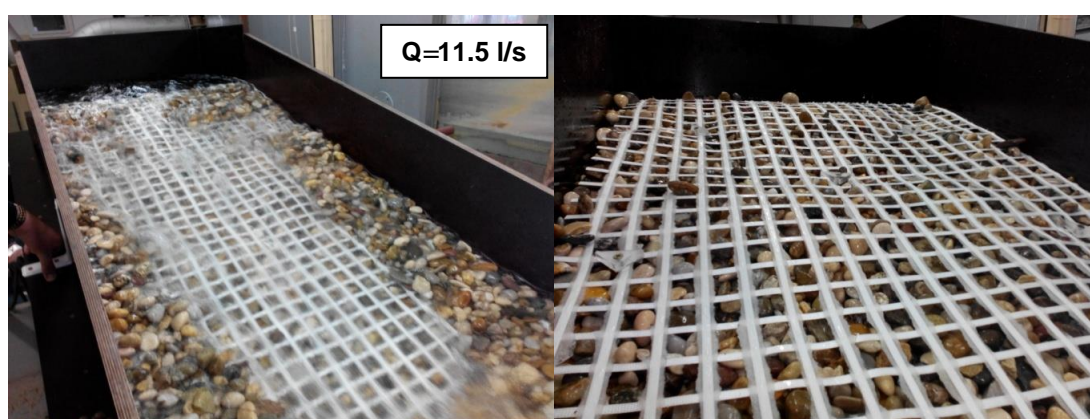


Figure 71. Removal of the sediments above the RECP M_3 by waterflow (on the left picture). Channel lining after the passage of Q_{max} (on the right picture).

Phase I, s.A+M₄:

RECP M_4 does not allow the passage of gravel particles s.A through the apertures. This net is more malleable, showing less stiffness than the other RECPs. Unfortunately, the manufacture is not known as well as its strength properties and material composition. This material was only tested to check if a smaller aperture size of the mat could influence the stability of underlying layers with lower grain sizes. The erosion process assumed the same behaviour as the other tested cases, with creation of a breach channel that widens in proportion with an increasing discharge. The breach formation took place during the period where the discharge is increased from 9.5 to 11.0 l/s (Figure 72).

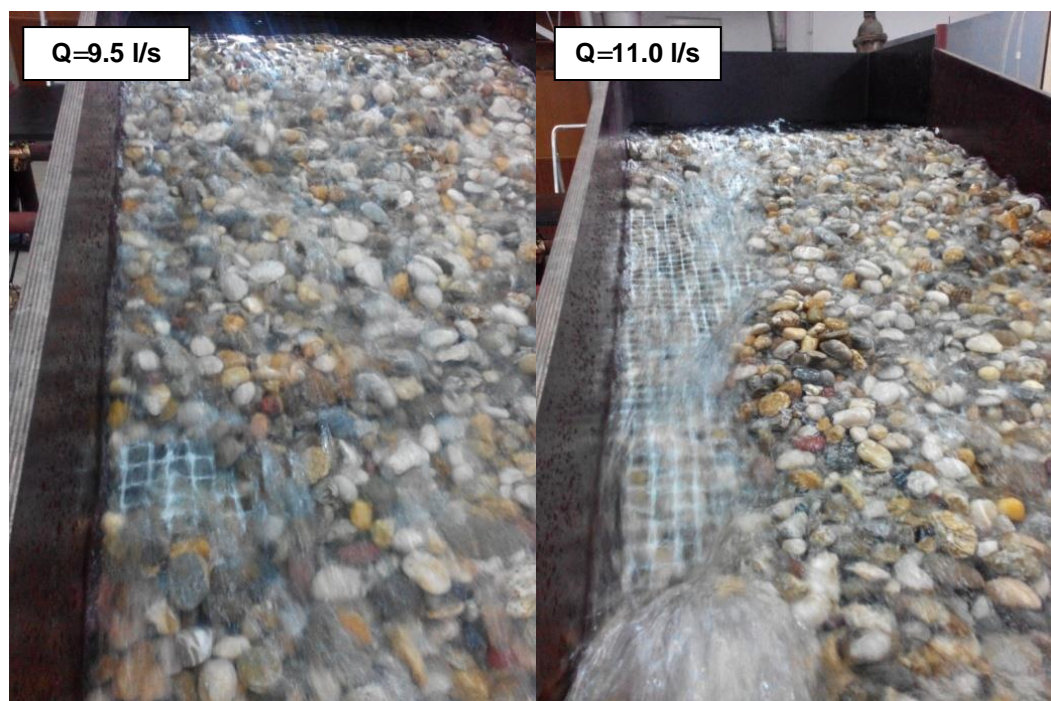


Figure 72. Development of a breach channel above the RECP M₄.

With a 33.5 l/s (maximum pump discharge) the granular layer under the mat was affected, being noticed pronounced sediment transport that uncovered the foundation layer in some areas. After the passage of this amount of discharge over the RECP M₄ the bottom granular layer became irregular and the mat was unable to stay in direct contact with the subgrade material (Figure 73).



Figure 73. Bed channel being submitted to Q_{max} (on the left picture). Bed channel configuration after overtopping event has been ended (on the right picture).

The mat did not withstand the shear stress submitted by the waterflow due to its reduced stiffness and high flexibility comparing with the others RECPs. Nevertheless, the value of

Q_{max} recorded is not characteristic from the moment where incipient motion of the underlying particles begins. The discharge was not increased in a progressive manner. In fact, the discharge was raised from 11.0 to 33.5 l/s which was not the correct procedure to find a threshold discharge value (Q_2).

Phase III, s.C+M₅:

For this test the RECP used is a composite turf reinforcement mat (C-TRM) which presents a more complex structure comparing with the geogrids tested before, namely a coconut fiber matrix incorporated into permanent three-dimensional turf reinforcement matting.

Following the procedure described earlier, the discharge was slowly increased and released over the hydraulic model's downstream slope until the time where erosion occurs. In this case, the erosion of the covering granular layer s.C began when the water discharge was 2.0 l/s (Figure 74). The discharge value was increased progressively till 35.0 l/s. The entire overlying granular layer was washed out but the RECP M₅ provided stability to granular material below it, avoiding sediment motion (Figure 74).



Figure 74. Initiation of the erosion process at the gravel top layer (beneath the TRM M₅) (on the left picture). Bed channel configuration after the overtopping event has ended, *i.e.*, after Q_{max} (on the right picture).

The experimental testing combining RECP M₅ with higher grain sizes was not done, since the presence of a granular layer with smallest grain size (s.C) was considered the worst case scenario in terms of stability due to its reduced weight.

Phase III, s.C+M₆.

For this test the RECP used is another type C-TRM, technologically more sophisticated than RECP M₅, consisting of a polypropylene fiber matrix incorporated into permanent three-dimensional turf reinforcement matting.

The test was performed the same way as the others. In this situation the erosion process of the top granular layer begins with 2.1 l/s. Afterwards, when this sacrificial layer had already been completely eroded, the maximum pump discharge (Q_{max}) of 34.0 l/s was attained and RECP M₆ did not yield, avoiding sediment movement of the underlying particles s.C (Figure 75).

As expected turf reinforcement mats presented the best erosion protection performance for the most potential unstable bottom layer (s.C), despite not being originally created for this type of unvegetated conditions and soil type (soil without cohesiveness).

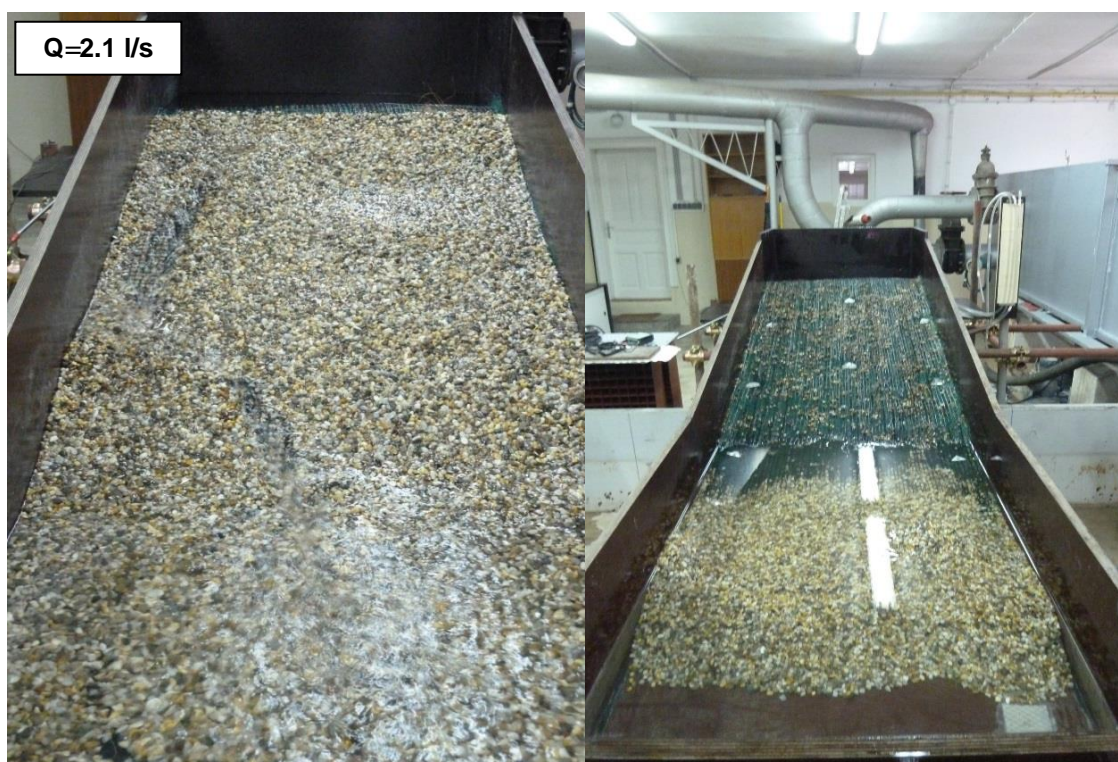


Figure 75. Initiation of the erosion process at the gravel top layer (beneath the TRM M₆) (on the left picture). Bed channel configuration after the overtopping event has ended, *i.e.*, after Q_{max} (on the right picture).

3.3.3. Data collected and observations

The principal data typically used to determine the erosion performance of a selected RECP product includes average soil loss (converted into CSLI) and the associated hydraulic shear stress calculated from flow thickness and mean flow velocity measurements (ASTM D6460 in Sprague, 2011). According to Kilgore and Cotton (2005) these hydraulic properties must be determined by full scale testing in laboratory channels using defined testing standard ASTM D6460.

Time series of hydrostatic flow thickness (perpendicular to slope) can be obtained by using measuring apparatus such as pressure gauges, point gauges or acoustic range finders. Measurement station intervals should be defined along the centreline of the flume where bed elevations are also recorded (to estimate soil loss depths), prior to the testing (Amini and Li, 2012 and Hughes *et al.*, 2012).

Time series of flow velocity (slope-parallel) can be estimated with devices such as Laser Doppler velocimeters (LDVs) and current meters (used in this experiment) (Hughes *e al.*, 2011). At least two downslope locations of velocity measurement (positioned at two flow depth measurement locations on the slope), correspondent to a fraction of the overall flow thickness (for example $0.4h_w$) should be guaranteed to evaluate eventual flow accelerations along the slope for a certain unit discharge. Note that equation (13) will typically estimate shear stresses higher than flows with the same discharge in which acceleration is still occurring. Flow thickness and velocity are function of distance down the landside slope until uniform flow conditions are reached for all values (average velocity will increase whereas flow thickness will decrease between two landside slope locations) (Hughes *et al.*, 2012).

Unlike flow thickness and velocity, instantaneous steady overflow discharge is conserved along the slope. The assumption of instantaneous discharge continuity allows to measure the discharge at the dike crest, where measurements are less difficult to perform and then transpose the values to the landside slope. The discharge at a certain measuring section (at the crest or landside slope) can be estimated as the product of mean horizontal velocity and normal flow thickness (Hughes *et al.*, 2011). By adopting this calculation procedure it is being assumed that flow velocity is constant throughout the water column at each location, which despite being a generally accepted assumption, it is not “hydraulically” true (section 2.3.3). In order to obtain the average flow velocity, velocity has to be measured at

certain depth of the water column, *i.e.*, at distance correspondent to $0.37h_w$ from the bed channel (CIRIA *et al.*, 2013).

Threshold performance discharges

Table 24 provides the measured performance values of threshold discharge Q_1 (or unit discharge q_1) for each phase of the experimental program (s.A, s.B or s.C).

Table 24. Values of the discharge measured when sediment motion begins to occur, associated with the granular top layer over the RECP. Part one of the experiments.

| | Q_1 l/s | q_1 l/s/m | Q_1 l/s | q_1 l/s/m | Q_1 l/s | q_1 l/s/m |
|----------------|--------------|----------------|--------------|----------------|--------------|----------------|
| RECP | s.A | | s.B | | s.C | |
| M ₁ | 10.1 | 13.2 | 3.0 | 3.9 | - | - |
| M ₂ | 9.0 | 11.7 | 3.5 | 4.6 | 1.5 | 2.0 |
| M ₃ | 9.5 | 12.4 | 3.5 | 4.6 | - | - |
| M ₄ | 9.5 | 12.4 | 3.0 | 3.9 | 1.5 | 2.0 |
| M ₅ | - | - | - | - | 2.0 | 2.6 |
| M ₆ | - | - | - | - | 2.1 | 2.7 |

Symbol “-“ means that the experiment was not performed.

Kilgore and Cotton (2005) stated that the erodibility of coarse non-cohesive soils was due to mainly particle grain size. As expected, the stability of the granular bottom layer decreased when using smaller grain size particles in its constitution. Accordingly, threshold discharge Q_3 is higher for higher grain sizes, which means that material s.A can withstand greater discharges without pronounced erosion (less than 10.0 l/s) than material s.B and s.C that only can stand residual discharges (Table 26). Material s.B and s.C are clearly not appropriate materials for handling overtopping discharges due to its reduced dimensions and weight. These results confirmed that gravel beds are not suitable for placement in steep channels slope. An explanation for this observation is that the gravel particles do not interlock due to its smooth and rounded shape. The sediment movement predictions (made in section 3.3.1) corroborated with the behaviour exhibited by the granular layer during the overtopping experiment generally, despite having overestimated the incipient motion of gravel s.A that stood still with discharge values around 9.0 l/s for a certain overflow duration.

Table 25 exhibits the measured performance values associated with threshold discharge Q_2 (or unit discharge q_2) for the several experiments performed.

Note the hydraulic model have limited capacity of what can be discharged on the test section ($Q_{max} \approx 29-36$ l/s). This value of Q_{max} have been reached in four cases (Table 25). Consequently the testing had to be stopped without the model's channel surface had experienced any pronounced particle movement that hindered layer stability. As expected, every mat tested sustained the damage (from stretching and ripping) inflicted by the overflow and maintained its structural integrity.

Table 25. Values of the discharge measured when sediment motion occurs beneath the mats. Part two of the experiments.

| | Q_2 l/s | q_2 l/s/m | Q_2 l/s | q_2 l/s/m | Q_2 l/s | q_2 l/s/m |
|----------------|------------------------|----------------|------------------------|----------------|----------------------|----------------|
| RECP | s.A | | s.B | | s.C | |
| M ₁ | stable ¹⁾ | - | 22.0 | 28.7 | - | - |
| M ₂ | - | - | unstable ⁴⁾ | - | 3.5 | 4.6 |
| M ₃ | stable ²⁾ | - | 22.5 | 29.3 | - | - |
| M ₄ | unstable ³⁾ | - | 10.0 | 13.0 | 4.5 | 5.9 |
| M ₅ | - | - | - | - | stable ⁵⁾ | - |
| M ₆ | - | - | - | - | stable ⁶⁾ | - |

1) $Q_{max}=29.6$ l/s / 38.6 l/s/m; 2) $Q_{max}=35.6$ l/s / 45.4 l/s/m; 3) The test was not well performed but unstable with $Q_{max}=33.5$ l/s / 43.7 l/s/m; 4) The test was not well performed but unstable with $Q=7.5$ l/s / 9.8 l/s/m; 5) $Q_{max}=35.0$ l/s / 45.6 l/s/m; 6) $Q_{max}=34.0$ l/s / 44.3 l/s/m; Symbol '-' means that the experiment was not performed.

Table 26 shows the threshold discharge values Q_3 (or unit discharge q_3) measured during the overtopping events and compares it with threshold discharge values Q_2 , in order to give the reader the influence of RECP in the underlying granular layer.

After analysing Table 26 it can be inferred that generally granular material (s.A, s.B and s.C) in conjunction with an overlying protection mat presents a better stability performance than the granular material alone, withstanding higher values of discharge water volumes without catastrophic sediment motion beneath it.

Table 26. Values of the discharge measured when sediment motion occurs during part three of the experiment and comparison with thresholds values of part two.

| Gravel | s.A | | s.B | | s.C | |
|----------------|-------------------|-------------------|--------------|----------------|-------------------|-------------------|
| no RECP | Q_3 l/s | q_3 l/s/m | Q_3 l/s | q_3 l/s/m | Q_3 l/s | q_3 l/s/m |
| | 10.0 | 13.0 | 2.5 | 3.3 | 1.0 | 1.3 |
| RECP | Q_2 l/s | q_2 l/s/m | Q_2 l/s | q_2 l/s/m | Q_2 l/s | q_2 l/s/m |
| M ₁ | 29.6 ⁺ | 38.6 ⁺ | 22.0 | 28.7 | - | - |
| M ₂ | - | - | - | - | 3.5 | 4.6 |
| M ₃ | 35.6 ⁺ | 46.4 ⁺ | 22.5 | 29.3 | - | - |
| M ₄ | - | - | 10.0 | 13.0 | 4.5 | 5.9 |
| M ₅ | - | - | - | - | 35.0 ⁺ | 45.6 ⁺ |
| M ₆ | - | - | - | - | 34.0 ⁺ | 44.3 ⁺ |

"+" means that $Q_2 \gg Q_{max}$.

Mats M₁ and M₃ provided effective confinement of material s.A by increasing the amount of bearable discharge considerably, at least three times more than without any geogrid reinforcement. Thus, the threshold discharge Q_2 was not reached, keeping the gravel locked in place. With regard to material s.B, mats M₁ and M₃ were not so successful in providing bottom layer stability comparing with the case of material s.A, because the threshold discharge Q_3 was attained for only 23.0 l/s, approximately. As the geogrid M₁ was not able to avoid the threshold discharge Q_2 for gravel bed s.B, an even more unstable behaviour was predicted for gravel bed s.C due to its lower grain size. Therefore, the testing combining RECP M₁ with gravel bed s.C was not realized. Mats M₂ and M₄ were not capable of providing any confinement of the granular layer s.C due to its physical characteristics, and hence were not suitable for reinforcing this reduced grain-sized layer. As the particles s:C could pass through the apertures of the mats, maybe if their aperture were smaller it would have been possible to stabilize the granular layer s.C. However, when using the granular material s.C (more prone to be displaced) reinforced with turf reinforcement mats M₅ and M₆, stability improvements of the erodible bed were remarkable, holding up a waterflow discharge at least 35 times greater than the discharge bearable without the mats. Since these mats were successfully tested over the most unstable gravel bed (s.C) in terms of control of underlying sediment motion, it was not necessary to perform the testing with the other gravel beds with higher grain sizes

(the greater the grain size value of gravel beds, the greater the value of threshold discharge Q_2). The surface protection system M_5 and M_6 presented the best performance result amongst the RECPs because they were the only RECPs capable of stabilizing the gravel bed s.C (most severe scenario). Accordingly this mats were considered the most adequate solution to provide erosion control and contribute to layer stability amongst the RECP tested.

Measurement of velocity and flow thickness

The waterflow velocity and thickness measurements took place only in phase I with granular material s.A and RECP M_1 (Table 16) at a cross-section location near the downward edge of the slope, (Figure 46). At least one more measurement location should have been established near the crest of the hydraulic model as stated before.

The calculated values are unlikely to be representative of the cross-sectional average flow velocity due to constraints that arose from the flow conditions during the measurement process, including: (a) insufficient flow thickness; (b) presence of flow turbulence; and (c) variable velocities over the cross-section A.

The hydraulic model was not designed in a way that a considerable upstream overflow elevation (or surge elevation) could be created in order to release a waterflow with sufficient thickness to submerge the velocimeter completely (especially for discharges lower than 25-30 l/s approximately) and thus obtain reliable data from it (Figure 76).



Figure 76. Measurement of velocity with an unsubmerged velocimeter.

As the flow was quite thin the tip of velocimeter was closer to upper limit of the flow thickness or even slightly above it. The distance between the measuring device and the bed channel, corresponding to a certain percentage of flow thickness, was not possible to estimate in order to determine the mean flow velocity (the velocity varies along the water column). In addition, for lower discharges some of the particles composing the top layer above the RECP were not submerged, which eliminated the possibility of measuring accurately both flow thickness and velocity values.

Besides water thickness being very small over the channel slope, the outflow presented some turbulence imposed by the size and shape of the gravel particles s.A in conjunction with the mat M₁. As the supercritical discharge flows down the landside slope, the downward momentum is resisted by friction due to slope surface roughness, and a turbulent boundary layer is formed. After the removal of granular top layer by the waterflow (this layer is always washed out in every experiment) the presence of the RECP over the bottom gravel layer reduced flow turbulence because the surface became smoother. Figure 77 allows to visualise the effect that protection cover's roughness has on the discharge in terms of turbulence.



Figure 77. Flowing water exhibiting turbulence ($Q_{max}=29.6$ l/s).

This behaviour was observed mainly in the vicinity of the slope's toe/sediment trap (next to cross-section A) where there was great concentration of dragged material that has been

washed out from the slope surface. When flowing water collided with an aggregation of particles a water jet was created and this phenomenon repeated along the uneven slope's surface profile (Figure 78). Consequently, the water depth varied a lot for a particular model's channel cross-section when gravel material was still laying down on the slope. During this phase of the erosion process, locally higher velocity could be perceived due to concentrated flow on the breach channels that have been created through the granular top layer (Figure 78). In this case the velocity is expected to be higher than a situation where top layer would have been completely washed away.



Figure 78. Waterflow depth profile (on the left picture) and water jet created due to irregularity of the surface granular layer (on the right picture).

Other aspect observed during the experiment was the entrainment of air into the flowing water that increases the overall flow thickness and also increases the complexity of the velocity/flow thickness measurement procedure.

The constraints presented above have made measurement procedure of flow thickness highly inaccurate and velocity readings possibly invalid. The problem related to mean velocity measurements at the slope could have been side-tracked if accurate flow thickness readings were obtained, by dividing the unit discharge (given by the flowmeter) by the normal flow thickness at a channel cross-section.

The following table summarizes the data collected by the velocimeter, which includes the measured number of propeller revolutions in a 20 seconds interval (R_i) and average flow velocity calculated through application of equation (48). It also contains the range of flow thickness values ($h_{w,min}$ and $h_{w,max}$) for a particular unit discharge ($q_{flowmeter}$), measured with an ordinary ruler normal to the slope of the hydraulic model. Note that all the readings

were taken in the same cross-section over the channel bed. It can be seen in Table 27 that flow depth measurements with a ruler were not able to provide data with accuracy, demonstrating the inherent limitations and inappropriateness of this device for data collection.

Table 27. Data collection: discharge values set in flowmeter; data log collected with the velocimeter; and order of magnitude of flow thickness.

| $Q_{flowmeter}$ | $q_{flowmeter}$ | Impulses read in signal counter | | N | $U_{velocimeter}$ | Flow thickness | |
|-----------------|---------------------|---------------------------------|-------|---------|--------------------|-------------------------------|-----|
| | | R_1 | R_2 | | | $h_{w,min} < h_w < h_{w,max}$ | cm |
| l/s | m ³ /s/m | | | Rev/sec | m/s | | |
| 5.1 | 0.007 | - | - | - | - | 0.5 | 1.0 |
| 7.5 | 0.010 | - | - | - | - | 0.5 | 1.0 |
| 10.0 | 0.013 | - | - | - | - | 1.0 | 1.5 |
| 12.5 | 0.016 | - | - | - | - | 1.0 | 1.5 |
| 15.0 | 0.020 | 252 | 255 | 12.68 | 1.32 | 1.5 | 2.0 |
| 17.5 | 0.023 | - | 256 | 12.80 | 1.34 | 1.5 | 2.0 |
| 20.0 | 0.026 | - | 258 | 12.90 | 1.35 | 1.5 | 2.0 |
| 22.5 | 0.029 | - | 294 | 14.70 | 1.53 | 2.5 | 3.0 |
| 25.0 | 0.033 | 287 | 278 | 14.13 | 1.47 | 2.5 | 3.0 |
| 29.6 | 0.039 | 300 | 290 | 14.75 | 1.54 | 2.5 | 3.0 |
| 35.0 | 0.046 | - | 387 | 19.37 | 2.01 ¹⁾ | - | - |

Symbol “-“ means that the measurement was not performed. Test duration: 51min (Phase I: bed layer: s.A+M₁). 1) Velocity value obtained over the RECP M₅, i.e., bed layer: s.C+M₅.

3.4.Data analysis and results

Table 28 presents a series of hydraulic parameters calculated from the data collected including: unit discharges q_{min} and q_{max} (obtained from the product of measured velocity $U_{velocimeter}$ and measured flow thickness $h_{w,min}$ and $h_{w,max}$); Manning’s roughness n_{min} and n_{max} (calculated using the calculated unit discharge and the measured average flow velocity); and maximum bed shear stress $\tau_{b,min}$ and $\tau_{b,max}$ (calculated with the flow thickness measurements and assuming that the flow has reached terminal velocity).

Table 28. Testing results calculated from de data collected from the experiments.

| Data collected | | | | Testing results | | | | | |
|-----------------|-------------------|-------------|-------------|-----------------|-----------|-------------|-------------|-------------|-------------|
| $q_{flowmeter}$ | $U_{velocimeter}$ | $h_{w.min}$ | $h_{w.max}$ | q_{min} | q_{max} | n_{min} | n_{max} | $T_{b.min}$ | $T_{b.max}$ |
| $m^3/s/m$ | m/s | m | m | m^2/s | m^2/s | $s/m^{1/3}$ | $s/m^{1/3}$ | N/m^2 | N/m^2 |
| 0.020 | 1.323 | 0.015 | 0.020 | 0.020 | 0.026 | 0.023 | 0.027 | 35.689 | 47.585 |
| 0.023 | 1.336 | 0.015 | 0.020 | 0.020 | 0.027 | 0.022 | 0.027 | 35.689 | 47.585 |
| 0.026 | 1.346 | 0.015 | 0.020 | 0.020 | 0.027 | 0.022 | 0.027 | 35.689 | 47.585 |
| 0.029 | 1.531 | 0.025 | 0.030 | 0.038 | 0.046 | 0.028 | 0.031 | 59.481 | 71.378 |
| 0.033 | 1.472 | 0.025 | 0.030 | 0.037 | 0.044 | 0.029 | 0.032 | 59.481 | 71.378 |
| 0.039 | 1.536 | 0.025 | 0.030 | 0.038 | 0.046 | 0.027 | 0.031 | 59.481 | 71.378 |

Measured unit discharges vs estimated unit discharges

The calculated unit discharges (q_{min} and q_{max}) do not have into account the amount of water that runs through the foundation layer and gravel layers and assume that flow velocity has a constant value along the flow thickness. Comparing the discharges measured by the flowmeter with the ones estimated as the product of flow thickness and mean velocity it can be perceived that some values of $q_{flowmeter}$ did not fit in the range of values defined by q_{min} and q_{max} . It was expected that the estimated unit discharges were inferior to the ones given by the flowmeter since its calculation only considered the water column above the lining. An explanation may be related with inaccurate flow depth measurements that provided overestimated readings and thus, overestimated unit discharges.

Estimated Manning's n

Manning's n was calculated according equation (18), even though terminal velocity may not have been attained on the hydraulic model channel. Non-uniform flow conditions provide values of flow velocity inferior to the ones provided when uniform flow is attained over the slope (for the same discharge), which implies lower Manning's n values when using equation (18). Manning's n was not constant during an overflow experiment and it varied with increasing flow thickness due to increasing overflow discharge, as demonstrated in Figure 79. The graph includes also the best regression line fit to the test data. Hughes *et al.* (2011) presented a similar plot where the Manning's n increased with higher flow thicknesses at certain slope cross-section, as shown in Figure 80. However, Manning's n in Figure 80 are correspondent to higher ranges of flow thickness than the ones found during the present overflow experiments.

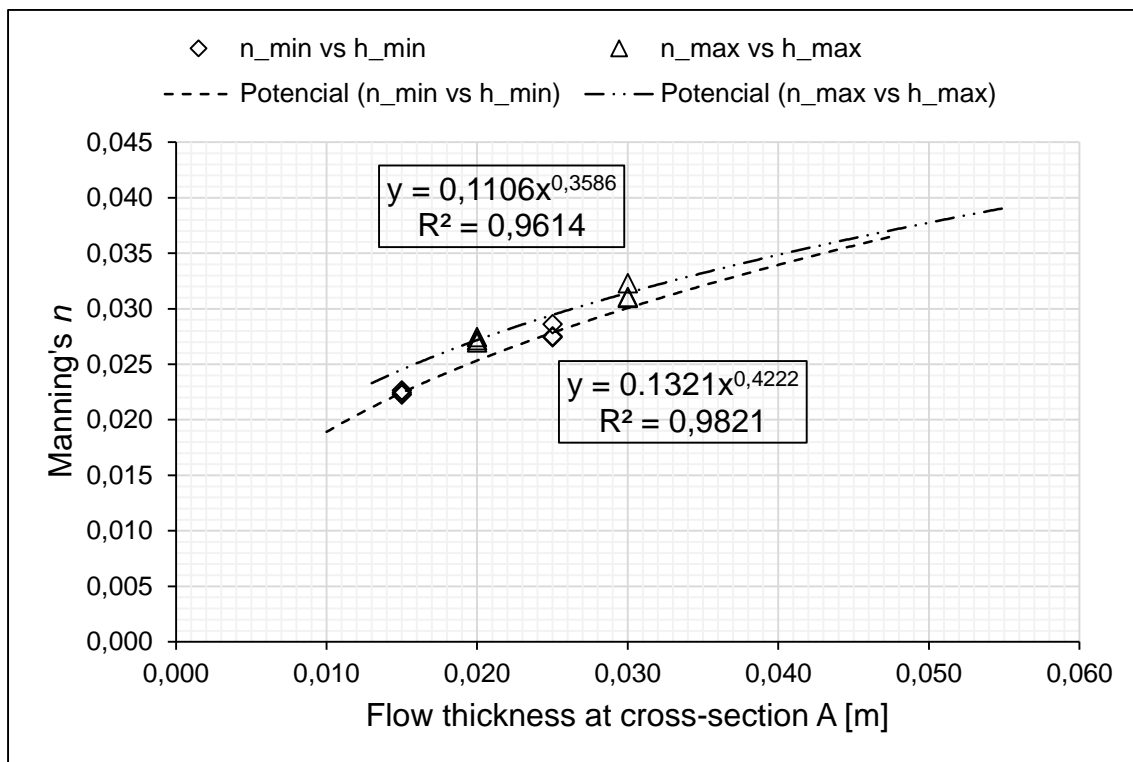


Figure 79. Estimated values of Manning's n at cross-section A.

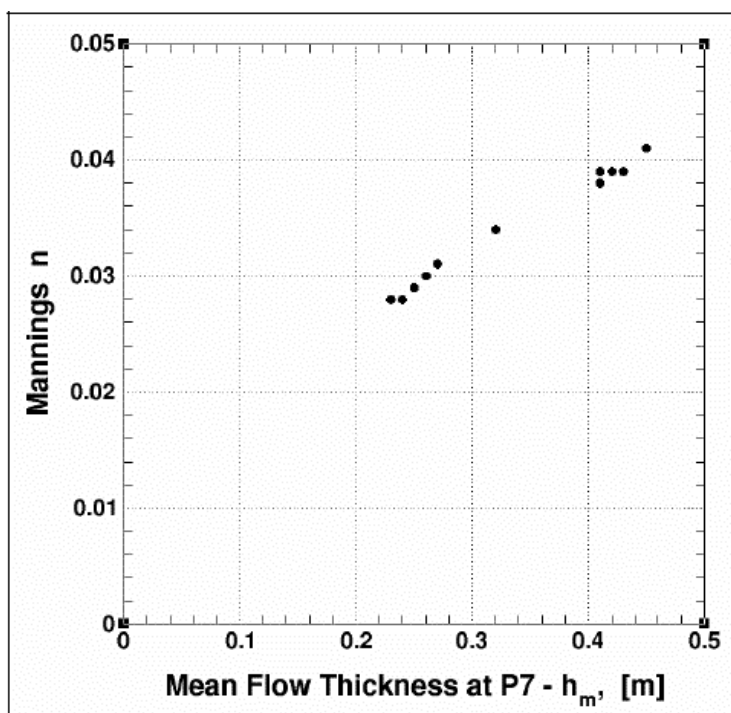


Figure 80. Manning's n versus flow thickness (Hughes *et al.*, 2011).

Estimated shear stress

Bed shear stress was only possible to be estimated through equation (21) because only one cross-sectional measurement location was defined. It was assumed that $R=h_w$ (for channels that are very wide in comparison to waterflow depth) and that the flow has reached a terminal flow velocity with a constant flow thickness. Especially for higher discharges ($Q>15.0$ l/s), slope length may be not long enough to allow the establishment of uniform flow conditions. In that case flow is still accelerating and equation (14) is more appropriate for estimation of mean shear stress over a determined length between the two measurement locations at the landside slope. Accordingly, shear stress values presented in Table 28 are probably conservative estimates that are larger than what would be calculated under the same flow conditions where the slope is long enough to allow terminal velocity (since the terminal flow thickness would be smaller than the “measured” flow thickness).

Empirical correlations

The same empirical correlations established by (Hughes *et al.*, 2012) (equation (16)) were calculated using shear stress values ($\tau_{b,min}$ and $\tau_{b,max}$) (at one cross-section station only) and unit discharges (q_{min} and q_{max}) presented in Table 28 and plotted in Figure 81. The graph includes the two best regression line fit to the test data.

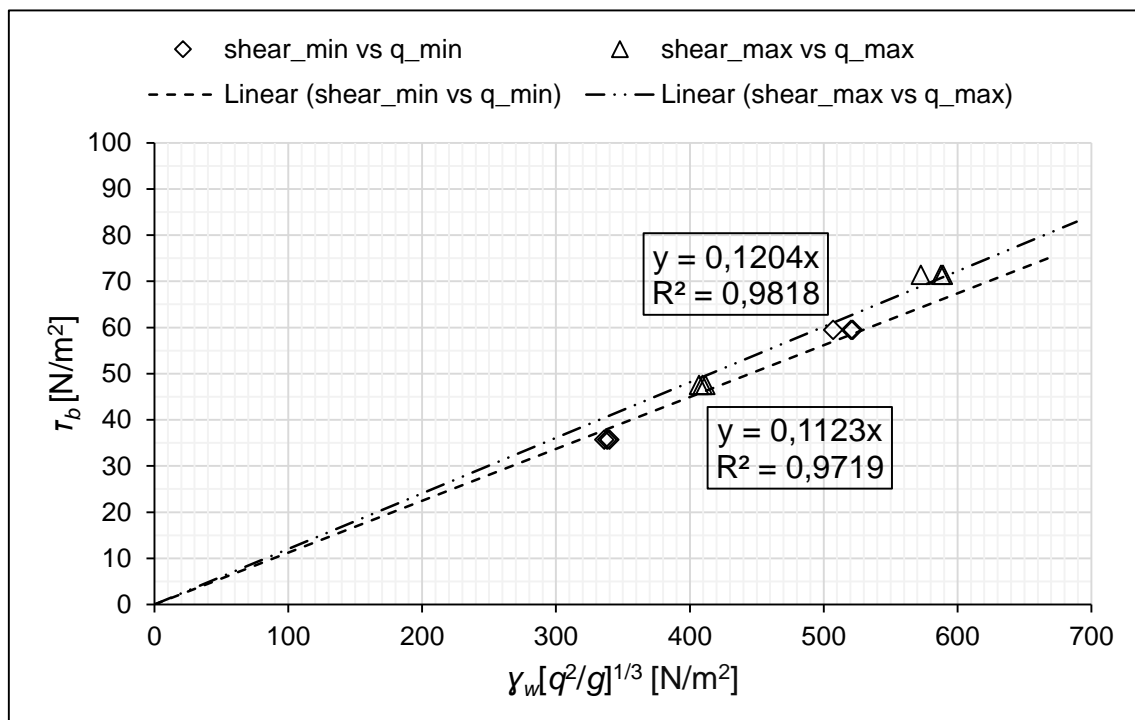


Figure 81. Unit discharge parameter versus shear stress on the lining (s.A+M₁).

Two best-fit equations can be extracted by the best regression line fit in Figure 81:

$$\tau_{b,\min} = 0.112 \cdot \gamma_w \left(\frac{q^2}{g} \right)^{\frac{1}{3}} \quad (52)$$

$$\tau_{b,\max} = 0.120 \cdot \gamma_w \left(\frac{q^2}{g} \right)^{\frac{1}{3}} \quad (53)$$

Together equation (52) and (53) provide a range of shear stress estimations for terminal flow velocity conditions as a function of the unit discharge over a slope with an inclination of 1V:4H and a surface roughness representative of the tested protection system (gravel s.A beneath geogrid M₁). Note that these equations provide rough estimations and hence caution is advised when making design considerations about them.

As expected, the coefficient of the predictive equation (16) presented in Figure 12, 0.106, was not equal to the two coefficients presented in Figure 81. This difference can be easily explained by the difference in the slope of landside face and roughness of surface layer between the Hughes *et al.* experiment and the experiment realized in the context of this dissertation. Also, concerning to Hughes *et al.* experiment, the shear stress was calculated with a shear stress equation that considers flow accelerations (equation (14)) and consequently is representative of an average shear stress over a distance at landside slope of higher magnitudes. Accordingly, each predictive equation is strictly valid only for the respective hydraulic model features. Furthermore, the coefficient differences may also be related to the lack of accuracy of the testing results.

Another empirical equation was evaluated for the range of tested parameters of the present experiment, the same way as Amini and Li (2012) did (section 2.8.3). It was intended to correlate flow thickness, through a hydraulic parameter dimensionally consistent, with unit steady discharge (Figure 82).

Two best-fit equations can be extracted by the best regression line fit in Figure 82:

$$\sqrt{gh_{w,\min}^3} = 0.3185 \cdot q \quad (54)$$

$$\sqrt{gh_{w,\max}^3} = 0.3516 \cdot q \quad (55)$$

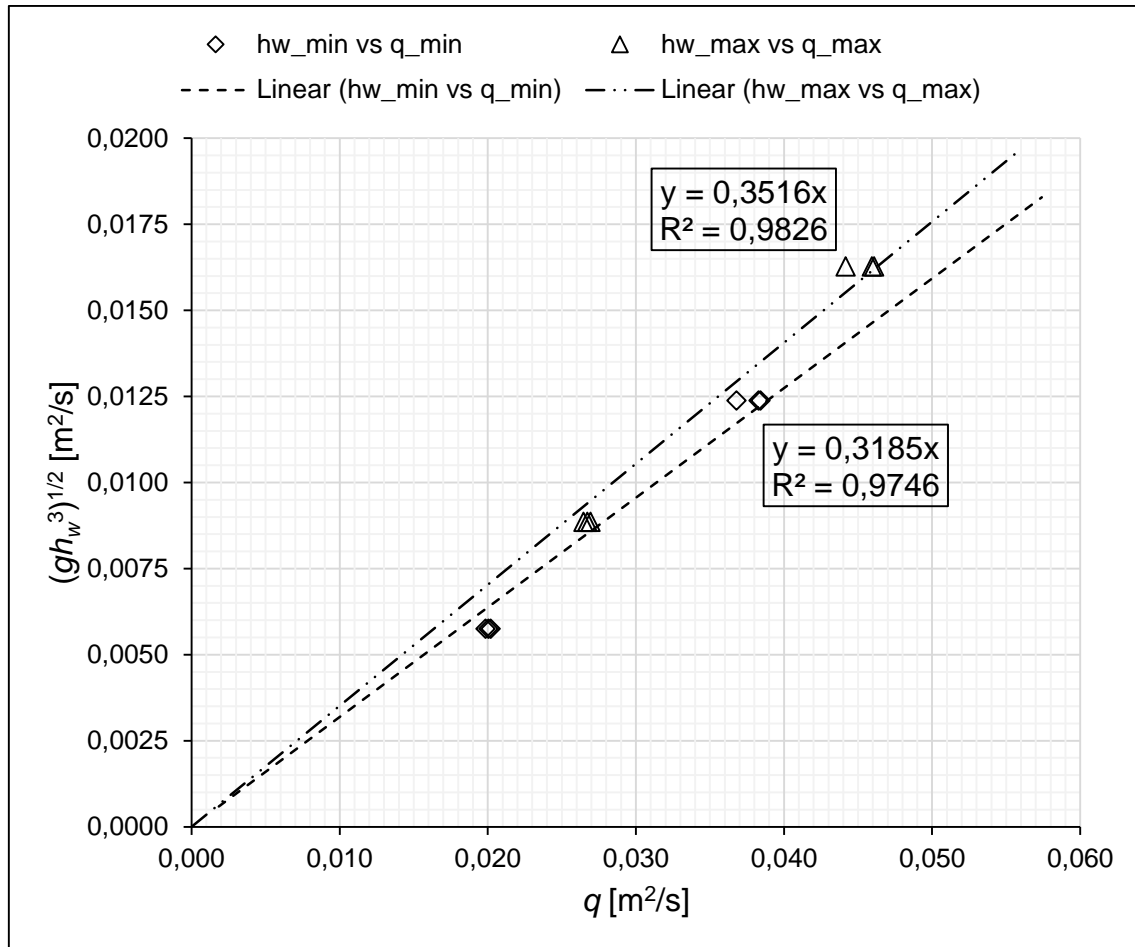


Figure 82. Overflow parameter that includes measured average flow thickness versus unit discharge (calculated through the measured velocity and flow thickness).

Together equation (54) and (55) provide a range of average flow thickness for terminal flow velocity conditions $[h_w=(y^2/g)^{1/3}]$, where $y_{min}=0.3185x$ or $y_{max}=0.3516x$ by setting an overflow parameter $[(g \cdot h_w^3)^{1/2}]$ as a function of the steady unit discharge (q) over the landside slope.

The two empirical best-fit coefficients obtained, 0.3185 and 0.3516, are naturally different to the one ($k_d=0.3076$) estimated by Amini and Li (2012) because it is representative of different protection channel lining composed of a vegetated HPTRM (Figure 42). As the two coefficients estimated are slightly higher than the one estimated by Amini and Li, for the same steady unit discharge, equations (54) and (55) will estimate higher flow thicknesses than equation (45). The differences in the estimation of flow thickness may be related with distinct Manning's roughness coefficient characteristic of each protection system. The manufacturer reported values of Manning's n range for the HPTRM, was 0.25-0.45, while for RECP M₁ the limitations of test facility only allowed to obtain

Manning's n in the range of 0.23-0.31. The HPTRM tested by Amini and Li (2012) also had a geogrid embedded in its structure, similar to RECP M₁ in terms of ultimate tensile strength (30.0 kN/m), but the presence of interlocked grass may have created a totally different surface roughness and consequently a different average Manning's n representative of tested hydraulic parameters. As equations (54) and (55) provide higher flow thickness the average Manning's n is expected to be higher than the one representative of HPTRM used by Amini and Li (if estimated for the same ranges of steady overflow unit discharge).

Measured flow velocity vs estimated mean flow velocity

As explained in section 2.3.3 the flow velocity assumes a logarithmic profile and consequently the maximum flow velocity is approximately reached at the surface boundary of the flow thickness and is zero at the stream bed.

In order to assess if the flowmeter velocity readings could be representative of mean flow velocity, equation (10) was calculated based on the measured values of flow thickness (Table 29). The methodology consisted of considering that the parameter z (m) was equal to a percentage of the flow thickness, $z=0.37h_w$, that corresponded in velocity profile $u(z)$ to the mean velocity U . The maximum velocity that corresponded to entire depth of the water column was also estimated, $u(z=h)^{min}$ and $u(z=h)^{max}$ (Table 29) (CIRIA *et al.*, 2013).

Table 29. Comparison between the measured mean flow velocity and mean velocity according equation (10).

| $q_{flowmeter}$ m ³ /s/m | $U_{velocimeter}$ m/s | u^*_{min} m/s | $u(z=0.37h)^{min}$ m/s | $u(z=h)^{min}$ m/s | u^*_{max} m/s | $u(z=0.37h)^{max}$ m/s | $u(z=h)^{max}$ m/s |
|--|--------------------------|--------------------|---------------------------|-----------------------|--------------------|---------------------------|-----------------------|
| 0.020 | 1.323 | 0.189 | 0.900 | 1.358 | 0.218 | 1.192 | 1.721 |
| 0.023 | 1.336 | 0.189 | 0.900 | 1.358 | 0.218 | 1.192 | 1.721 |
| 0.026 | 1.346 | 0.189 | 0.900 | 1.358 | 0.218 | 1.192 | 1.721 |
| 0.029 | 1.531 | 0.244 | 1.466 | 2.057 | 0.267 | 1.724 | 2.372 |
| 0.033 | 1.472 | 0.244 | 1.466 | 2.057 | 0.267 | 1.724 | 2.372 |
| 0.039 | 1.536 | 0.244 | 1.466 | 2.057 | 0.267 | 1.724 | 2.372 |

It was found that for the unit discharges $q_{flowmeter}=0.020$, 0.023 and 0.026 l/s/m the flow velocities measured with the flowmeter ($U_{velocimeter}$) were greater than the mean flow velocity estimated by equation (10) [$u(z)=(0.37h)^{min}$ and $u(z)=(0.37h)^{max}$].

For the remaining unit discharges $q_{\text{flowmeter}}=0.029$, 0.033 and 0.039 at Table 29, the $U_{\text{velocimeter}}$ was a value between the range of values provided by equation (10) and hence nearer to the mean velocity U . This discrepancy in the values of velocity was related with conditions during the flow depth measurement process. For higher discharges, higher flow thicknesses were obviously created, which in turn allowed to control better the depth of submersion of the flowmeter correspondent to a certain flow velocity. In addition, it is also associated with the inherent lack of accuracy of the measurement process due to the constraints presented before (presence of flow turbulence and variable velocities over the cross-section A).

4. SUMMARY AND CONCLUSIONS

This chapter presents a summary of the conclusions that have already been discussed in the report, as well general recommendations for further research.

First, brief preliminary conclusions are presented based on the conducted literature review. Most river flood protection dikes were not designed to withstand overtopping water volumes, and therefore, some type of protection/strengthening system must be provided in order to protect the underlying soil from erosion. During an overtopping event the landside slope of a dike is exposed to higher erosive forces than the waterside slope. The use of a surface protection/strengthening system is also expected to increase earthen dike resiliency (the capacity of the dike to fulfil its functions after design conditions have been exceeded), and hence, avoid reduction of dike crest elevation and catastrophic breaching when damage is inflicted on its structure beyond the levels it was designed for. However, still little design guidance is available for indicating appropriate overtopping protection measures to preclude erosion of dike crowns and landside slopes. A possible earthen dike slope protection consists of a flexible and light armouring system named turf reinforcement mat (TRM). These systems are suitable for earthen dikes with grass-covered slopes and crest in order to achieve their fullest performance potential. The present design guidance for onset of damage on grass-covered slopes is given by Hewlett *et al.* (1987) stability curves, which establishes a relation between limiting velocity and overflow duration. However, it is necessary to confirm through full-scale testing if these curves can predict reasonably the onset of damage for other grass species than the ones tested by Hewlett.

Design guidance for slope erosion protection/strengthening systems can be obtained for a series of commercial products by testing the products on steep channels subject to supercritical flows. Typically, design guidance includes the maximum allowable shear stress exerted by the flow on the slope protection system boundary and limiting (mean) flow velocity. These values are not only determined by the mechanical characteristics of the mat but also by the properties of the underlying soil. The mat's anchor type, length and arrangement over the slope is also a critical feature to assure that these performance thresholds are attained. Unfortunately, thresholds performance values are often available only for short-testing flow durations which may overestimate real world performance of a

RECP. Accordingly, a factor of safety should be applied to the manufacturer's published test data in order to adjust the expected mat performance to long-lasting flows.

Next a brief of the conclusions obtained from the experimental study realized with the aid of a hydraulic model are explained. As stated, the hydraulic model consists of steepen channel (1V:4H) wherein RECPs installed over erodible gravel beds were submitted to increasing overflow hydraulic forces in order to evaluate its erosion performance. It was found that bare gravel beds, $D_{50} \leq 25$ mm, are not suitable materials to be employed as a surface layer of a dike landside slope. Gravel layers with small grain sizes (s.B and s.C) were easier displaced than higher grain sizes layers (s.A) by the flowing water. The particle dimension had a clear influence on the performance of the open grids RECP M₁ and M₃ that were able to stabilize the gravel bed with higher grain size, s.A, but not the gravel beds of inferior grain sizes, s.B and s.C. As expected, RECP M₅ and M₆ showed the best performance in terms of erosion control since they are considered more technology advanced products than ordinary geogrids. The RECPs M₅ and M₆ were capable of providing effective erosion protection by locking in place the sediments s.C that had presented the most unstable behaviour when handling alone overflowing discharges. The RECPs M₁, M₃, M₅ and M₆ were able to withstand maximum overflowing discharges without erosion of the subgrade soil of 38.6, 45.4, 45.6 and 44.3 l/s/m, respectively. Due to constraints related to the test facility functionality it was not possible to attain a constant Q_{max} throughout the experimental study, as well as levels of discharge that would provoke pronounced erosion of underlying bed soil. Thus, permissible discharges of the flexible linings "M₁+s.A", "M₃+s.A", "M₅+s.C" and "M₆+s.C" obtained were probably conservative values that did not represent the full potential capabilities of the products in terms of erosion control (*i.e.*, RECPs could handle more discharge without underneath soil erosion). The erosion performance of RECPs such as TRMs (RECP M₅ and M₆) is not independent of underlying soil. Accordingly it would have been preferable to test a RECP over a compacted cohesive bed soil (with a % of clay and/or silt) with reduced permeability, typically found at earthen dike top soil layers.

The shear stress at one downward cross-section over the slope was also estimated using the formulation for steady uniform flow on a slope. This equation required the estimation of normal flow thicknesses. However, some concerns were raised about if the slope was long enough to allow the establishment of a uniform flow regime with a terminal flow velocity,

for discharges superior to $q \approx 16$ l/s/m. As this assumption was unlikely to be verified the shear stress estimation was probably an overestimated value. If two consecutive flow thickness measurement stations had been defined, it would have been possible to confirm if flow was still accelerating or not. Nevertheless, the maximum shear stress obtained over the reinforced lining “s.A+M₁” was a value ranging from 55.5 to 71.4 N/m² for a discharge value set in the flowmeter of $q=39$ l/s/m. The measured mean flow velocity associated with the shear stress exerted on the lining was about 1.54 m/s. According to the steady overflow limiting velocity curves of Hewlett *et al.* (1987) this magnitude of mean velocity can be withstand only with a grass-cover surface protection well established in a subgrade clayey soil of an earthen dike.

An estimation of the Manning’s roughness coefficient was calculated based on the mean flow velocity measurements parallel to the dike slope and unit discharge correspondent to the water column above the lining “s.A+M₁”. This discharge was expected to be smaller than the one measured in the flowmeter because it does not have into consideration the water that runs through the open spaces between the gravel particles. However, this was not verified probably due inaccurate flow thickness measurements that overestimated the real flow thickness. The reduced flow thicknesses over the slope were the main obstacle to the measurement of flow velocity with accuracy, at pre-defined depth throughout the water column. The estimated Manning’s n varied with the flow thickness measured for each level of discharge, as shown in Figure 80. It ranged between 0.027 and 0.031 for the highest flow discharge obtained in testing channel.

Both measurements of flow thickness and velocity had a considerable degree of uncertainty associated. The reader must be aware of this fact even though these values may seem between reasonable ranges of values.

Empirical correlations proposed by Hughes *et al.* (2011) were established for the steady overflow over the lining “s.A+M₁” that related the shear stress at a slope’s cross-section to a hydraulic parameter including steady unit discharge (calculated as the product as flow thickness and mean velocity) and specific weight of water (equations (52) and (53)). It were also proposed empirical correlations developed by Amini and Li (2012) that related a hydraulic parameter, including the flow thickness at a slope’s cross-section, to the unit discharge (calculated as the product as flow thickness and mean velocity) (equations (54) and (55)). The empirical linear correlations presented herein were strictly valid only for the

hydraulic model characteristics and the range of the tested hydraulic parameters (channel slope, surface roughness, etc.). Its predictive ability maybe strongly jeopardized by the error associated with data recording and also by the lack of extensive data log.

It was found that the flow velocities measured using the flowmeter for the three higher discharges attained in the hydraulic model could be well approximated to the mean flow velocity calculated according equation (10), considering that $U=u(z=0.37h_w)$. However, for lower discharges the velocimeter readings were not representative of mean velocity, due to the small flow thicknesses that did not submerge completely the propeller.

Future developments

This dissertation provides a basis for understanding the hydraulic processes involved in surge-overflow events responsible for causing surface erosion at earthen dikes and introduces measures to mitigate the problem consisting of lightweight surface protection covers with rolled erosion control products.

It would be interesting to perform advanced research on a real case study, wherein the hypothesis of reinforcing an earthen dike segment with a surface protection system to function like a bypass spillway, would be under appraisal. Note that this segment would allow that excessive flood water volumes of a main river course (due to heavy rainfalls) could be transferred into a flood detention area for temporary storage, and this way avoid that populated areas with economic value could be affected by the flood. The surface reinforcement solution under evaluation would consist of a high performance reinforcement mat (HPTRM) with proper anchor system. This real case study would be complemented with an experimental study to assess expected performance features attained by the interaction of the embankment surface soil with the HPTRM. The experimental study should be carried on a full-scale hydraulic model, in which a large surface layer of local soil reinforced with a strengthening solution could be installed and submitted to discharge levels representative of a local flood hydrograph for a considerable overflow duration (the spillway may carry a discharge flow for several hours). This slope surface layer would replicate an actual surface slope cover. Contrary to the conditions provided by the hydraulic model used in this dissertation, this test facility would ideally possess all the instrumentation and physical conditions to accurately calculate hydraulic parameters and simulate the erosion behaviour of the surface soil material under the mat, in order to evaluate the effectiveness of the solution before its implementation as a spillway.

REFERENCES

- Amini, F. and Li, L. (2012a). *Full-scale Overtopping Tests on Three Innovative Levee Strengthening Systems (SERRI Report 80009-01)*. Oak Ridge National Laboratory, Oak Ridge (Tennessee), USA.
- Amini, F. and Li, L. (2012b). *High Performance Turf Reinforcement Mat Strengthened Levee under Combined Wave and Storm Surge Turbulent Overtopping Conditions (SERRI Report 80009-02)*. Oak Ridge National Laboratory, Oak Ridge (Tennessee), USA.
- ASCE Hurricane Katrina External Review Panel (2007). *The New Orleans Hurricane Protection System: What Went Wrong and Why*. American Society of Civil Engineers (ASCE), Reston (Virginia), USA.
- ASTM D6460-1 (2012). *Standard Test Method for Determination of Rolled Erosion Control Product (RECP) Performance in Protecting Earthen Channels from Stormwater-Induced Erosion*. ASTM International, West Conshohocken, USA. (in Nelsen, 2005).
- ASTM D6460-99 (2000). *Standard Test Method for Determination of Erosion Control Blanket (ECB) Performance in Protecting Earthen Channels from Stormwater-Induced Erosion*, ASTM International. West Conshohocken, USA. (in Sprague 2011).
- Briaud, J. L.; Chen, H. C.; Govindasamy, A. V. and Storesund, R. (2008). Levee Erosion by Overtopping in New Orleans during the Katrina Hurricane. *Journal of Geotechnical and Geoenvironmental Engineering*, ASCE, 134(5), 618-632.
- Broere, D. (1999). *Breach erosion of earth dams*. MSc thesis, Delft University of Technology, Delft, The Netherlands.
- Chen, Y. H. and Cotton, G. K. (1988). *Design of Roadside Channels with Flexible Linings - Hydraulic Engineering Circular no. 15, 3rd Edition (report FHWA-IP-87-7)*. FHWA (US Department of Transportation), Virginia, USA. (in Nelsen, 2005).
- Chen, Z. Y. and Anderson, B. A. (1986). *Development of a methodology for estimating embankment damage due to flood overtopping (report FHWA/RD-86/126)*. Federal Highway Administration (FHWA) (US Department of Transportation), Virginia, USA.
- CIRIA; Ministry of Ecology and USACE (2013). *The International Levee Handbook (C731)*. Construction Industry Research and Information Association (CIRIA), London, United Kingdom.
- Dean, R. G.; Rosati, J. D.; Walton, T. L. and Edge, B. L. (2010). Erosional equivalences of levees: Steady and intermittent wave overtopping. *Ocean Engineering Journal*, Elsevier, 37(1), 104-113.
- Degoutte, G. (2012). *Les déversoirs sur les digues fluviales (Spillways on river flood protection levees)*. QUAE Editions, Versailles, France. (in CIRIA et al., 2013).
- FEMA, (2004). *Federal Guidelines for Dam Safety - Glossary of Terms*. Federal Emergency Management Agency (FEMA) - Interagency Committee on Dam Safety, Washington DC, USA.

- FEMA, (2008). *Geotextiles in Embankment Dams - Status Report on the Use of Geotextiles in Embankment Dam Construction and Rehabilitation*. FEMA's National Dam Safety Program, Colorado, USA.
- Flikweert, J.; Thornton, C.; Beasley, J.; Rowlette, R.; Kluskens, R. and Hughes, S. A. (2013). "Resiliency Against Overtopping - Determining the Need for Armouring on the Levees of New Orleans". Proceedings of the Coasts, Marine Structures and Breakwaters Conferences (Institution of Civil Engineers), Edinburgh (UK), 18-20 September.
- Gresser, C. S. (1996). *Soil Compaction and Stability (Informational sheet on compaction)*. Giles Engineering Associates, Waukesha, USA.
- Hanson, G. J. and Hunt, S.L. (2006). Lessons Learned using Laboratory JET Method to Measure Soil Erodibility of Compacted Soils. *Journal of Applied Engineering in Agriculture*, American Society of Agricultural and Biological Engineers (ASABE), 23(3), 305-312. (in CIRIA et al., 2013).
- Hanson, G. J. and Simon, A. (2001). Erodibility of cohesive streambeds in the loess of the Midwestern United States. *Hydrological Processes Journal*, Taylor & Francis, 15(1), 23-38.
- Hanson, G. J.; Tejral, R. D.; Hunt, S. L. and Temple, D. M. (2010). "Internal erosion and impact of erosion resistance". Proceedings of the 30th US Society on Dams Annual Meeting and Conference, Sacramento (USA), 12-16 April.
- Hanson, G. J.; Temple, D. M.; Morris, M. W. and Hassan, M. A. A. M. (2005). "Simplified breach analysis model for homogeneous embankments: Part II, Parameter inputs and variable scale model comparisons". Proceedings of the 2005 US Society on Dams Annual Meeting and Conference, Salt Lake City (USA), 6-10 June.
- Hanson, G.J. and Temple, D. M. (2002). Performance of bare-earth and vegetated steep channels under long-duration flows. *Transactions of the American Society of Agricultural Engineers Journal*, ASABE, 45(3), 695–701. (in Amini and Li, 2012b).
- Haselsteiner, R.; Strobl, T.; Heerten, G. and Werth, K. (2008). "Overflow Protection of Flood Embankments with Geosynthetics". Proceedings of the 4th European Geosynthetics Conference (EuroGeo 4), Edinburgh (Scotland), 7-10 September.
- Hassanzadeh, Y. (2012). *Hydraulics of Sediment Transport, Hydrodynamics - Theory and Model*. www.intechopen.com (accessed at 10/2/2014).
- Henderson, F. M. (1966). *Open channel flow*. MacMillian Publishing Co., New York, USA. (in Hughes et al., 2012).
- Hewlett, H. M.; Boorman, L. A. and Bramley, M. E. (1987). *Guide to the design of reinforced grass waterways (R116)*. CIRIA, London, United Kingdom. (in Hughes, 2011)
- Hughes, S. A. (2008). "Levee overtopping design guidance: what we know and what we need". Proceedings of the Solutions to Coastal Disasters Congress, Oahu (USA), 13-16 April.
- Hughes, S. A. (2008b). *Estimation of overtopping flow velocities on earthen levees due to irregular waves (CHETN Technical Notes Collection ERDC/CHL CHETN-III-77)*. US Army Engineer Research and Development Centre, Vicksburg (Mississippi), USA.

- Hughes, S. A. (2011). *Adaptation of the Levee Erosional Equivalence Method for the Hurricane Storm Damage Risk Reduction System (report ERDC/CHL TR-11-3)*. US Army Engineer Research and Development Centre (Coastal and Hydraulics Laboratory), Vicksburg (Mississippi), USA.
- Hughes, S. A. and Nadal, N. C. (2009). Laboratory study of combined wave overtopping and storm surge overflow of a levee. *Journal of Coastal Engineering*, Elsevier, 56(3), 244-259.
- Hughes, S. A. and Shaw, J. M. (2011). Continuity of Instantaneous Wave Overtopping Discharge with Application to Stream Power Concepts. *Journal of Waterway, Port, Coastal, and Ocean Engineering*, ASCE, 137(1), 12-25. (in Hughes et al, 2011).
- Hughes, S. A.; Sharp, J. A.; Shaw, J. M.; Howard, I. L. and McAnally, W. H. (2011). *Physical Testing and Hydraulic Simulation of Wave Overtopping of Earthen Levees (SERRI Report 70015-008)*. Oak Ridge National Laboratory, Oak Ridge (Tennessee), USA.
- Hughes, S. A.; Shaw J. M. and Howard, I. L. (2012). Earthen Levee Shear Stress Estimates for Combined Wave Overtopping and Surge Overflow. *Journal of Waterway, Port, Coastal, and Ocean Engineering*, ASCE, 138(3), 267-273.
- Hulitt, C. (2010). *Full-scale testing of three innovative levee strengthening systems under overtopping condition*. MSc thesis, Jackson State University, Jackson (Mississippi), USA.
- IPCC (2007). *Climate change 2007*. Intergovernmental Panel on Climate Change (IPCC), Geneva, Switzerland. (in Pickert et al., 2011).
- Kilgore, R. T. and Cotton, G. K. (2005). *Design of Roadside Channels with Flexible Linings - Hydraulic Engineering Circular no. 15, 3rd Edition (report FHWA-NHI-05-114)*. Federal Highway Administration (US Department of Transportation), Virginia, USA.
- Kortenhaus, A.; Doorn, N.; Hawkes, P.; Larson, M. and Sanchez-Arcilla, A. (2007). *Hydraulic loading of flood defence structures (FLOODsite report T02-07-04)*. www.floodsite.net (accessed at 21/10/2013).
- Lancaster, T. and Theisen, M. (2003). *Classifying rolled erosion-control products: a current perspective*. Erosion Control Technology Council (ECTC), St. Paul (Minnesota), USA.
- Landa, P. M. (2014). *Wave Overtopping Resilient 'Afsluitdijk', Design Procedures for Landward Slope Erosion Stability during Large Overtopping Volume Events*. MSc thesis, Delft University of Technology, Delft, the Netherlands.
- Miller, S. J.; Fischenich, J. C. and Thornton C. I. (2012). *Stability Thresholds and Performance Standards for Flexible Lining Materials in Channel and Slope Restoration Applications*. US Army Engineer Research and Development Centre (Environmental Laboratory), Vicksburg (Mississippi), USA.
- Morris, M.; Hassan, M.; Kortenhaus, A. and Visser, P. (2009). *Breaching Processes: A state of art review (FLOODsite report T06-06-03)*. www.floodsite.net (accessed at 21/10/2013).
- Nelsen, R. J. (2005). "Research Quantifies Performance of TRM Reinforced Vegetation". Proceedings of the Geo-Frontiers Congress 2005 - Erosion of Soils and Scour of Foundations, Austin (USA), 24-26 January.

- Oumeraci, H.; D'Eliso, C. and Kortenhaus, A. (2005). *Breaching of coastal dikes: State of the art (FLOODsite report T06-06-06)*. www.floodsite.net (accessed at 21/10/2013).
- Pan, Y.; Li, L.; Amini, F. and Kuang, C. (2012). Full-Scale HPTRM-Strengthened Levee Testing under Combined Wave and Surge Overtopping Conditions: Overtopping Hydraulics, Shear Stress, and Erosion Analysis. *Journal of Coastal Research*, CERF, 29(1), 182-200.
- Pickert, G.; Weitbrecht, V. and Bieberstein, A. (2011). Breaching of overtopped river embankments controlled by apparent cohesion. *Journal of Hydraulic Research*, Taylor & Francis, 49(2), 143-156.
- Powledge, G.R.; Ralston D. C.; Ralston, D.C. Miller, P.; Chen, Y. H.; Clopper, P. E. and Temple, D. M. (1989). Mechanics of overflow erosion on embankments. II: Hydraulic and Design Considerations. *Journal of Hydraulic Engineering*, ASCE, 115(8), 1056-1075.
- Pullen, T.; Allsop, N.W.H.; Bruce, T.; Kortenhaus, A.; Schüttrumpf, H. and van der Meer, J.W. (2007). *EurOtop: Wave overtopping of sea defences and related structures: Assessment Manual*. www.overtopping-manual.com (accessed at 2/2/2014).
- Quintela, A. C. (1981). *Hidráulica*. Fundação Calouste Gulbenkian, Lisbon, Portugal.
- Schmocker, L. (2011). *Hydraulics of dike breaching*. PhD thesis, Swiss Federal Institute of Technology, Zurich, Switzerland.
- Seed, R.B.; Bea, R.G.; Abdelmalak, R.I.; Athanasopoulos, A.G.; Boutwell, G.P.; Bray, J.D.; Briaud, J.L.; Cheung, C.; Cobos-Roa, D.; Cohen-Waeber, J.; Collins, B. D.; Ehrensing, L.; Farber, D.; Hanemann, M.; Harder, L. F.; Inkabi, K. S.; Kammerer, A.M.; Karadeniz, D.; Kayen, R.E.; Moss, R.E.S.; Nicks, J.; Nimmala, S.; Pestana, J.M.; Porter, J.; Rhee, K.; Riemer, M.F.; Roberts, K.; Rogers, J. D.; Storesund, R.; Govindasamy, A.V.; Vera-Grunauer, X.; Wartman, J.E.; Watkins, C.M.; Wenk, Jr. E. and Yim, S.C. (2006). *Investigation of the Performance of the New Orleans Flood Protection System in Hurricane Katrina on August 29, 2005*. University of California, Berkeley, USA.
- Sills, G. L.; Vroman, N. D.; Wahl, R. E. and Schwanz, N. T. (2008). Overview of New Orleans levee failures: Lessons learned and their impact on national levee design and assessment. *Journal of Geotechnical and Geoenvironmental Engineering*, ASCE, 134(5), 556-565. (in Amini and Li, 2012).
- Singh, V. P. (1996). *Dam breach modelling technology*. Kluwer, Doedrecht, The Netherlands.(in Schmocker, 2011).
- Sprague, C. J. (2011). *Large-scale Channel Erosion Testing (ASTM D6460) of Enviro scape ECM C4000 Double Net Coconut Blanket over Sandy Loam*. TRI/Environmental, Oakwood, USA.
- Sturm, T.W. (2001). *Open channel hydraulics*. McGraw-Hill Higher Education, New York, USA. (in Hughes et al., 2012).
- TAW (1996). *Clay for dikes (Technical report)*. Technical Advisory Committee on Water Retaining Structures, Delft, The Netherlands.(in Oumeraci et al., 2005).
- Temple, D. M. and Hanson, G. J. (1994). Headcut Development in Vegetated Earth Spillways, *Journal of Applied Engineering in Agriculture*, ASABE, 10(5), 677-682.

- Tensar® (2013). *RollMax® Instalation Guidelines*. www.tensarcorp.com (assessed at 2/3/2014).
- Thornton, C. I. and Beasley, J. (2013). “Overtopping Protection for Dams - Vegetative Cover and Turf Reinforcement Mats”. Proceedings of the 20th National Dam Safety Technical Seminar, Emmitsburg (USA), 20-21 February.
- van Gerven, K. A. J. and Akkerman, G. J. (2005). *State-of-the-art Inventory* (ComCoast report WP 3). Rijkswaterstaat, Delft, the Netherlands.
- Van Rijn, L. C. (1993). *Principles of sediment transport in rivers, estuaries, coastal seas*. Aqua Publications, Amsterdam, the Netherlands. (in Zhu, 2006).
- Van Rijn, L.C. (1984). Sediment pick-up functions. *Journal of Hydraulic Engineering*, ASCE, 110(10), 1494-1502. (in Zhu, 2006).
- Visser, P. J. (1998). *Breach growth in sand-dikes*. PhD thesis, Delft University of Technology, the Netherlands.
- Whitehead, E.; Schiele, M. and W. Bull, W. (1976). *A guide to the use of grass in hydraulic engineering practice (CIRIA Technical Note 71)*, CIRIA, London, UK.
- Young, K. C., and D. M. Stone (1967). *Resistance of low cost surfaces for farm dam spillways (Report 95)*. University of New South Wales (Water Research Laboratory). Sydney, Australia. (in Hughes, 2008b).
- Zhu, Y. (2006). *Breach growth in clay dikes*. PhD thesis, Delft University of Technology, Delft, the Netherlands.